

DEVELOPMENT OF MULTIANALYTE MICROPHYSIOMETRY FOR THE
STUDY OF ISLETS AND BIOLOGICAL TOXINS

By

Rachel M. Snider

Dissertation

Submitted to the Faculty of the
Graduate School of Vanderbilt University
in partial fulfillment of the requirements
for the degree of

Doctor of Philosophy

in

Chemistry

May, 2009

Nashville, Tennessee

Approved:

David E. Cliffel

Darryl J. Bornhop

Charles M. Lukehart

John P. Wikswo

David W. Wright

ACKNOWLEDGEMENTS

There are so many people I would like to thank and acknowledge for their support over the course of my life over the last 27 years and my education during the last 22 years. Growing up in Montgomery, Alabama, I was fortunate enough to be in the magnet programs from the year they opened. My love of science was sparked in the science lab of Forest Avenue Academic Magnet. Mrs. Bonnie Glaze continued to feed that interest at Baldwin Junior High. By the time I reached high school, I knew I wanted to study science. Mrs. Pam Moulton had a pivotal impact on me in her AP US History class. She challenged me intellectually to move beyond what I thought I could do to achieve what I was truly capable of.

Sweet Briar College was an ideal atmosphere for me to develop as a person and as a scholar. When I was in intro biology my freshman year, Dr. Robin Davies and her genetics class helped give me a dose of reality of how much college differed from high school. She was my advisor my first year and had an impact on me far greater than what classes I chose. Similarly, Dr. Rob Granger's general chemistry class my first year grabbed my attention and the instrumental analysis class later on solidified my future in analytical chemistry. It was Dr. Rob who led to my meeting Robert Hayes at SERMACS, starting my path to Vanderbilt University.

The chemistry department of SBC as a whole had a major impact on me. I am grateful to Dr. Jill Granger and her biochemistry class for giving me the foundation to be able to perform interdisciplinary research. On a side note, her choice of the Voet and Voet biochemistry textbook has been invaluable in writing this dissertation. Dr. Susan Piepho did everything in her power to make quantum and p-chem interesting. My senior

research project with her where I worked with LabVIEW shaped my future by feeding my interest in instrumental design and software development. Chapter III of this dissertation would not have been possible without her.

Here at Vanderbilt I am grateful to my entire committee for challenging me intellectually and for the growth that had come from that. Dr. David Cliffel has been the best advisor I think I could have asked for. I am still continually amazed by the depth of his knowledge on a huge array of topics. Dr. Cliffel has provided invaluable guidance as well as fostering my independence. I am also so grateful to the Cliffel lab as a whole. Sven Eklund and Madalina Ciobanu helped me get started on my research topics and inspired me to become the best scientist I could be. There have been so many lab members over the years from the early years of Dale, Rachel, and Aren to the group we are now. Also, Amy Rue, Chris Green, and Stanton Elseroad, Vanderbilt undergraduates I worked with, for their help on many different projects. The lab has been the place of a lot of great memories from lab lunches to Cliffel group parties with volleyball and Star Trek games to flood response drawers. Thank you all. I am grateful to every group member for their help over the years.

Beyond the help I have had within the lab, there have been many people and places outside of the lab that have helped me complete my dissertation. I would like to thank Claudia Schlee; if not for our fun evenings with Leon, Lola, and Polly I don't know how I would have gotten through the adjustment of my first year. My second year brought the arrival of three dear friends Ginny Grant, Craig Garmendia, and Sharon Hamilton. It was Ginny who introduced me to my love of hockey and the Nashville Predators. Also, I am extremely thankful to Ginny for my dissertation of a get-away in

September that helped me finish writing with a degree of sanity intact. Craig introduced me to the opera and symphony here and put up with my love of hockey. Sharon and I will always have the bonds forged by the phrases “War Eagle!” and “Ka-click!” Mekha George has been an invaluable support to me by believing in me even when I questioned. I can’t wait to walk across the stage with her in May. I will always be grateful that Jennifer Merritt decided to rotate through our lab and become one of my dearest friends. I also want to thank Alice van der Ende for Starbucks runs, Larissa Fenn for being my football buddy, the “girls” for lunches and fun nights at the Roof. The list goes on and on. I have made such amazing friendships and bonds over the last five and a half years, and I cannot thank you all enough.

The community I found at Good Shepherd has meant so much to me over the last year. Singing in the choir has given me a place to enjoy my more musical, less scientific side. The love and support of that community as a whole and the community of Cursillo have given me strength to keep going even when I didn’t want to type another word. To Father Randy, I can never thank you enough.

Last and very, very far from least I want to thank my family. I will never be able to express how much their love and support has meant to me. Mama and Daddy and my sisters, Josselyn, Elizabeth, and Judy, and the entire Snider/Johnson clan, knowing that I had your support behind me has enabled me to go forward and face any challenge. Especially to my precious niece Lainey, who has been a personal measuring stick of how long I’ve been in graduate school as she grew up, her sweet smile shining from my desktop background has brightened many days. I cannot find the words to adequately define how much you have done. I love you all so much.

To sum up, there have been innumerable people who have guided me, supported me, cracked me up when I needed a laugh, and given me a swift kick in the rear when I needed that. Thank you all. I am thankful for each one of you.

TABLE OF CONTENTS

	Page
ACKNOWLEDGEMENTS	ii
LIST OF TABLES	viii
LIST OF FIGURES	ix
LIST OF ABBREVIATIONS	xii
Chapter	
I. SYSTEMS BIOLOGY AND THE STUDY OF METABOLISM	1
II. DEVELOPMENT OF THE MULTIANALYTE MICROPHYSIOMETER	6
III. DEVELOPMENT FOR A MULTICHAMBER MULTIPOTENTIOSTAT FOR MULTIANALYTE MICROPHYSIOMETRY IN EIGHT ELECTROCHEMICAL CELLS SIMULTANEOUSLY	18
Introduction	18
Potentiostat Design	19
Experimental	23
Assembly	23
Computer control	26
Software	26
Calibration of multipotentiostat modules.....	30
Timing studies.....	31
Amperometric testing of the multipotentiostat with the MAMP	32
Results and discussion	33
Calibration.....	33
Timing studies.....	34
Testing of sensors in the MAMP	34
Conclusions	37
Acknowledgments.....	38
IV. STUDIES OF ISLET METABOLISM IN THE MAMP	39
Introduction.....	39
Experimental	48
Chemicals.....	48
Apparatus	49

Sensor head construction	50
Modified electrodes for the detection of insulin	51
Testing of films for insulin sensitivity	51
Testing of islets in the MAMP	52
Results and discussion	54
Conclusions	70
Acknowledgments.....	71
V. MAMP FOR THE STUDY OF THE METABOLIC EFFECTS OF CHOLERA TOXIN	72
Introduction.....	72
Experimental	75
Chemicals and instrumentation.....	75
MAMP experiments with pheochromacytoma cells.....	75
Results and discussion	76
Conclusions.....	93
Acknowledgments.....	94
Appendix	
A. DESIGN AND ASSEMBLY OF MULTIPOTENTIOSTAT MODULES FOR MULTIANALYTE MICROPHYSIOMETRY	95
B. MULTIPLE APPROACHES TO MODELING CURRENT RESPONSES IN THE MAMP TO DERIVE METABOLIC RATES	105
REFERENCES	107
CURRICULUM VITAE.....	116

LIST OF TABLES

Table	Page
1. Calibration values determined for a 4 chamber multipotentiostat	34
2. Insulin oxidation peak currents from cyclic voltammograms.....	56
3. Basal metabolic rates of PC-12 cells	77
4. Effect of 1000 nM CTx on glucose oxidase sensor in three chambers of cells	79

LIST OF FIGURES

Figure	Page
1. Hierarchical scales of biology	1
2. Titration of silanol and silamine insulating layer of LAPS at high and low pH	7
3. Formation of a junction between an n-type semiconductor and a solution containing a redox couple O/R	8
4. Schematic of the circuitry of the LAPS sensor of the Cytosensor	9
5. Photocurrent-voltage curves in LAPS and the effects of pH	9
6. Cytosensor data-analysis hierarchy	10
7. Cross sectional view of the sensor chamber of the Cytosensor	11
8. Illustration of glycolysis highlighting glucose, oxygen, lactate, carbon dioxide, and protons	12
9. Modified sensor head with four platinum electrodes	13
10. Enzyme films used in the MAMP	14
11. Current response at glucose oxidase electrode for a single stop flow with live and dead cells	16
12. Adder bipotentiostat with three working electrodes.....	25
13. Current follower with four switchable resistors	25
14. LabVIEW program written for calibration of multichannel multipotentiostats.....	27
15. Flow diagram of data collection software for multipotentiostat	28
16. User interface of LabVIEW program written for the multipotentiostat for use with the MAMP	29
17. Portion of the block diagram of multipotentiostat software for the MAMP dealing with data collection, graphing, and saving to file	30
18. “Dummy cell” used in calibration of multipotentiostats	35

19.	Current response of bare modified sensor head without cells present	35
20.	Current response at modified sensor head with glucose oxidase and lactate oxidase films without cells present	36
21.	Current response at modified sensor head with glucose oxidase and lactate oxidase films with 5×10^5 PC-12 pheochromacytoma cells.....	33
22.	Pancreatic islet.....	39
23.	Human insulin showing one intrastrand and two interstrand disulfide linkages.....	40
24.	Procedure used in allogenic islet transplantation	42
25.	Transmission electron micrograph of a single MWCNT	46
26.	Modified sensor head with a GCE and three platinum electrodes	50
27.	Cyclic voltammograms of MWCNT films in buffer and insulin	55
28.	Optical microscope images of MWCNT films on modified sensor head before and after testing in the MAMP	58
29.	Linear sweep voltammograms in MAMP of MWCNT/DHP composite film in buffer and $300 \mu\text{M}$ insulin	59
30.	Insulin calibration curves of MWCNT/DHP films on 3 mm GCE in bulk solution and 1 mM GCE in microfluidic chamber of MAMP	60
31.	Typical flow – stop flow amperometric current profile of a MWCNT/DHP sensor film in MAMP.....	62
32.	Amperometric current response MWCNT/DHP sensor film in MAMP with seventy five islets	63
33.	Insulin concentration (background subtracted) as measured with MWCNT/DHP composite film in the MAMP with islets upon stimulation with high glucose.....	64
34.	Insulin concentration (background subtracted) as measured with MWCNT/DHP composite film in another chamber of MAMP with islets upon stimulation with high glucose.....	65
35.	Normalized baseline current response at the lactate oxidase electrode in MAMP upon stimulation of seventy five islets with high glucose.....	66

36.	A-C) Insulin concentration (background subtracted) as measured with MWCNT/DHP composite film in the MAMP with 75 islets upon stimulation with high glucose and low glucose with 50 mM potassium.....	67-68
37.	Mechanism of action of cholera toxin	73
38.	Basal metabolic rates of three chambers of 5×10^5 PC-12 cells as measured in the MAMP	77
39.	MAMP signals for 5×10^5 PC-12 cells in response to 1000 nM CTx	79
40.	Metabolic rates of three chambers of PC-12 cells exposed to 1000 nM cholera toxin	80
41.	Metabolic response of PC-12 cells to 500 nM CTx	82
42.	Metabolic responses of three chamber of PC-12 cells to 3 exposures of 1000 nM CTx with each exposure 2 minutes long	83
43.	Metabolic responses of three chamber of PC-12 cells to 3 exposures of 100 nM CTx with each exposure 2 minutes long	84
44.	Metabolic responses of three chambers of PC-12 cells exposed to a single 2 minute dose of 100 nM CTx.....	86
45.	Effect of cholera toxin on adenylate cyclase and effect of cAMP on protein phosphorylation.....	87
46.	A-B) Metabolic responses of two different chambers of cells treated with $10 \mu\text{M}$ forskolin.....	88-89
47.	H-89, <i>N</i> -[2-(<i>p</i> -bromocinnamylamino)ethyl]-5-isoquinolinesulfonamide	90
48.	Metabolic responses of three chambers of PC-12 cells treated with $30 \mu\text{M}$ H-89 and a single two minute dose of 100 nM cholera toxin	91
49.	Role of glycogen breakdown in cellular metabolism	92
50.	Backplane of multipotentiostat.....	96
51.	Configuration card.....	98
52.	Multipotentiostat module	101
53.	Geometry of the 2D axi-symmetric problem. a) Enzyme sensor and b) Oxygen sensor	105

LIST OF ABBREVIATIONS

a :	microfluidic cell thickness
A :	area of the electrode
ADP:	adenosine diphosphate
ATCC:	American Type Culture Collection
BSA:	bovine serum albumin
C or C^0 :	concentration of the analyte
cAMP:	cyclic adenosine monophosphate
CAPK:	cAMP dependent protein kinase
CF1-3:	current followers 1-3
COSY:	correlation spectroscopy
CTx:	cholera toxin
CV:	cyclic voltammogram
D :	diffusion coefficient
DAQ:	data acquisition
DHP:	3,4-dihydro-2H-pyran
DMF:	<i>N,N</i> -dimethylformamide
E^0 :	standard potential of a redox couple
E_a :	potential of the anode
E_c :	potential of the cathode
ECAR:	extracellular acidification rate
E_{cell} :	potential of the electrochemical cell

EDTA:	ethylenediamine tetra-acetic acid
F:	Faraday's constant (96485 C/mol)
F1:	voltage follower
FVB:	Friend leukemia virus B strain of mice
G6P:	glucose-6-phosphate
GC:	gas chromatography
GCE:	glassy carbon electrode
GM1:	monosialotetrahexosylganglioside
GOx:	glucose oxidase
G α :	heterotrimeric G protein subunit which activates adenylate cyclase
GTP:	guanosine triphosphate
H-89:	<i>N</i> -[2-(<i>p</i> -bromocinnamylamino)ethyl]-5-isoquinolinesulfonamide
HBSS:	Hank's balance salt solution
I:	current
I2:	inverting amplifier
i_d :	diffusion limited current
i_l :	mass transport limited current
i_p :	stop flow peak current
k_{KIN} :	transport rate
LAPS:	light-addressable potentiometric sensor
LC:	liquid chromatography
LED:	light emitting diode
LOx:	lactate oxidase

LSV:	linear sweep voltammogram
m :	mass transfer coefficient
MAMP:	multianalyte microphysiometry
MAS:	magic angle spinning
MFA:	metabolic flux analysis
MS:	mass spectrometry
MWCNT:	multiwalled carbon nanotube
n :	number of moles of electrons in an electrochemical reaction
NADH/NAD ⁺ :	nicotinamide adenine dinucleotide
NMR:	nuclear magnetic resonance
ob/ob-:	obese mouse strain
PC:	potential control amplifier
PCB:	printed circuit board
PKA:	protein kinase A
PTFE:	polytetrafluoroethylene
R :	gas constant
R_f :	resistor of the current follower
R_i :	resistor of the dummy cell
T :	temperature in Kelvin
$t^{1/2}$:	inverse square root of time
T1DM:	type 1 diabetes mellitus
TDP:	time dependent potentiation
Tris:	tris(hydroxymethyl)aminomethane

UHPLC:	ultra high pressure liquid chromatography
V_i :	potential applied to the dummy cell
V_o :	potential read from the dummy cell
WE1:	working electrode 1
WE2:	working electrode 2
WE3:	working electrode 3
χ_{pip} :	applied potential at the inflection point of the photocurrent curve
Z2:	zero shift adder amplifier

CHAPTER I

SYSTEMS BIOLOGY AND THE STUDY OF METABOLISM

Systems biology is a field of science that is based on the exploration of the dynamics of complete biological entities by describing the interactions between all the components.^{1,2} Systems biology arose out of the realization that the vast amount of genomic and proteomic data being discovered needed to be examined in an integrated manner. The goal of systems biology is to define the properties, relationships and functions of a biological system. Figure 1 illustrates the hierarchy of scales involved in biology from molecules to whole animals.³

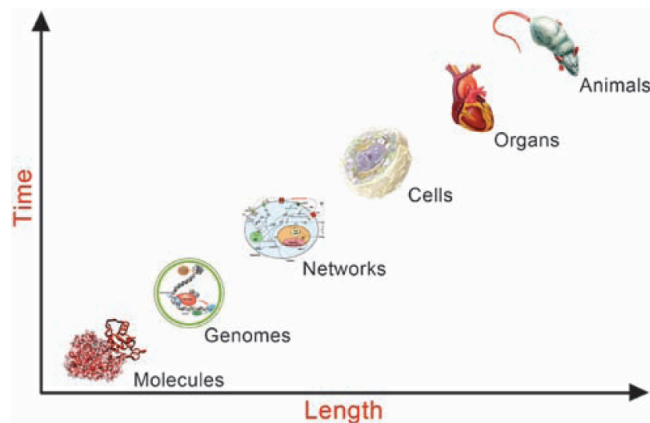


Figure 1. Hierarchical scales of biology³

The field of genomics began with the sequencing of entire genomes in the 1980s,² and proteomics is focused on the structure and function of proteins encoded in the DNA.³ Recent studies attempting to discover genes involved in disease have been almost too

sensitive, discovering that thousands of genes can change expression during the progression of cancer.^{4,5} In another study, 600 out of 9600 genes studied all showed correlation with the aggressiveness of lung cancer;⁶ however, it is not known which of these genes has a functional impact. As the rate that genes are being sequenced increases, the emphasis is being shifted to the function of genes. To some degree this can be studied with proteomics, as there is a clear link between gene sequence and protein structure. Yet, protein sequence alone cannot give a great deal of information about function. In most cases, the protein function can be derived from the phenotype⁷ and these studies examine proteins outside of their cellular context.³

In addition to genomics and proteomics, there is an ever-expanding taxonomy of additional “omics” fields, including the transcriptome, glycome, and metabolome.⁸ The term “metabolome” has been coined to describe the entire metabolic composition of an organism or cell.^{3,9,10} While some view metabolomics as a subset of metabonomics,¹⁰ others view the terms as interchangeable. According to Fiehn in his 2001 review, metabolomics is the “comprehensive and quantitative analysis of all metabolites.”¹¹ Metabonomics is very similar and is defined as “the quantitative measurement of the time-related multi-parametric metabolic response of living systems to pathophysiological stimuli or genetic modification.”¹² However, from a practical standpoint, metabolomics deals with metabolic regulation and fluxes of individual cells or cell types. Metabonomics is the study of biochemical profiles of whole organisms and is typically studied using biofluids, such as blood or urine, or cell or tissue extracts.^{3,10,13} The greatest impact of metabonomics has been in the area of toxicology, particularly preclinical toxicology, and the search for biomarkers.⁸

The main approaches currently in use for analysis of the metabolome are nuclear magnetic resonance (NMR) spectroscopy and mass spectrometry (MS) methods.^{7,8,10,13} Typically, MS methods are used in conjunction with a pre-separation of the metabolites using gas chromatography (GC), liquid chromatography (LC), high-pressure liquid chromatography (HPLC), or ultra-high-pressure liquid chromatography (UHPLC). MS has been widely used in metabolic fingerprinting and metabolite identification studies.¹³ As Robertson points out, “MS excels at selective identification of a molecular entity, while NMR excels at the identification of all proton containing species in a sample.” However, “specific platforms are not a prerequisite for metabolomic investigation.”⁸ Thus, the method best suited for a given study is dictated by the type of information desired.

Typically, ¹H spectra of biofluids contain thousands of signals that arise from the hundreds of molecules present that represent many biological pathways.¹⁰ This complex signal can be used to monitor increases or decreases in a particular signal as a result of a biological pathway as the signal intensity is dependent on the concentration in solution. More advanced two dimensional NMR methods, such as correlation spectroscopy (COSY), can be used to increase signal dispersion and elucidate the connectivity between signals.⁷ An additional advantage of NMR is that intact tissues can be studied without pretreatment using magic angle spinning (MAS). The term “magic angle” is derived from phenomenon that when a sample is spun rapidly (~4-6 kHz) at an angle of 54.7° relative to the applied magnetic field the line-broadening effects that would normally obscure the proton spectra of a solid sample are greatly reduced.^{8,10,13}

All metabolomic and metabonomic studies result in complex data sets that require “chemometric and biometric methods for interpretation and production of biochemical fingerprints that are of diagnostic or other classification value.”¹³ A number of approaches have been developed to model metabolism, such as structural, stoichiometric and carbon flux models, stationary and non-stationary mechanistic models, and models with gene regulation. The flux of carbon and electrons under varying conditions can be estimated by stoichiometric models of enzyme pathways and measurable quantities of metabolites.³ Metabolic flux analysis (MFA) determines the carbon fluxes in central carbon metabolism and related pathways based on measurement of extracellular rates, assuming pseudo steady state and a stoichiometric model of metabolism.^{14,15} MFA can provide insights into cellular metabolism under varied bioreactor conditions and rapidly clarify the cellular response to culture conditions. MFA experiments are limited to large numbers of cells in bioreactors or well-plates and are on a long term timescale but without continuous measurement.¹⁵ Most studies use either a stoichiometric approach or isotope tracer approach to estimate intracellular fluxes, and the metabolic fluxes are computed offline after analysis of nutrient and metabolite levels or isotopic tracer concentrations.¹⁵ Isotopically labeled metabolites in ¹³C tracer experiments can be analyzed *ex situ* using either NMR or mass spectrometry to determine the labeling pattern.^{14,15} The offline nature of MFA measurements cause no real-time information to be obtained about the pathways effected.¹⁵

A number of interesting physiological systems have extremely complex temporal behavior such as the cell cycle, circadian rhythm, and oscillations in glucose, insulin, and calcium by pancreatic islets.³ The development of other “omic” fields such as genomics

and proteomics were preceded by new instrumentation in electrophoresis and MS. In the same manner, new methodologies are necessary in the field of metabolomics to accurately model metabolism as a dynamic process. This dissertation centers on the development of an instrument that gathers dynamic real-time information on cellular metabolic processes, which we have named the multianalyte microphysiometer (MAMP).

CHAPTER II*

DEVELOPMENT OF THE MULTIANALYTE MICROPHYSIOMETER

The multianalyte microphysiometer (MAMP) has been used to measure the metabolic effects of fluoride, dinitrophenol, and antimycin A¹⁶ and applied to cancer studies of hypoxia and proliferation.¹⁷ Currently, the MAMP simultaneously measures the extracellular concentration of four analytes involved in cellular metabolism and was developed through modifications of an existing instrument, the Cytosensor[®] microphysiometer.¹⁶⁻²⁰

The Cytosensor[®] microphysiometer, released by Molecular Devices in 1990, uses a light addressable potentiometric sensor (LAPS) to study cellular metabolism by measuring changes in the extracellular acidification rate (ECAR).²¹ The Cytosensor[®] has been used to study many biological processes such as receptor pharmacology,^{22,23} enzyme modulators,²⁴ cytotoxins,²⁵ ionophores,²⁶ immune effectors,²⁷ and metabolic effectors.²⁸

The Cytosensor's LAPS forms the lower surface of the microfluidic chamber and is comprised of a silicon semiconductor chip coated with a thin insulating layer of silicon oxynitride. Chips are formed by first growing a 30 nm SiO₂ film followed by low pressure chemical vapor deposition of Si₃N₄.^{29,30} Hydration of the insulating surface creates silanol and silamine groups on the surface, as shown in Figure 2.³¹ These groups

*Eklund, S. E.; Snider, R. M.; Wikswo, J. P.; Baudenbacher, F.; Prokop, A.; Cliffel, D. E. *J. Electroanal. Chem.* **2006**, 587, 333-339.

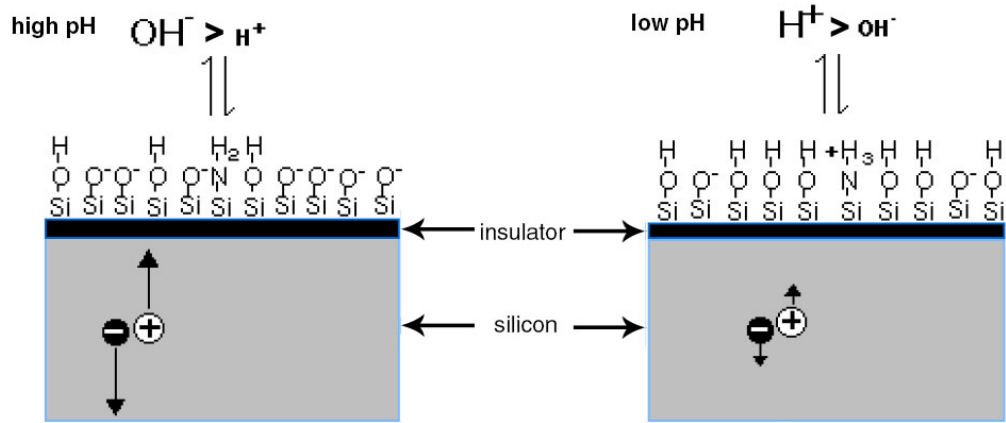


Figure 2. Titration of silanol and silamine insulating layer of LAPS at high and low pH. At high pH the surface potential of the insulating layer is increased causing electrons to migrate toward the bulk silicon and holes toward the surface.³¹

are titrated as the pH of the aqueous media changes, causing the surface potential of the insulating layer to shift by ~ 61 mV per pH unit at 37 °C.^{21,29,30,32} This change is in accordance with Nernst's Law, as shown by the calculation below where the only change in the system is an increase in the acidity of the solution from pH 7 to pH 6.³³

$$\begin{aligned}
 E_{\text{cell}} &= E_c - E_a \quad 2\text{H}^+ + 2\text{e}^- \longleftrightarrow \text{H}_2 \\
 E_a &= E_a^\circ + \frac{RT}{nF} \ln \frac{[\text{H}^+]^2}{p(\text{H}_2)} \\
 \Delta E_a &= E_{a(\text{pH}6)} - E_{a(\text{pH}7)} \\
 &= \frac{RT}{F} \ln \left(\frac{1 \times 10^{-6} \text{ M}}{1 \times 10^{-7} \text{ M}} \right) = \frac{8.314 \text{ J mol}^{-1} \text{ K}^{-1} \cdot 310 \text{ K}}{96485 \text{ C}} \ln 10 \\
 &= 61.5 \text{ mV}
 \end{aligned}$$

The LAPS is an n-type silicon semiconductor, which is formed when silicon is doped with an element whose valence electron energy closely matches the energy level of the conduction band, such as arsenic. In this case, at room temperature, the majority of donor atoms are ionized with each giving an electron in the conduction band and a corresponding positive site, or hole, in the donor atom. When an interface is formed between an n-type semiconductor and an electrolyte, a space charge region forms in the

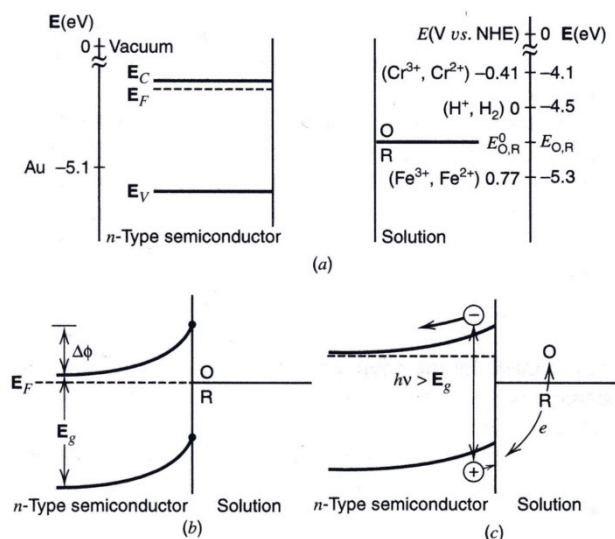


Figure 3. The formation of a junction between an n-type semiconductor and a solution containing a redox couple O/R. (a) Before contact in the dark. Typical values for energy levels shown referenced to NHE (E^0) and to vacuum (E). (b) After contact in the dark and electrostatic equilibration, (c) Junction under irradiation. [Adapted from Bard]³³

semiconductor at the interface causing the band energies of the semiconductor to become more negative with increasing distance into the semiconductor, an effect known as “band bending.” When this is illuminated by light with energy higher than the band gap of the semiconductor, photons are absorbed and electron-hole pairs are formed. The space charge region promotes the separation of these pairs, with electrons moving into the bulk material and holes toward the surface, where they promote photo-oxidation and a photoanodic current. Figure 3 illustrates the energy levels of an n-type semiconductor alone, in contact with an electrolyte solution in the dark, and in contact with an electrolyte solution when illuminated.³³

In the LAPS, a voltage is applied to the insulating layer by placing an electrode in the aqueous solution and attaching another electrode to the bare silicon surface, producing an electric field within the insulating layer and at the silicon-insulator

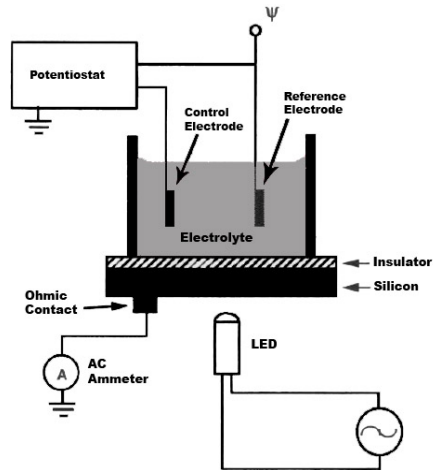


Figure 4. Schematic of the circuitry of the LAPS sensor of the Cytosensor. The LED is infrared and modulated at 10 kHz.^{31,32}

interface.^{21,31} A schematic of the LAPS and its corresponding circuitry is given in Figure 4.^{31,32} In this case, a 10 kHz modulated infrared LED is pulsed on the back of the silicon sensor, and the magnitude of the photocurrent depends on the magnitude of the electric field, which in turn is the sum of both the applied potential and the surface potential of the insulating layer.^{30,31,34,35} As shown in Figure 5, the photocurrent-applied

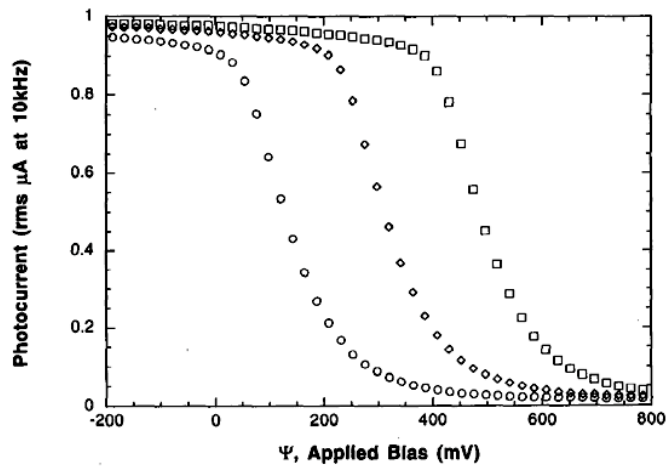


Figure 5. Photocurrent-voltage curves in LAPS and the effects of pH. The potential from solution to the silicon bulk was swept from -200 to + 800 mV while the light intensity was modulated at 10 kHz and the photocurrent was recorded. The curves represent pH 4.0 (circles), pH 7.0 (diamonds), and pH 10.0 (squares). [Adapted from Owicki]³⁰

potential curves generated at the LAPS change as the pH of the solution on the top of the LAPS changes.³⁰ Thus to obtain a constant photocurrent with changing pH and changing surface potential, the applied potential must be adjusted.^{21,29-32,34}

There are multiple layers to the LAPS data in the Cytosensor; Figure 6 shows the hierarchy of this data.³⁰ The potential applied across the silicon chip is scanned, and the photocurrent measured to obtain the initial level of data. The applied potential at the inflection point of the photocurrent curve, Ψ_{pip} , is reported to the user as the raw data in the Cytosensor software at 1 Hz. The rate of change in Ψ_{pip} is reported in $-\mu\text{V/s}$ and is referred to as the ECAR.^{30,31}

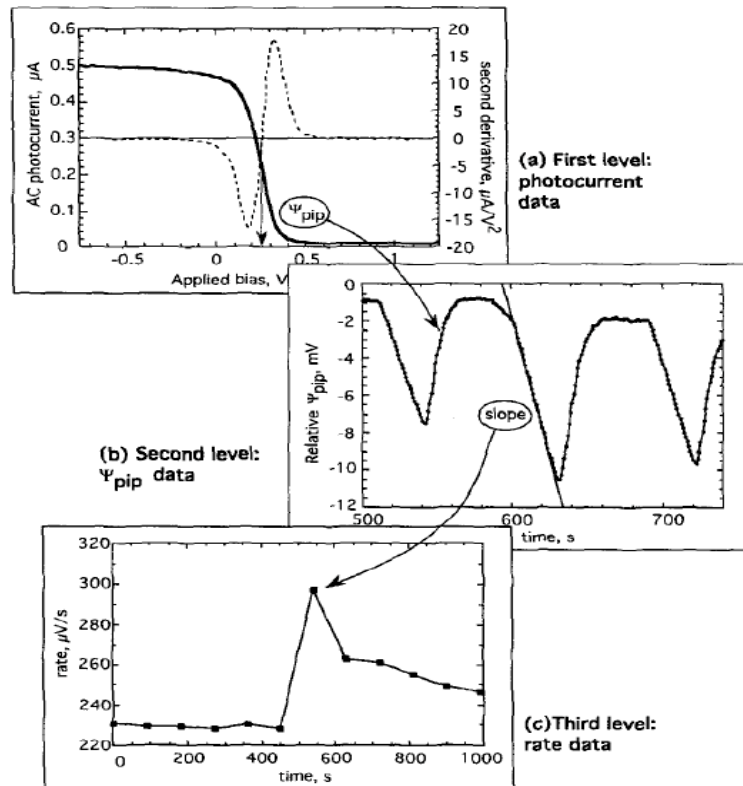


Figure 6. Cytosensor data-analysis hierarchy. (a) The photoresponse curve (solid line). The inflection point of the photoresponse curve (Ψ_{pip}) is determined by finding the zero crossing of the second derivative (dashed line). (b) Ψ_{pip} is plotted versus time as the surface potential shifts its value. (c) The rate of change in the surface potential is determined by a least-squares fit.³⁰

A cross-sectional view of the Cytosensor sensor chamber is depicted in Figure 7.¹⁷ The cells used in Cytosensor experiments typically are seeded the night prior the experiment into Corning Costar® Transwell® tissue culture treated 3 μm pore polycarbonate membrane capsule cups with total area of 1.12 cm^2 . Cells are seeded at a density $3\text{-}5 \times 10^5$ cells/capsule cup, such that the cells will be 75-80% confluent. A spacer is placed atop the cells to help define the chamber volume and limit the area of cells exposed to 25% of the total area. An additional 3 μm pore polycarbonate membrane insert is placed on top of the spacer. The cells are placed atop the LAPS, which forms the lower surface of the sensor chamber. The sensor head, which contains fluid tubes and the counter electrode of the LAPS, is clamped down on top by a gantry with the o-ring defining the chamber height of $\sim 100 \mu\text{m}$ and $\sim 3 \mu\text{L}$ volume as well as creating electrical contact between the sensor head and the LAPS.

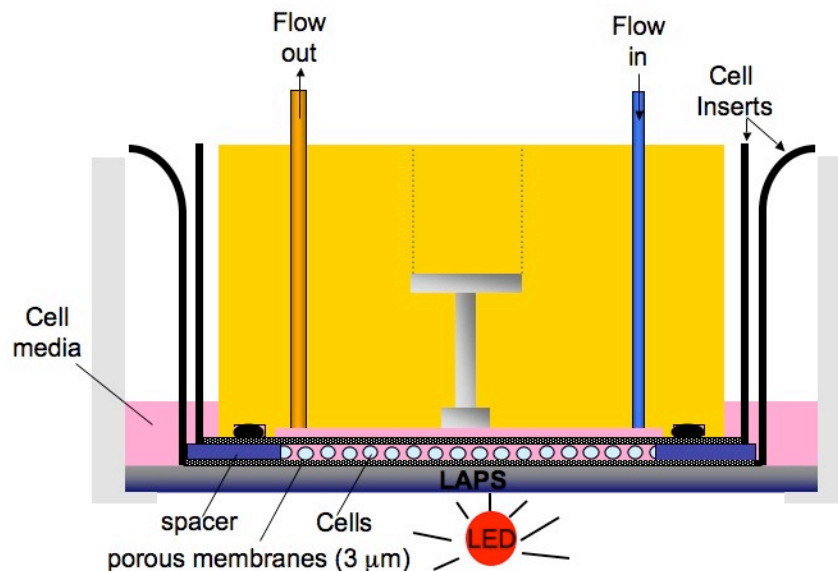


Figure 7. Cross sectional view of the sensor chamber of the Cytosensor showing the LAPS, LED, cells (trapped between two 3 μm pore membranes), spacer, and sensor head.¹⁷

In order to allow acidic byproducts of cellular metabolism such as lactic acid and carbonic acid to accumulate, lowering of the pH of the media, the Cytosensor is designed around a stop flow cycle of 120 s with 80 s of flow at 100 $\mu\text{L}/\text{min}$ and 40 s of stop flow. The media used in the Cytosensor is weakly buffered (1 mM phosphate) in order to allow greater sensitivity. As designed, changes measured in ECAR are correlated to changes in the metabolic activity of the cells.³¹ However, protons are only one of many chemical species involved in cellular metabolism, as seen in Figure 8. Also, the proton concentration is affected by changes in both anaerobic metabolism, through lactic acid, and aerobic metabolism through the production of carbon dioxide.¹⁷ In order to draw conclusions about the effect of a molecule of interest on cellular activity, information on more metabolic parameters is needed. The MAMP was developed from the Cytosensor by the inclusion of electrochemical sensors for extracellular glucose, lactate, and oxygen.¹⁶⁻¹⁹ A more complete picture of cellular metabolism can be obtained with glucose and oxygen as input parameters and lactate and acidification as output parameters.

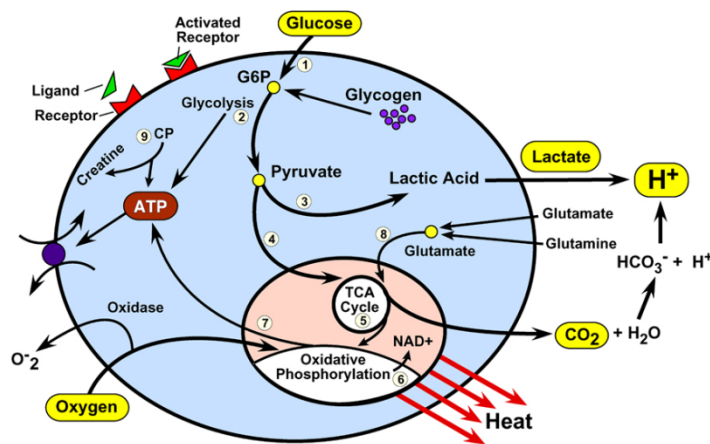


Figure 8. Illustration of glycolysis highlighting glucose, oxygen, lactate, carbon dioxide, and protons.¹⁷

To measure these three new analytes, the sensor head was modified by adding four platinum electrodes, one of which acts as the secondary counter electrode. Four 0.6 mm paths are drilled through the sensor head with the hole for the counter electrode widened on the surface to ~2 mm. The counter electrode is made by melting a 0.5 mm platinum electrode to form a 1.5 mm ball at the end. Two of the working electrodes are 0.5 mm platinum wires used for glucose and lactate measurements. The third working electrode, used to measure oxygen, is a 127 μm platinum wire, which is wrapped multiple times around a 0.5 mm platinum wire for added mechanical stability, with silver epoxy used to aid the electrical contact between the two. Each wire is embedded in the sensor head with white epoxy, ground down flush to the face of the sensor head using silicon carbide grinding paper, and polished with 1 μm diamond paste. The wires extending from the sensor head are reinforced with copper socket pins to add mechanical strength. Additional electrodes of different size or made of another material can be added. The surface of a modified sensor head, shown in Figure 9, is cleaned with water and ethanol, and the electrodes cleaned electrochemically by cycling in 0.5 M sulfuric acid.

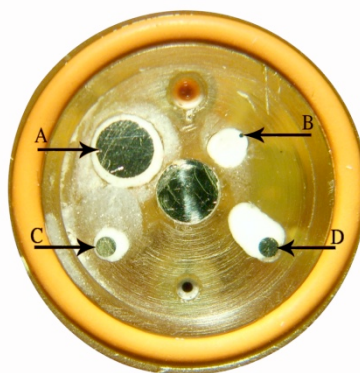


Figure 9. Modified sensor head with one 1.5 mm (A), one 127 μm (B), and two 0.5 mm platinum electrodes (C and D).

Glucose, lactate, and oxygen are all measured amperometrically using the counter electrode on the modified sensor head and the reference electrode of the Cytosensor at a low frequency, to help prevent cross-talk with the high frequency measurement of the LAPS. Oxygen is detected through direct reduction at the 127 μm electrode at -0.45 V vs. Ag/AgCl (2 M KCl). Glucose and lactate are measured indirectly through oxidation of hydrogen peroxide produced through the reaction of glucose oxidase (GOx) and lactate oxidase (LOx) enzymes at $+0.6\text{ V}$ vs. Ag/AgCl (2 M KCl), as shown in Figure 10. GOx and LOx films are formed by hand casting onto the electrode surface a solution of the enzyme, bovine serum albumin (BSA), and glutaraldehyde. A thin layer of Nafion (perfluorosulfonic acid-PTFE copolymer, 5% w/w solution in ethanol) can be added to either the glucose or oxygen sensor to act as a diffusion barrier and help to prevent biofouling.

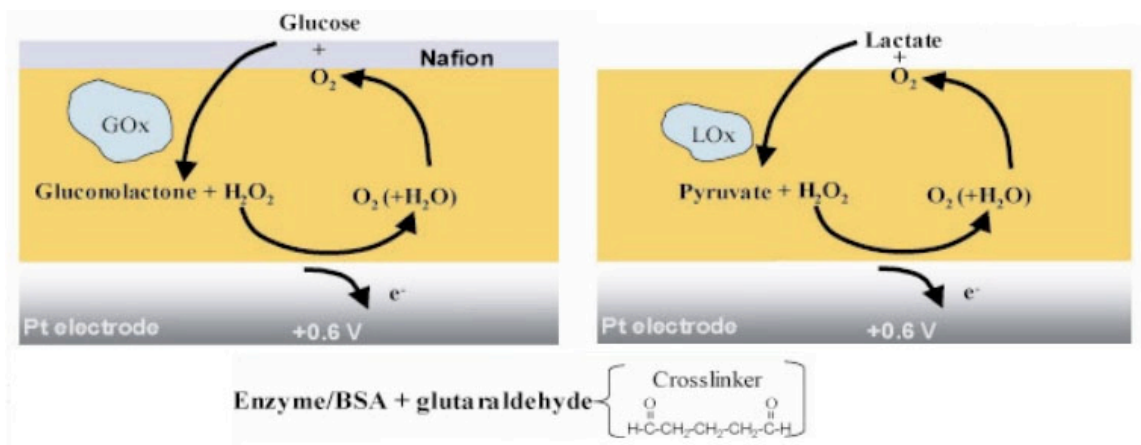


Figure 10. Enzyme films used in the MAMP. Glucose and lactate are measured indirectly through the reduction at $+0.6\text{ V}$ of hydrogen peroxide created by reaction with their respective oxidase enzymes, GOx and LOx. Enzyme films are formed by hand casting a solution of the enzyme, bovine serum albumin, and glutaraldehyde onto the electrode surface. A layer of Nafion can be added to the GOx film to act as a diffusion barrier and help prevent biofouling.

In an MAMP experiment to measure basal metabolic rates, cells are introduced into the MAMP, and data collection is begun. Once the cells equilibrate for at least one hour, they are killed using alamethicin, a cell permeabilizing agent,³⁶ to collect the sensor responses in the absence of cellular activity and calibrate the enzyme films with solutions of known glucose and lactate concentration. Sodium fluoride was used in initial experiments as a means of metabolic inactivation.¹⁶ The production of lactate is prevented in the presence of sodium fluoride, an inhibitor of enolase, which converts 2-phosphoglycerate to phosphoenolpyruvate.³⁷ However, sodium fluoride does not completely inhibit glycolysis³⁸ and has been shown to be an interferent in tests utilizing glucose oxidase.³⁹ The media sold by Molecular Devices for use in the Cytosensor is low buffered (1 mM phosphate) and contains 11 mM glucose.³¹ In order to use a more physiologically relevant glucose concentration (5 mM)⁴⁰ and calibrate the glucose sensor, a custom media was developed in conjunction with Mediatech, which is identical to the media sold by Molecular Devices but without glucose.

MAMP data is reported as current (nA) with time; Figure 11 shows the response of a glucose oxidase sensor for a single stop-flow cycle with live and dead cells. With the pump on, the media flows at a rate of 100 $\mu\text{L}/\text{min}$, and the current response is steady state. When the pumps stop, the current decays as glucose is depleted from the media by the cells and also at the sensor. When the pump restarts, the media is refreshed, and the current returns to its steady state value. The current response of a given stop flow period, i_p , is defined as the difference between the steady state current and the current at the end of the stop flow. Data is then analyzed by subtracting the response with dead cells from

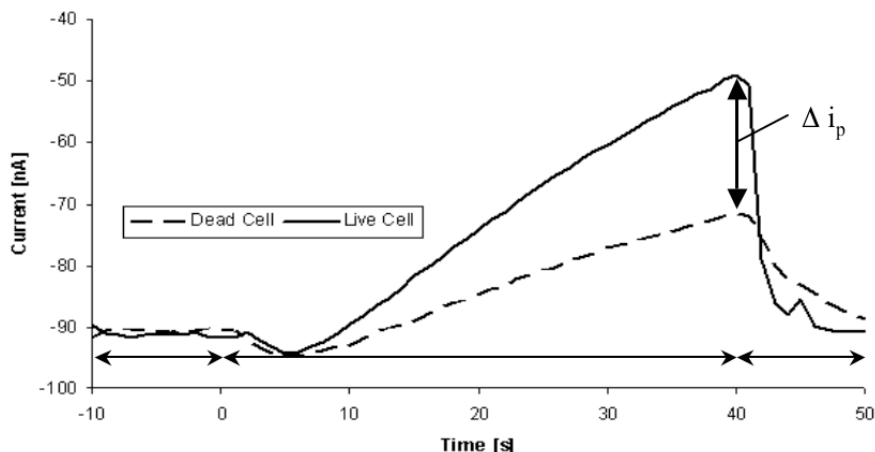


Figure 11. Current response at glucose oxidase electrode for a single stop flow with live and dead cells. The current is at a steady state with the pumps on (-10 to 0 s) and then decays when the pump is off (0 to 40 s). Upon resumption of flow, the current returns to its steady state level.

the response with live cells to obtain the current response due to cellular activity, Δi_p in Figure 11.

The concentration in the chamber at the end of the stop flow is calculated from Δi_p using the calibration at the end of the experiment. By accounting for the microfluidic volume, the number of cells present, and the length of the stop flow period, metabolic rates can be calculated in terms of $\text{mol cell}^{-1} \text{s}^{-1}$. Modeling efforts are underway to develop methods of analyzing the data over the entire stop flow period by modeling the stop flow period as a Cottrell step and through a mathematical model.

The research presented in this dissertation is focused on improving the robustness of multianalyte microphysiometry as a tool in metabonomics. A new multipotentiostat has been developed, with each chamber having three working electrodes and an individual reference and counter electrode. This allows for the simultaneous collection of data from up to eight channels of the MAMP. Through the development of an insulin sensitive electrode and study of the metabolic responses of isolated murine islets, the

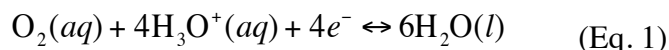
MAMP has been applied to new areas of research. The MAMP has been utilized as a tool for investigating the signaling pathways that lead to the metabolic response measured when cells are exposed to a toxin.

CHAPTER III*

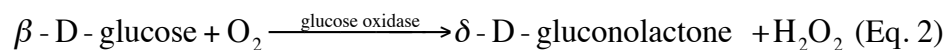
DEVELOPMENT FOR A MULTICHAMBER MULTIPOTENTIOSTAT FOR MULTIANALYTE MICROPHYSIOMETRY IN EIGHT ELECTROCHEMICAL CELLS SIMULTANEOUSLY

Introduction

One of the first electrochemical biosensors was the Clark electrode developed in 1953 by Lealand C. Clark, to measure the level of dissolved oxygen in blood.⁴¹ In a Clark electrode, the sensor contains a gas permeable membrane through which oxygen, nitrogen, and carbon dioxide all diffuse. However, only oxygen is reduced at the cathode through the following reaction (Eq. 1).⁴²



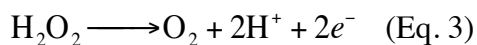
The development of amperometric sensors has been linked to the need for blood glucose monitoring, which is employed by diabetics who comprise 5% of the world population. No other bioassay is performed as frequently.⁴³ Blood glucose monitoring accounts for approximately 85% of the biosensor market.⁴⁴ The idea of a glucose enzyme electrode was first proposed by Clark and Lyons in 1962.⁴⁵ This first sensor was a thin layer of glucose oxidase trapped over a Clark oxygen electrode. Glucose oxidase reacts oxygen in the enzyme-catalyzed reaction shown in Equation 2.



The amount of oxygen consumed at the electrode could thus be linked to the concentration of glucose present.

* Lima, E.A.; **Snider, R.M.**; Reiserer, R.S.; Wikswo, J.P.; Cliffl, D.E. (to be submitted to *Sensors and Actuators B*)

In 1973, an amperometric sensor for direct oxidation of the hydrogen peroxide, Equation. 3,⁴⁴ produced by the enzymatic reaction of glucose oxidase was developed by Guilbault and Lubrano.⁴⁶



Today amperometric electrodes have been developed for a great number of biological molecules. Electrochemical sensors have been widely used in the field of neuroscience due to the large number of electrochemically active neurotransmitters including catecholamine, indolamine, glutamate, lactate, ascorbate, nitric oxide, dopamine, acetylcholine, and choline.^{47,48} Electrodes have been able to be implanted into the brains of mice, allowing real time measurements of neurotransmitter release.⁴⁹ Today electrochemical biosensors are being utilized in a number of fields including toxicology to provide high throughput electrochemistry through the use of interdigitated electrode arrays,⁵⁰ instrumented well plates,^{51,52} and addressable electrode arrays.⁵³

Potentiostat Design

All amperometric sensors are based upon the oxidation or reduction of an analyte and require a three-electrode potentiostat instrument that controls the working electrode, counter electrode and reference electrode.^{33,54} A potentiostat is used to measure the current that passes between the working electrode and counter electrode, while holding the potential of the working electrode constant in relation to the reference electrode.^{33,42} The term “potentiostat” was coined by A. Hickling, who developed the first instrument capable of automatic potential control.⁵⁴⁻⁵⁶ Hickling’s potentiostat spurred research into

controlled potential methods, as it did not require continuous operator control of the applied potential.^{54,56}

A simple potentiostat based on a single operational amplifier serves as the basis for a Wenking potentiostat. In the Wenking design, the working electrode is held at absolute ground, the desired applied potential is inverted into the input of the op-amp, and the counter connected to the output of the op-amp. The current is measured in a series resistor coming out of the op-amp. A key feature of this design is that there is no direct electronic feedback from the output of the op-amp to the inputs, making the amplifier an open-loop configuration, which is inherently prone to high frequency oscillations.

Improvements on this most basic design include the use of an electrometer circuit to measure the current between the counter and the working electrodes. This electrometer circuit holds the working electrode at virtual ground and replaces the series resistors of the Wenking potentiostats for current measurements. Other typical improvements include a voltage follower circuit to invert the desired potential at the reference electrode, and a current buffer to allow the counter electrode to draw larger currents.^{33,54,56}

Development of more advanced potentiostat designs for a wide range of specific instrumental needs has flourished in both academic and commercial fields. The design of advanced potentiostat instrumentation is based on the simple potentiostat circuit described above, but focuses on the specific improvements necessary for desired applications. These specific improvements include faster time responses leading to faster scan rates, lower power consumption, field portability, bi- and multi-potentiostats,

and electrically isolated circuitry. Faster time responses involving positive feedback compensation have enabled the development of fast-scan cyclic voltammetry measurements with scan rates over a megavolt per second.⁵⁷ Lower power consumption enables the development of long-lived battery powered potentiostats at low-cost for miniaturization.⁵⁸ Combination of low power, miniaturization, and integrated electronics enabled field portable designs for numerous hand-held biosensor applications.⁵⁹⁻⁶⁴ Electrically isolated circuitry enables potentiostats to be combined with other electronic instrumentation such as on-chip capillary electrophoresis,⁶⁵ and can be accomplished using opto-couplers.⁶⁶ Simultaneous measurements can be performed in multiple electrochemical cells, each comprised of an individual set of working, counter, and reference electrodes, forming an array of single analyte potentiostats.⁶⁷ Scribner and Associates have developed a commercial multichannel potentiostat that has 100 working electrodes all at the same potential, each with its own electrometer circuitry, and a single counter and reference electrode, and a 64 working electrode system was described in the literature.⁶⁸

In contrast, the design of two working electrodes with independent potential control in a single electrochemical cell leads to conventional bipotentiostats.³³ Expanding the number of working electrodes per electrochemical cell has led to multipotentiostats like a quadpotentiostat⁶⁹ and the commercial CH Instruments 1030 which controls eight separate working electrode potentials with a single counter and reference.

In order to measure multiple analytes in multiple electrochemical cells simultaneously, we have created a multichamber multipotentiostat. This multichamber multipotentiostat consists of an array of 4 or 8 multipotentiostats operating

simultaneously, similar to the array of single potentiostats by Popovtzer.⁶⁷ Each of these multipotentiostats has three working electrodes, two of which shared the same applied potential, as in the Scribner potentiostat design,⁶⁸ and one of which has a separate working electrode potential as in a conventional adder multipotentiostat like the CHI 1030. This multichamber multipotentiostat enables us to monitor multiple analytes in different fluidic chambers simultaneously. This instrument could be used for instrumenting conventional well-plates with multiple electrochemical sensors, but our specific application has been to develop multianalyte microphysiometry in microfluidic chambers.

Conventional 4 or 8 chamber microphysiometry was commercialized as the Cytosensor by Molecular Devices and measured pH to obtain the extracellular acidification rates (ECAR) using a light addressable potentiometric sensor (LAPS), where the ECAR are correlated to changes in cellular metabolism. Multianalyte microphysiometer (MAMP) expanded upon the Cytosensor[®] microphysiometer with the addition of amperometric electrodes for monitoring glucose, lactate and oxygen. Using our multichamber multipotentiostats, the MAMP can be used to measure the four-analyte metabolic response of cells in either four or eight microfluidic chambers simultaneously. The reference electrode is downstream from the microfluidic chamber and is shared with the potentiometric measurement of the LAPS. The amperometric measurements utilize a modified sensor head with three working electrodes and a counter electrode in each chamber. Thus each microfluidic chamber is a discrete electrochemical cell with its own reference and counter electrodes and three working electrodes.^{16,18,19}

Initial MAMP experiments were developed utilizing a CH Instruments 1030 multipotentiostat.^{16,18,19} This instrument is capable of measuring up to eight working electrodes simultaneously; however, it is designed for all eight working electrodes to be used in a single electrochemical cell. For this reason, only a single chamber of the MAMP could be utilized at any given time. Also, it is not feasible to run multiple 1030 multipotentiostats off of a single computer. Thus, there was a need to develop a multichamber multipotentiostat capable of recording the amperometric response in eight electrochemical cells of three working electrodes each simultaneously. To be best suited for the MAMP, the multipotentiostat must be capable of reliable measurement at a low frequency to help prevent cross talk with the high frequency LAPS sensor (10 kHz).³⁰

Experimental

Assembly

The multichamber multipotentiostat designed for use with the MAMP is a combination of features of previous multipotentiostat designs with two working electrodes being held at the same potential (CF1 and CF2), and a third at a separate potential (CF3). A schematic of this design type is shown in Figure 12.³³ In this potentiostat, the current outputs for each working electrode are read using an electrometer circuit (current followers: CF1, CF2, and CF3). In the design for our multipotentiostat, the feedback resistance for each electrometer is digitally selected with a multiplexer based on the sensitivity setting in the LabVIEW software from a set of four resistors as shown in Figure 13. The reference electrode is directly connected to F1, a voltage follower that fixes the reference potential at the negative of the input working electrode

potential while providing a high impedance at the reference electrode. The potential control amplifier, PC, is the heart of the potentiostat (the Wenking single op-amp equivalent) and does not have a feedback loop except for some small capacitors that are used to reduce the problems with tripping into oscillations. The second potential control circuitry is shown in the top right of Figure 12, where the first inverting amplifier, I2, provides the inverted second potential to a zero shift adder amplifier, Z2, that results in an output potential that is the difference between the second applied potential and the first applied potential. This potential difference, Δe , is then used as the positive input potential for the electrometer for the separate potential working electrode, CF3. The potential output of CF3 would normally need to be measured differentially; however, we use an instrumentational amplifier to subtract Δe after CF3 and are able to measure the differential output voltage generated as a non-referenced single ended input to the DAQ card.

Multipotentiostat modules were designed and built by Ron Reiserer and Eduardo Lima. Each multipotentiostat module performs the functions shown in Figure 12 and is used to measure one electrochemical cell chamber. The multipotentiostat modules are stacked into an array of 4 or 8 modules that are each connected in a backplane and comprise the multichamber multipotentiostat. A detailed description of the schematics and assembly of the multipotentiostat modules, written by Eduardo Lima, who built the potentiostat modules and wrote software for their calibration, is given in Appendix A.

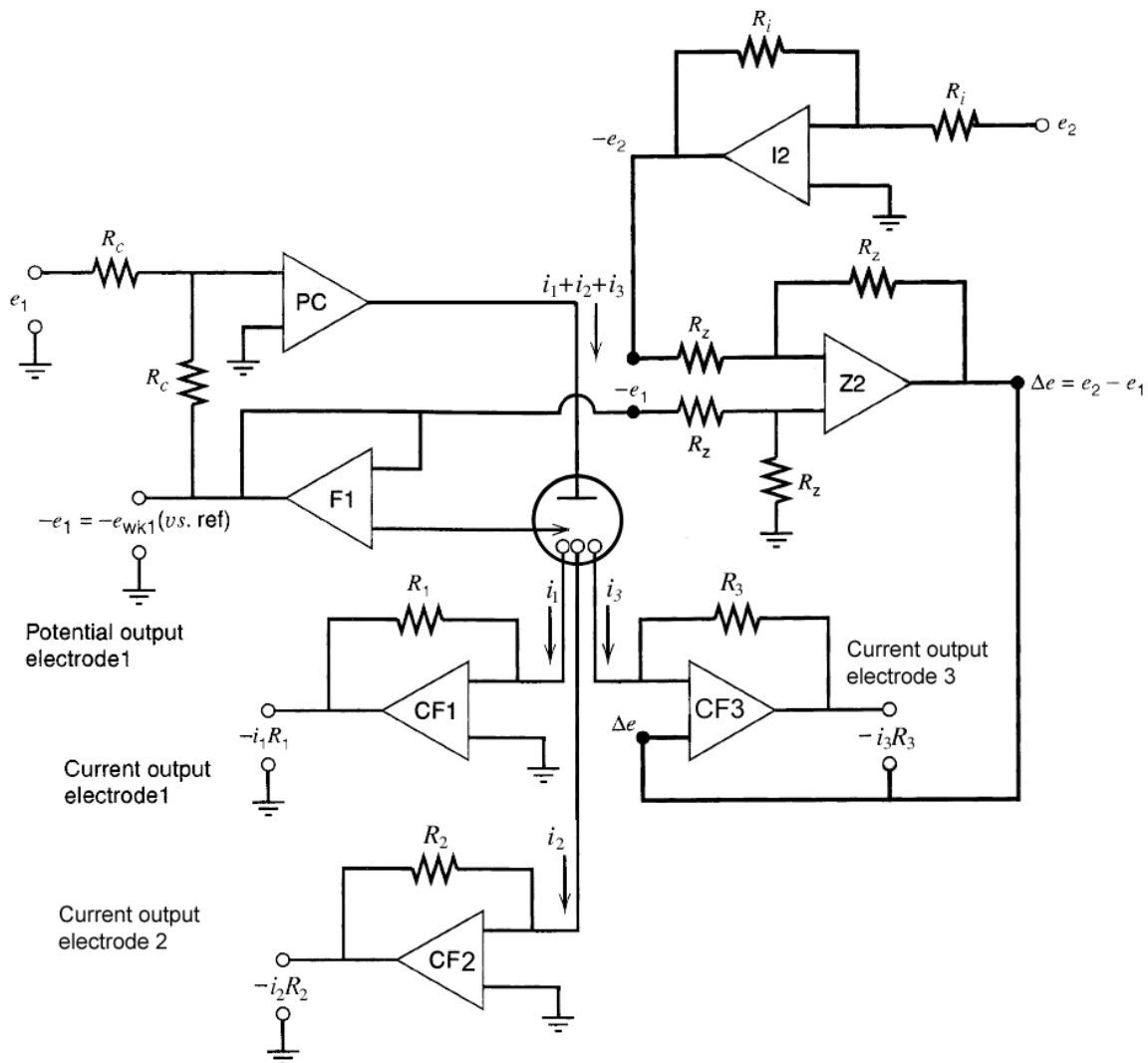


Figure 12. Adder bipotentiostat with three working electrodes [Adapted from Bard]³³

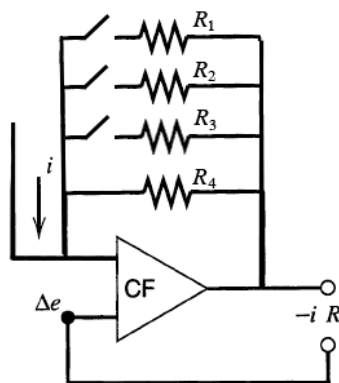


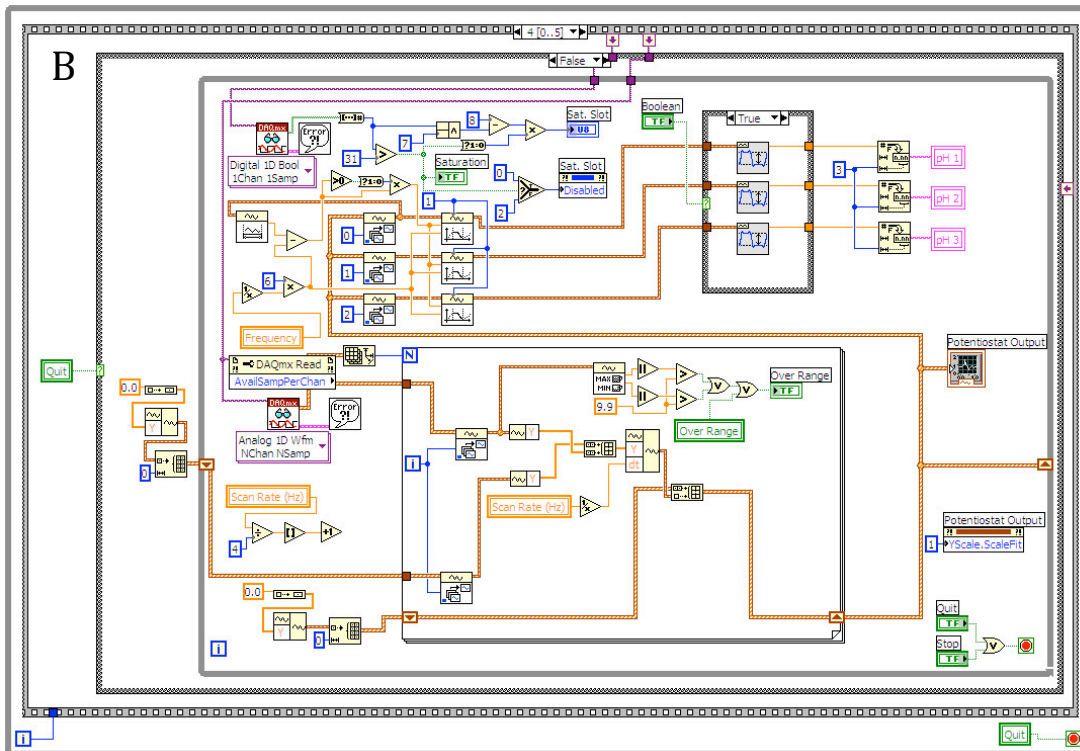
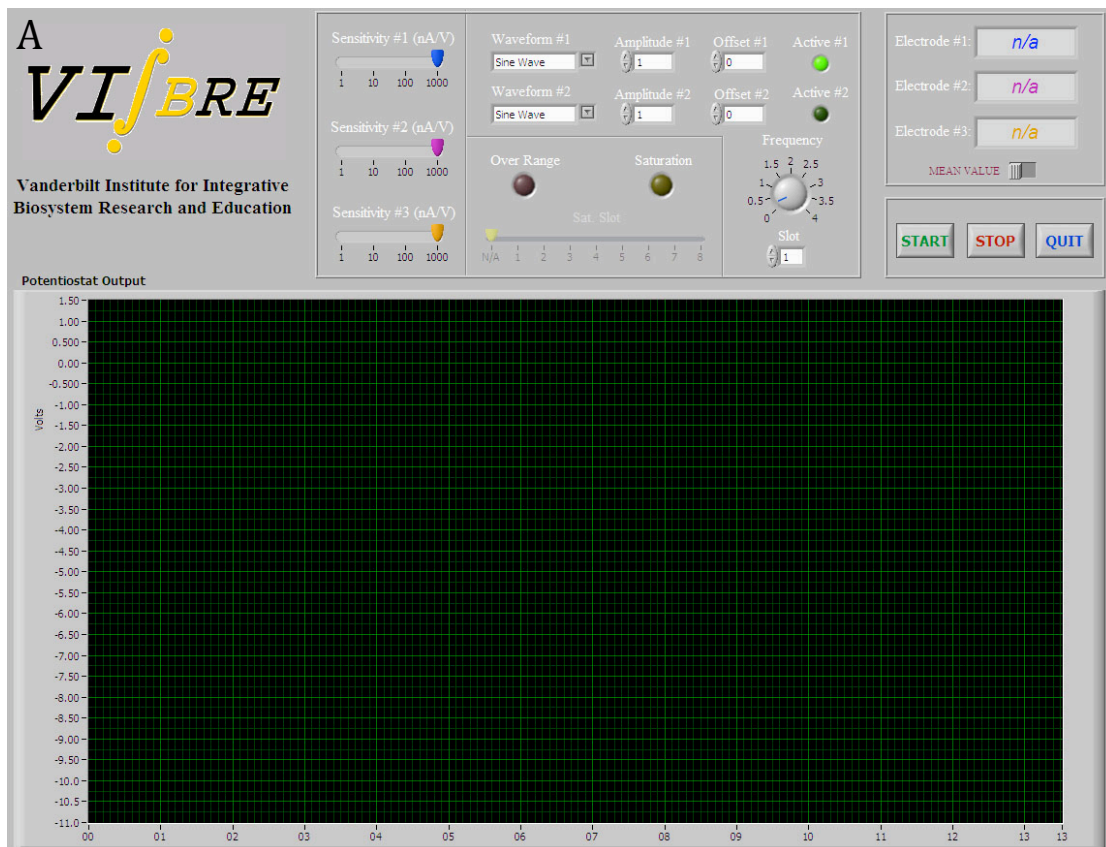
Figure 13. Current follower with four switchable resistors [Adapted from Bard]³³

Computer control

The MAMP system was controlled as described by Eklund with a Macintosh computer whose Cytosoft™ program controlled the pumps and temperature controls of the MAMP.¹⁶ A separate Pentium IV personal computer was used to control the multichannel multipotentiostat *via* National Instruments data acquisition (DAQ) cards and custom designed LabVIEW software. For four chamber MAMPs and multipotentiostats, either the PCI-6036E or PCI-6221 DAQ card was used, and in eight-channel systems PCI-6229 was used. Standard National Instruments shielded 68-pin cables (SH68-68-EP and SHC68-68-EPM) connected the DAQ cards to the configuration card of the potentiostat.

Software

LabVIEW software for the calibration of the multipotentiostat modules was written by Eduardo Lima. The front panel of this software is shown in Figure 14A, and a section of the block diagram which controls data acquisition is shown in Figure 14B.



LabVIEW software was also written for the multipotentiostat for multichamber amperometry experiments. A schematic flow diagram of the program is shown in Figure 15. Figure 16 shows the front panel of the program showing the user inputs of sensitivity, electrode potential, run time, sample rate, and sample name. The segment of the block diagram dealing with data collection and display is shown in Figure 17.

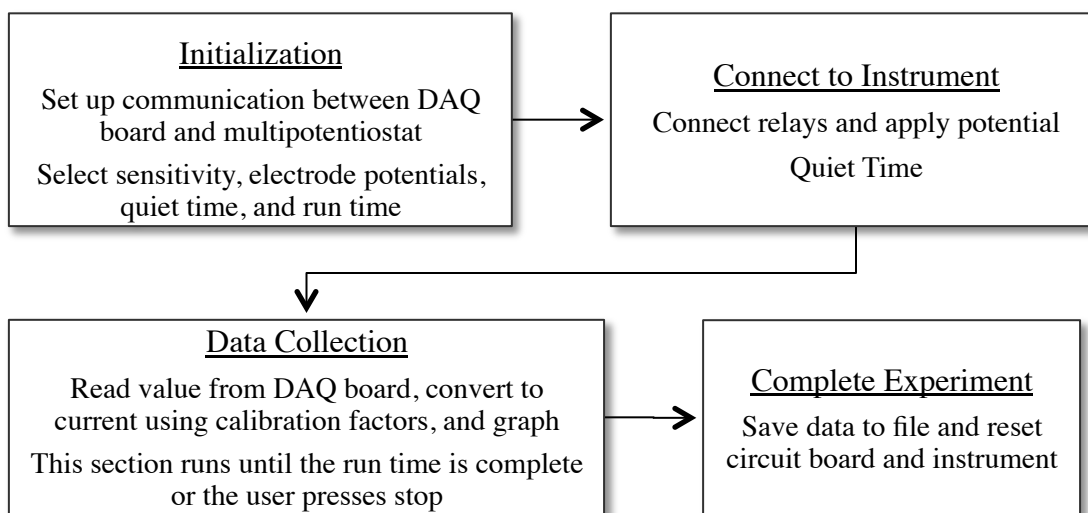


Figure 15. Flow diagram of data collection software for the multipotentiostat



Figure 16. User interface of the LabVIEW program written for the multipotentiostat for use with the MAMP

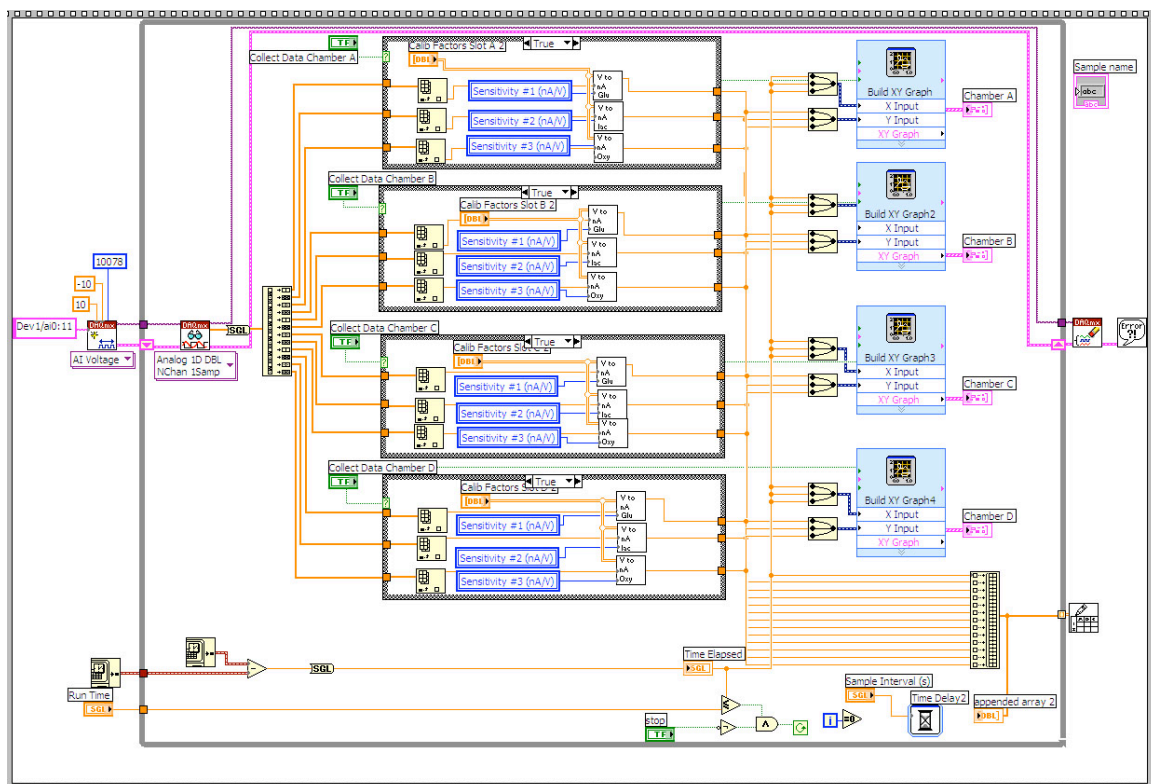


Figure 17. Portion of the block diagram of multipotentiostat software for the MAMP dealing with data collection, graphing, and saving to file

Calibration of the Multipotentiostat Modules

In order to calibrate each module of the multipotentiostat, a “dummy cell” comprised of four resistors, as shown in Figure 18, is used. The offset voltage of the DAQ card in applying a potential to the working electrodes must be determined. As this offset potential is applied to each individual multipotentiostat module slot, an average offset is found by measurement from each card. A single offset value was determined for working electrodes one and two, as the same potential is applied at both electrodes. A separate offset value is determined for working electrode three.

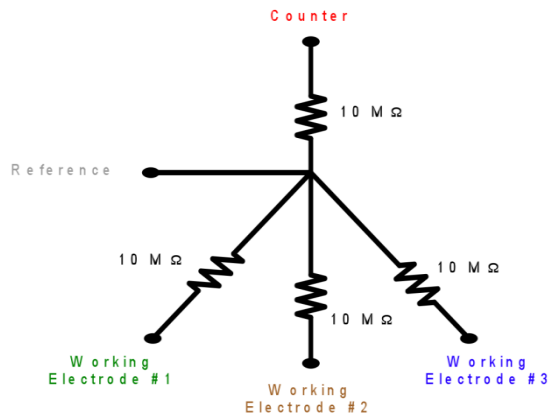


Figure 18. “Dummy cell” used in calibration of multipotentiostats

The determination of the specific feedback resistance, R_f , in each circuit is required to accurately convert voltages on the DAQ card back into amperometric currents. Based upon the sensitivity selected, one of four resistors, with value R_f , is connected to the current follower circuit, shown as R_1 through R_4 in Figure 13, with $V_o = -IR_f$, so that V_o remains between ± 10 V. By connecting a resistor of known resistance R_i of the dummy cell to the input and applying a known potential V_i , the value of R_f can be determined using the relationship, $V_o = -(R_f/R_i)*V_i$. The offset of the DAQ card response is included in the value of R_f calculated here. The value of R_f is then used to convert the voltage read on the DAQ card to the current measured at the working electrode.

Timing Studies

Tests were performed with the multipotentiostat and the MAMP to determine the reliability and high frequency noise using a sample rate of 1 Hz typical of MAMP experiments. Timing studies at higher frequencies were performed using dummy cells to allow testing without interfering with the LAPS of the MAMP. The dummy cells were

connected, and the amperometric response and noise backgrounds were measured at varying sample rates.

Amperometric Testing of the Multipotentiostat with the MAMP

Tests were performed with the multipotentiostat and the MAMP to measure the amperometric response and noise of the working electrodes of modified sensor heads, which are shown in Figure 9 in Chapter II. The sensors in the MAMP were tested with and without enzyme films, and with enzyme films in the presence of pheochromacytoma cells ($\sim 5 \times 10^5$ per insert, PC-12, CRL-1721 from the American Type Culture Collection (ATCC)). All MAMP protocols for cell cup and enzyme film preparation followed those given in Chapter II. Working electrode one (WE1) was coated with a glucose oxidase enzyme film, and working electrode two (WE2) was coated with a lactate oxidase enzyme film. WE1 and WE2 are 0.5 mm platinum electrodes. The 127 μm platinum electrode was working electrode 3 (WE3) and was left bare. Films were hand cast onto the surface of the platinum electrodes on the modified sensor heads and allowed to dry for 45 minutes before being used in the MAMP.

In these tests, working electrodes one and two were held at +0.6 V *vs.* the Ag/AgCl (2M KCl) reference of the MAMP. Working electrode three was held at -0.45 V *vs.* the Ag/AgCl (2M KCl) reference of the MAMP. All experiments were performed using 5 mM glucose modified RPMI 1640 media. In all experiments the sensors were calibrated with modified RMPI media with no glucose and no lactate, with 0.05 mM lactate and 1 mM glucose, with 0.1 mM lactate and 3 mM glucose, with 0.2 mM lactate and 5 mM glucose.

In the test of sensors without films and no cells, the sensors were placed into Corning Costar[®] Transwell[®] cup assemblies without cells, perfused with media, and the current response recorded. In the test with enzyme films but no cells, the sensors were placed into Corning Costar[®] Transwell[®] cup assemblies without cells; the current response was recorded as the chamber was perfused with media and the enzyme films on the sensors were calibrated. In the test with enzyme films and PC-12 cells, the sensors were placed into Corning Costar[®] Transwell[®] cup assemblies containing the cells and the current response recorded as the chamber was perfused with 5 mM glucose modified RPMI 1640 media for 45 minutes. The media was then changed to modified RPMI 1640 media containing 5 mM glucose and 101 μ M alamethicin. Once the cells were dead, the enzyme films of the sensors were calibrated.

Results and Discussion

Calibration

The offsets for each DAQ card and calibration factors for the instrument were determined. The offset values were found to be less than 60 mV for working electrodes one and two and less than 20 mV for working electrode three. These were then corrected for in the potential applied in the LabVIEW program. The calibration factors for the feedback resistances necessary for converting the measured voltage to a current were found to be within 10 % of the defined sensitivity, as expected given the tolerances of the resistors used. The R_f values determined for each module of a 4 chamber multipotentiostat are given in Table 1.

Table 1. Calibration values determined for a 4 chamber multipotentiostat

Expected value (nA/V)	Module 1			Module 2			Module 3			Module 4		
	WE1	WE2	WE 3	WE1	WE2	WE 3	WE1	WE2	WE 3	WE1	WE2	WE 3
1	1.056	0.9930	1.081	1.079	1.004	1.073	1.068	0.9977	1.078	1.028	0.9811	1.085
10	10.64	10.05	10.81	10.75	10.09	10.75	10.78	10.03	10.77	10.40	9.872	10.84
100	104.9	98.64	108.9	107.3	99.50	108.2	106.0	98.94	108.6	103.0	97.09	109.3
1000	1053	994.2	1079	1072	997.5	1078	1064	991.7	1082	1036	900.9	1085

Timing Studies

In a five hour thirty-five minute experiment in the MAMP with sample rate of 1 Hz, the average error in timing over the course of the experiment was 1.4 ms. For use in other experimental setups where there is not the issue of interference with the 10 kHz LAPS of the MAMP, sampling as fast as 10 Hz is possible with time steps of 0.100 ± 0.008 s.

Testing of Sensors in the MAMP

The amperometric response of a modified sensor head without films in the absence of cells is shown in Figure 19. The current response of working electrode one and two is very similar, which indicates that the electrodes of the modified sensor head are of similar area.

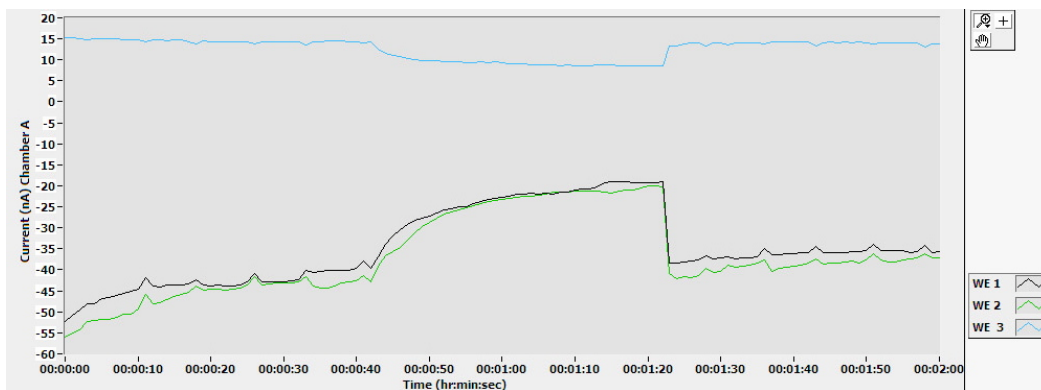


Figure 19. Current response of bare modified sensor head without cells present in modified RPMI 1640 media with 5 mM glucose

The amperometric response of a modified sensor head with enzyme films in the absence of cells is shown in Figure 19. When cells are absent and the chamber contains modified RPMI 1640 media containing 5 mM glucose, there is no stop flow signal on the lactate oxidase electrode (WE 2) and the magnitude of the oxidation current at the glucose oxidase electrode (WE 1) increases during stop flow. There is a linear calibration of both the glucose oxidase and lactate oxidase electrodes. The signals at the bare platinum oxygen electrode (WE 3) remain constant through out the experiment.

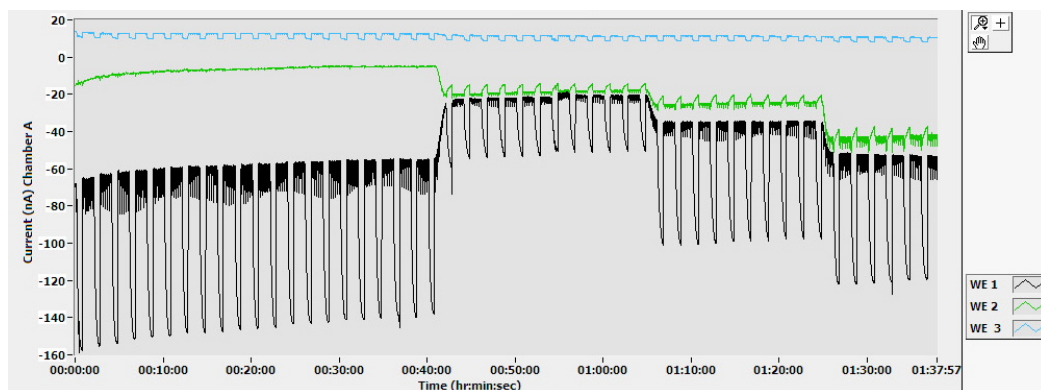


Figure 20. Current response at modified sensor head with WE1 coated with glucose oxidase, WE2 coated with lactate oxidase, and WE3 bare without cells present.

The amperometric response of a modified sensor head with enzyme films in the presence of cells is shown in Figure 21. In the presence of cells with media containing 5 mM glucose before they are treated with alamethicin, the magnitude of the oxidation current at the lactate oxidase electrode increases during the stop flow and the magnitudes of the currents at the glucose oxidase electrode and bare platinum oxygen electrode decrease during the stop flow. These results are consistent with lactate being produced and oxygen and glucose being consumed by the cells. At the end of treatment with

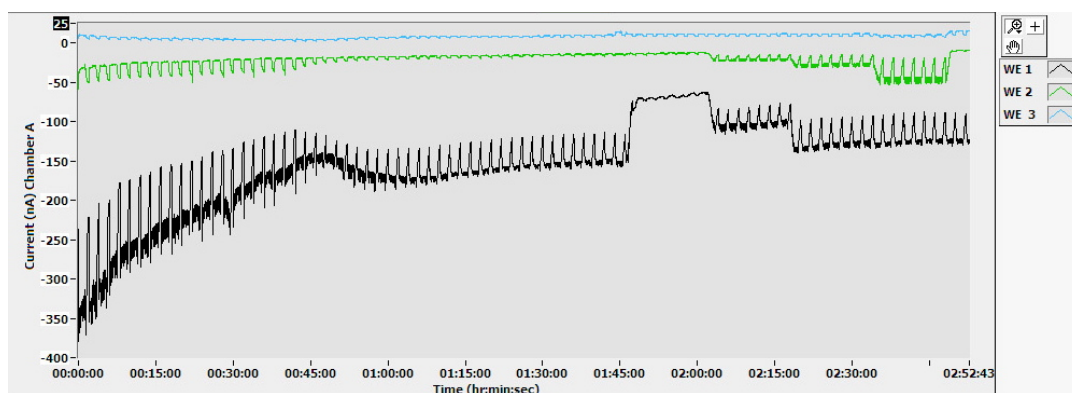


Figure 21. Current response at modified sensor head with WE1 coated with glucose oxidase, WE2 coated with lactate oxidase, and WE3 bare with 5×10^5 PC-12 pheochromacytoma cells.

current at the lactate oxidase electrode increases during the stop flow and the magnitudes of the currents at the glucose oxidase electrode and bare platinum oxygen electrode decrease during the stop flow. These results are consistent with lactate being produced and oxygen and glucose being consumed by the cells. At the end of treatment with alamethicin, when the cells have died, there is no longer a significant change in the current at the lactate oxidase electrode, and the decreases in the magnitude of the current at the glucose oxidase electrode and at the bare platinum oxygen electrode are less during

stop flow. These results are consistent with there being less glucose and oxygen consumed during the stop flow. This multichamber multipotentiostat has since been used in studies of cancer metabolism,^{70,71} islet physiology,^{72,73} and studies of the effects of toxins on cellular metabolism.¹⁷

Conclusions

We have developed a multipotentiostat capable of simultaneously measuring amperometric current response of three working electrodes in up to eight electrochemical cell chambers at a controlled bandwidth. This multipotentiostat works with sensitivities of 1, 10, 100, or 1000 nA/V, depending on the feedback resistor selected. The timing of the sample rate at 1 Hz has a low standard deviation of 1.4 ms over the course of a five and a half hour experiment, and data can be collected for as long as ten hours. Sampling frequencies as high as 10 Hz can also be used, when the LAPS is off, thereby eliminating the high frequency noise from crosstalk.

This multipotentiostat is applicable to any system requiring amperometric measurements in multiple electrochemical cells simultaneously, such as in an instrumented well plate. The only limitation is that the current design is limited to the application of two potentials; however, this is not a significant issue so long as two of the analytes have similar reduction or oxidation potentials.

The use of this multipotentiostat increases the number of MAMP chambers that could be measured simultaneously from 1 to 8, allowing for simultaneous testing of multiple cell types or exposures or simply allowing replicate experiments to be run

simultaneously. Currently efforts are underway to integrate new instrumentation modules for potentiometric measurements of pH and Ca^{2+} , such as in the work of Yicong.^{20,74}

Acknowledgments

I would like to acknowledge Eduardo Lima, a postdoctoral research associate, and Ron Reiserer, laboratory manager of the Vanderbilt Institute for Integrative Biosystems Research and Education, who built the multipotentiostat modules and performed electronics testing. Dr. Eduardo Lima also wrote software that was used to calibrate the DAQ cards used with the multipotentiostat.

CHAPTER IV

STUDIES OF ISLET METABOLISM IN THE MAMP

Introduction

The detection of insulin is important in the study of the metabolic function of islets, the cells that produce insulin. These cells, their function, dysfunction, and destruction, play a critical role in diabetes. Diabetes mellitus affects two hundred million people worldwide, six percent of the world's population.⁷⁵ Type I diabetes mellitus (T1DM) accounts for up to 10% of diabetes cases worldwide and occurs when the immune system attacks the insulin-producing cells of the pancreas.⁷⁶

The human pancreas is comprised of exocrine tissue that excretes digestive enzymes through ducts and endocrine tissue that releases hormones into the bloodstream. Endocrine function is performed by the islets of Langerhans, clusters of cells scattered throughout the exocrine tissue of the pancreas,⁷⁷ as shown in Figure 22.⁷⁸ Islets vary in size from less than 40 μm up to 400 μm in diameter as the number of cells varies from a few cells to 5,000 cells.⁷⁹

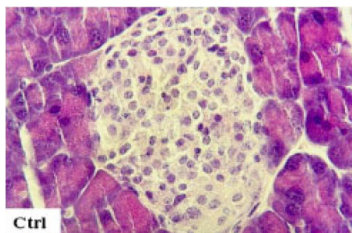


Figure 22. Pancreatic islet⁷⁸

* Snider, R. M.; Ciobanu, M.; Rue, A. E.; Cliffler, D. E. *Anal Chim Acta* **2008**, *609*, 44-52.
Ciobanu, M.; **Snider, R.M.**; Rue, A.E.; Chen, Z.; Powers, A.C.; Cliffler, D.E. (for submission to *Anal. Chem.*)

Islets are comprised of four main cell types: insulin-producing β cells, glucagon-producing α cells, somatostatin-producing δ cells, and pancreatic polypeptide-producing PP cells.⁷⁷ Human islets are normally comprised of approximately 54% β cells,⁸⁰ which are spread throughout the islet. Murine islets contain 85% β cells, which form the core of the islet.⁸¹ Insulin secretion by β cells can be stimulated by glucose, as well as other molecules such as amino acids, fats, and hormones.⁸² Glucose stimulated insulin secretion is described as biphasic, with an initial peak of concentration followed by increased release to reach a plateau.⁸³ A key event in glucose sensing is believed to be the phosphorylation of glucose by glucokinase (GK).⁸⁴ Insulin release can also be triggered by elevated levels of potassium and other nutrients.⁸⁵⁻⁸⁷

Insulin is synthesized within β cells in the form of pro-insulin, a single polypeptide chain containing the A and B chains and the C peptide linking region. Prior to being secreted, insulin is converted within the secretory granule from pro-insulin to insulin by removal of the C peptide.⁷⁹ As shown in Figure 23,⁸⁸ human insulin has a molecular weight of approximately 9 kDa and is comprised of 51 amino acids in two polypeptide chains with the A chain containing 21 amino acids.⁷⁷ The two strands are linked through two disulfide bonds with an intrastrand disulfide bond on the A chain.^{77,89}

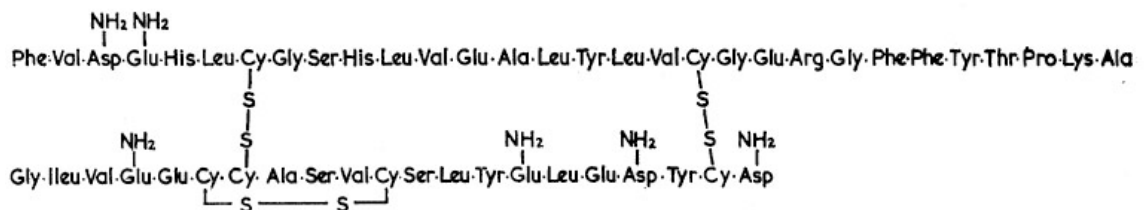


Figure 23. Human insulin showing the two interstrand and one intrastrand disulfide linkages⁸⁸

The current state of the art treatment for T1DM is based upon delivery of insulin using pumps to stabilize the levels of glycosylated hemoglobin. While this treatment is lifesaving, it is unable to completely prevent the development of medical complications of the eyes, kidneys, nerves, and blood vessels.⁹⁰ In some patients, even with this treatment can cause severe hypoglycemia, leading to potentially life-threatening outcomes.⁹¹ For these patients, as well as those who have undergone a kidney transplant and thus will be on life-long anti-rejection therapy, the transplant of insulin producing tissue, either whole pancreas or islets is a possible treatment.⁹¹ In 1993, the diabetes control and complications trial set forth a strong rationale for pancreas transplant;⁹² however, whole-organ pancreas transplant has significant risk of increased mortality.⁹¹

Early human islet transplantations were relatively unsuccessful with fewer than 12% of patients receiving islet allografts remaining insulin independent for more than a year, *i.e.* not requiring insulin injections.⁹⁰ In 2000, Shapiro reported successful islet transplantation for seven patients that resulted in insulin independence for all patients for an average of 11.9 months. A key factor in the reported success of this study, which came to be known as the Edmonton protocol, was the avoidance of corticosteroids in the immunosuppressive treatment of patients, following transplant.⁹³ Further studies have confirmed one-year insulin independence rates of 80% and three year islet graft function rates of approximately 90%, based on detection of C-peptide from the conversion of proinsulin to insulin.⁷⁵ A five year follow up with patients from the 2000 study by Shapiro showed that while 80% of the patients showed graft function only 10% remained insulin independent.⁹⁴ This unexpected decrease in graft function, along with the

withdrawal of the enzyme used in pancreas digestion by Roche in 2007, has led to decreased expectations of islet transplantation as a T1DM cure.⁹¹

The steps involved in pancreatic islet transplant are shown in Figure 24.⁹² First, the pancreas is harvested from a donor and subjected to collagenase digestion to separate islets from exocrine tissue. The pancreatic islets are then purified using density gradient centrifugation. Next, purified islets are injected into the liver of the recipient through the portal vein. As shown in Figure 24, islets become trapped within the sinusoids of the liver, where they perform their exocrine function.⁹²

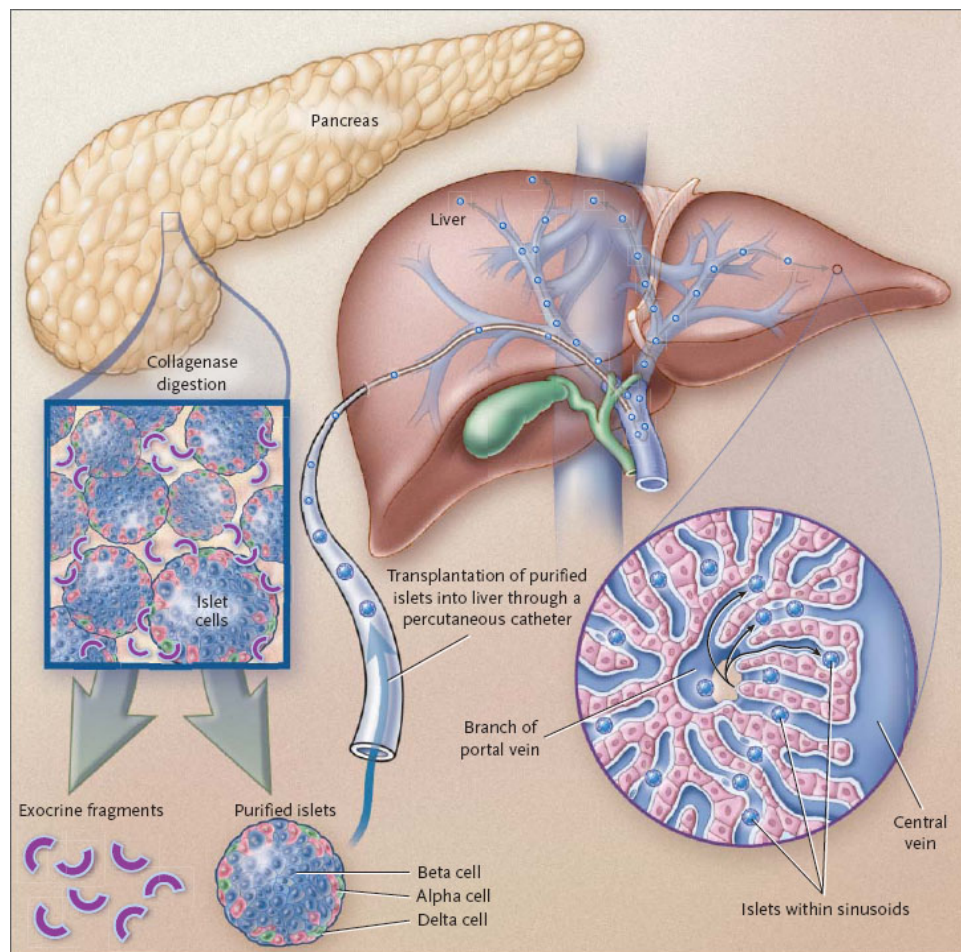


Figure 24. Procedure used in allogeneic islet transplantation⁹²

Since the 2000 study by Shapiro, there have been many advances in islet transplantation, particularly improvements in isolation procedures.⁷⁵ However, the standard characteristic in the evaluation of the health and function of isolated islets prior to transplantation is still the rate of insulin release, as determined by standard static or perfusion experiments.⁹⁵ Even in the most experienced isolation centers, more than 50% of islet mass can be lost during pancreatic digestion, purification and culture.⁹¹ Additionally, the long term use of immunosuppressant even with improved protocols is associated with toxicity to islets.⁷⁸ In order to address these issues, further *in vitro* study of the effect of digestion procedures and immunosuppressants on islet metabolism is warranted.

In a typical standard static test, two samples of 5 or 10 islets are incubated for a period of time, typically one to two hours, one sample in media containing a low concentration of glucose (2.8-3.3 mM) and the other sample in media with a high concentration of glucose (16.7-20 mM). The amount of insulin in the media is determined, and the stimulation index is calculated as the ratio of the insulin content in the high glucose media to the insulin content of the low glucose media.⁹⁶⁻⁹⁸ The stimulation index is used to quantify the insulin secreting capability of the islets; this measure is used in the analysis of islets for human transplants.⁹³ In perfusion experiments, islets are immobilized in a fluid path, such as between glass frits in a tube, and media is flown past. Typically, the islets equilibrate in low glucose media (~3 mM) for approximately 30 minutes to one hour, and then the glucose concentration is increased (~17 mM). Samples of the media outflow are collected throughout the experiment, every one to two minutes, and the insulin content is then determined to obtain a rate of insulin

release. The number of islets used in perfusion experiments varies from 5 to as many as 50.⁹⁹⁻¹⁰³ In perfusion experiments, the concentration vs. time profile of secreted insulin can be compared to the expected glucose stimulated insulin response for healthy islets.^{83,104} Both of these techniques require *ex situ* analysis of insulin content from collected samples, and as these methods necessitate testing of sample fractions, the true dynamic insulin release profile is not observed because time averaging occurs. Assay methods for the quantitative analysis of insulin in these samples include enzyme linked immunosorbent assay, radioimmunoassay, and chromatography. While these assays can have very low detection limits, these methods can be time consuming and require the labeling of insulin with either fluorescent tags or radioisotopes.¹⁰⁵⁻¹⁰⁷

Electrochemistry and fluorescence have also been used to quantify islet secretion with time resolution that reaches real-time in some cases; however, these studies primarily have involved detecting zinc, calcium or other molecules such as 5-hydroxytryptamine that play a role in insulin secretion.¹⁰⁸⁻¹¹² Maghasi *et al.*¹⁰⁸ detected secretion from β cells electrochemically through anodic stripping voltammetry of zinc at a bismuth-coated electrode. This study proposed that the amount of zinc detected correlated to the amount of insulin secreted since insulin is stored primarily in crystalline form with encapsulated zinc ions. However, this detection method required preconcentration and *ex situ* analysis of the β cell culture supernatant.¹⁰⁸ Kennedy and coworkers have been able to study insulin secretion by single islets in a microfluidic device through electrophoresis-based immunoassay of insulin¹¹¹ and also through fluorescence spectroscopy of zinc and intracellular calcium.¹¹⁰ While these techniques

have very low detection limits, they are unable to measure unlabeled native insulin directly.

Direct electrochemical detection of insulin is attractive as it can provide sensitivity and also reduced analysis times to enable continuous real-time measurements compared to the above methodologies. One of the first chemically modified electrodes developed to measure the oxidation of insulin was a ruthenium dioxide/cyanoruthenate film on a glassy carbon fiber electrode;¹¹³ however this electrode operated at pH 2, making it impractical for physiological measurements. A ruthenium dioxide/cyanoruthenate film on a carbon fiber microelectrode was later utilized at pH 7.4 to monitor chemical secretion by single β cells in response to stimulation with glucose, tolbutamide, and potassium.¹¹⁴ Redox mediators and electrocatalysts such as ruthenium oxide,¹¹⁵ ruthenium metallodendrimer,¹¹⁶ and iridium oxide¹¹⁷ layers have been shown to promote the oxidation of insulin at physiological pH and have been used in amperometric detection and quantization of insulin. However, iridium oxide sensors have the disadvantages of pH sensitivity resulting from the proton mediated nature of electron transfer and also the slow nature of proton transport within the film that delays the electrode response;¹¹⁸ ruthenium oxide and ruthenium metallodendrimer films have mixed redox states leading to complex electron transfer kinetics, with the electrochemical behavior of ruthenium oxide varying between crystal faces.¹¹⁹ While these sensors have been used to detect insulin electrochemically, they have limited stability of their mixed redox state surface films leading to loss of insulin sensitivity.

Because of the difficulties associated with the above chemically modified electrodes, multiwalled carbon nanotubes (MWCNTs) are an attractive possibility as an

electrocatalyst for the oxidation of insulin. MWCNTs are long, multi-walled, thin cylinders of carbon that can be described as several two-dimensional graphite sheets rolled into a tube.¹²⁰ Figure 25 shows a transmission electron micrograph of a MWCNT containing a concentric nested array of nine single walled nanotubes.¹²⁰

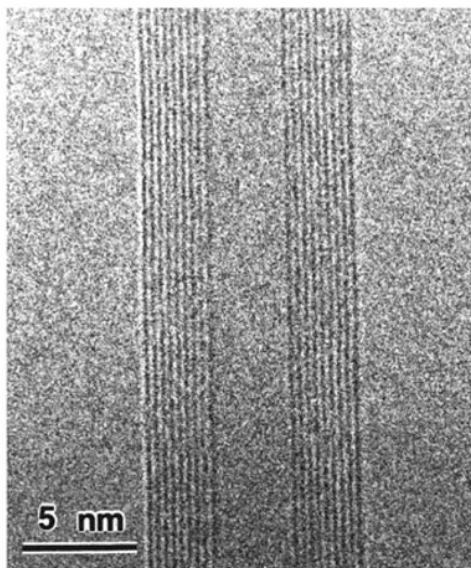


Figure 25. Transmission electron micrograph of a single MWCNT¹²⁰

Recent studies have shown the ability of MWCNTs to promote electron transfer reactions of both important biomolecules^{53,121} and redox centers embedded deep within proteins.^{122,123} This electrocatalytic property, as well as the chemical stability and high mechanical strength of MWCNTs, has rendered them an appealing material for use in biosensors.¹²⁴ Also, MWCNT-modified electrodes have been shown to reduce surface fouling effects, like those seen in NADH oxidation at highly ordered pyrolytic graphite electrodes.¹²⁵

The direct oxidation of insulin with high sensitivity in physiological pH using a MWCNT modified glassy carbon electrode (GCE) cast from a suspension in *N,N*-

dimethylformamide (DMF) was reported by Wang and Musameh.¹²⁶ No cross-linking agent or polymer was used in the preparation of this film. Because the film was produced upon the evaporation of DMF, there was little control of film morphology leading to agglomeration of the MWCNTs. Recent improvements by Wang and co-workers include a combination carbon nanotube/ruthenium oxide electrode.¹²⁷ Wu *et al.* reported that the stability of MWCNT films for the detection of small biomolecules is improved by addition of a fatty acid such as dihexadecyl phosphate to an aqueous suspension of MWCNTs.¹²⁸ Gorski *et al.* recently explored the use of a chitosan MWCNT composite film for insulin oxidation.¹²⁹ The addition of the polysaccharide chitosan was seen to facilitate the preparation of films for electrochemical sensors, but these sensors were not coupled to microfluidic analysis nor used for direct insulin measurements on islets. The preparation of the chitosan-based film includes the use of an acid solution at 80–90 °C and results in a film up to 10 μm thick.¹²⁹ In our microphysiometer setup, a thick film may prove an impediment in the microfluidic thin layer cell where the volume of the microfluidic chamber is 3 μL . The use of a small molecule, such as dihydropyran (DHP), as a stabilizing agent for the MWCNT film should result in a simpler preparation as DHP is simply added to the aqueous suspension. DHP is a vinyl ether that has been shown to self-polymerize,¹³⁰ and therefore has the ability to form a thinner stabilizing network for adhering the MWCNTs to the glassy carbon surface.

An electrochemical insulin sensor would be ideally suited for use in the physiological detection of insulin in a microfluidic device, such as the MAMP, which is described in more detail in Chapter II. In the MAMP, as in all microfluidic devices, the

film electrodes must be able to withstand the shear forces generated in the detection chamber.

In this chapter, we present an insulin sensor for electrochemical detection in a microfluidic device based on direct oxidation at a MWCNT/DHP composite film at physiological pH. Compared to sensors in literature, our sensor has improved surface coverage and adherence to the electrode surface. We have successfully adapted this sensor for the microfluidic chamber of the MAMP and used it to record the response of isolated murine islets to glucose stimulation, as well as nutrient stimulation.

Experimental

Chemicals

All materials were used as obtained unless otherwise noted. Insulin (from bovine pancreas, 27 USP units/mg), and dihexadecyl phosphate were purchased from Sigma. The insulin content appeared to vary as much as 20% between commercial lots. 3,4-Dihydro-2H-pyran (DHP), Tween-80, and DMF were purchased from Acros. Cell-Tak™ cell and tissue adhesive was purchased from BD Biosciences. Glassy carbon rods (1 mm diameter) were obtained from Structure Probe, Inc. (West Chester, PA). Platinum rod (2 mm) was purchased from VWR. All microphysiometer consumables were purchased from Molecular Devices (Sunnyvale, CA).

Insulin solutions were prepared from a stock of 10 mg/mL solution of insulin in 19.6 mM hydrochloric acid containing 0.02% v/v Tween-80. Dilutions were then made in 50 mM phosphate buffer (pH 7.4, 0.02% v/v Tween-80) immediately before use in experiments. Male FVB (Friend leukemia virus B) mice were made available by the Islet

Isolation Core of the Vanderbilt Diabetes Research and Training Center. FVB mice have been used previously as control models for basal levels in a number of studies of the effect of gene modification on insulin secretion.¹³¹⁻¹³³ Islets were isolated from these mice by Dr. Zhongyi Chen of the Islet Isolation Core of the Vanderbilt Diabetes Research Training Center as described by Brissova *et al.*¹³⁴ The islets were cultured overnight in RPMI with 10% fetal bovine serum and 11 mM glucose. Upon receipt the islets were stored in an incubator at 37 °C and 5% CO₂ until use.

MWCNTs were obtained as a gift from Dr. William Hofmeister and were manufactured as a byproduct of diamond deposition by microwave assisted chemical vapor deposition using an iron catalyst. An Astex Large Area Diamond Deposition System with a 5 kW microwave source was used. Nanotubes were purified through treatment with nitric acid, following the method of Dujardin *et al.*,¹³⁵ to remove the remaining catalyst and aggregates. Following purification, the nanotubes were stored in a desiccator.

Apparatus

All electrochemical measurements, with the exception of amperometric tests in the MAMP, were conducted using a CHI 660a potentiostat from CH Instruments (Austin, TX). The electrochemical cell was used in a three electrode configuration with 3 mm GCE working electrode CHI104 (CH Instruments Austin, TX), Ag/AgCl (2 M KCl) reference electrode CHI 111 (CH Instruments Austin, TX), and platinum mesh counter electrode in all experiments but those in the MAMP. In the MAMP, the 2 mm platinum disk on the modified sensor head (Figure 26) was used as the counter and the 1 mm

glassy carbon electrode was used as a working electrode, while the reference electrode (Ag/AgCl, 2 M KCl) was downstream from the microfluidic chamber, as is typical in the Cytosensor[®]. For amperometric tests in the MAMP, a four channel microphysiometer and Cytosoft[®] program (Molecular Devices) were used to control pump cycles. The multipotentiostat described in Chapter III was used to measure the current response in MAMP experiments.

Sensor Head Construction

For insulin determination in the MAMP, a sensor head was constructed with a 1 mm GCE, a 0.5 mm platinum working electrode, a 127 μm platinum working electrode, and a 2 mm platinum counter electrode, as described in Chapter II. The GCE was connected to platinum wire with silver epoxy to allow electrical connection. All electrodes were sealed with Hysol[®] Epoxi-Patch and polished until flush with the surface. The schematic of the modified sensor head can be seen in Figure 26.

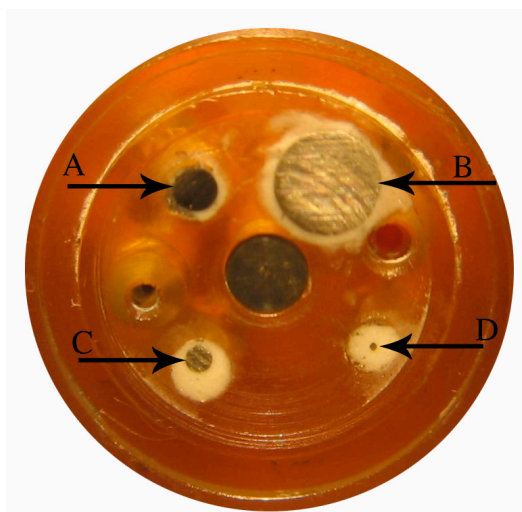


Figure 26. Modified sensor head with 1 mm GCE (A), 2 mm (B), 0.5 mm (C), and 127 μm (D) platinum electrodes

Modified Electrodes for the Detection of Insulin

All films were formed by drop casting the suspension on to the electrode surface, with 20 μL used for a 3 mm GCE and 3 μL for a 1 mm sensor head GCE.

MWCNTs cast from DMF: A 10 mg/mL suspension of carbon nanotubes in DMF was sonicated for one hour.¹²⁶

MWCNT/dihexadecyl phosphate: A 10 mg/mL suspension of MWCNT in water was prepared with a 1:1 mass ratio of MWCNT:dihexadecyl phosphate. The suspension was sonicated for one hour.¹²⁸

MWCNT/DHP: A 10 mg/mL suspension of MWCNT in water was prepared with a 1:1 mass ratio of MWCNT:DHP. This suspension was sonicated for fifteen minutes.

Testing of Films for Insulin Sensitivity

Cyclic voltammograms (CVs) were obtained for each electrode film on the 3 mm GCE and 1 mm GCE of the modified sensor head in 50 mM phosphate buffer (pH 7.4, 0.02% v/v Tween-80) with and without insulin, from 0 to 1 V at a scan rate of 50 mV/s. The MWCNT/DHP film on the 3 mm GCE was also calibrated outside of the MAMP in a batch test. After ~1 hour of electrode conditioning at +0.88 V vs. Ag/AgCl (2 M KCl) in 50 mM phosphate buffer (pH 7.4, 0.02% v/v Tween-80), aliquots of buffer and insulin were injected to give concentrations of 0, 1.97×10^{-7} , 3.94×10^{-7} , 6.87×10^{-7} , and 9.79×10^{-7} M insulin. The resulting data was filtered using a LabVIEW program with a Fourier transform low pass filter to remove the electromagnetic stirring noise.

To test the suitability of these films for use in the MAMP, the 1 mm sensor head GCE was coated with one of the three film types and then placed in the MAMP for 4.5

hours under stop flow conditions with a cycle of 180 s with a flow rate of 20 $\mu\text{L}/\text{min}$ for 140 s and a 40 s stop flow period. The condition of the films was observed using an optical microscope before and after testing. Linear sweep voltammetry (LSV) in solutions of buffer and insulin was performed with a scan rate of 50 mV/s in the microphysiometer for films on the sensor head GCE at a constant flow rate of 20 $\mu\text{L}/\text{min}$. The MWCNT/DHP composite film was then calibrated amperometrically on the modified sensor head in the MAMP with ~ 1 hour of electrode conditioning following the same method used in the batch test of the film on the 3 mm GCE, with concentrations of 0, 1.001×10^{-6} , 5.002×10^{-6} , 1.001×10^{-5} , 2.501×10^{-5} M insulin.

Testing of Islets in the MAMP

The polycarbonate membranes of the Cytosensor[®] capsule cups were coated with Cell-Tak[™], a combination of proteins from mussels. The cups were dried at 37 °C, rinsed with water, and dried again. Approximately 75-125 islets were hand picked from the culture media using a manual pipette, rinsed three times with 1 mM phosphate buffer with 100 mM NaCl (pH 7.0), and then placed onto the Cell-Tak[™]. The islets were then coated with 5 μL of agarose following a well established protocol for the use of non-adherent cells in the Cytosensor[®].^{21,136,137} A spacer and insert were placed inside the cup. Hank's balanced salt solution (HBSS)¹³⁸ with 2.8 mM glucose was pipetted inside. For all islet experiments, the glassy carbon electrode was coated with 3 μL of 10 mg/mL suspension of MWCNT in water with a 1:1 mass ratio of MWCNT:DHP. The 0.5 mm platinum electrode was coated with a solution of lactate oxidase and bovine serum albumin in pH 7 phosphate buffer. Both films were allowed to dry for 45 minutes. These

two electrodes were held at a potential of +0.88 V vs. Ag/AgCl (2 M KCl) during islet experiments. The 127 μm platinum working electrode was coated with a layer of Nafion (perfluorosulfonic acid-PTFE copolymer, 5% w/w solution in ethanol). This electrode was held at -0.45 V vs. Ag/AgCl (2 M KCl) during islet experiments

The capsule containing the islets was then placed in the MAMP, and the Cytosoft[®] data collection and pump control program started. The islets were allowed to equilibrate for 20 minutes in the MAMP at 37 °C at a flow rate of 20 $\mu\text{L}/\text{min}$, before data collection of insulin commenced. The pump cycle for islet experiments was 180 seconds, with 140 seconds at flow rate of 20 $\mu\text{L}/\text{min}$ and a 40 second stop flow period. To validate that the sensor can detect glucose stimulated insulin secretion, islets were initially perfused with HBSS with 2.8 mM glucose, referred to as low glucose. After 45 minutes, the perfusion media was switched to HBSS with 16.7 mM glucose, referred to as high glucose, for 42 minutes. The media was switched back to low glucose for 33 minutes, to high glucose for 66 minutes, and then back to low glucose.

Identical procedures were followed in the absence of islets to determine the effect of increased glucose levels on the sensor.

Potassium stimulated insulin secretion was also studied. In these experiments, islets were initially perfused HBSS with low glucose for 45 minutes, HBSS with high glucose for 45 minutes, HBSS with low glucose for 30 minutes, HBSS with high glucose for 45 minutes, HBSS with low glucose for 30 minutes, HBSS with 2.8 mM glucose supplemented with 50 mM potassium for 48 minutes, and then returned to HBSS with low glucose. Identical procedures were followed in the absence of islets to determine the effect of increased glucose levels on the sensor.

Results and Discussion

We present the development of a MWCNT/DHP composite film and its use in a microfluidic chamber inside the MAMP, yielding a sensor capable of detecting insulin secretion from islets and study of islet metabolism as a whole. This film was compared with established electrochemical insulin sensors based on MWCNTs, namely the MWCNT film cast from DMF of Wang and Musameh¹²⁶ and the MWCNT/dihexadecyl phosphate composite films of Wu *et al.*¹²⁸ As this sensor has been designed for use in the MAMP, uniformity of coating and adherence of the film to the electrode surface are vital.

Figure 27 presents a preliminary comparison of these three film types. CVs were obtained in buffer (pH 7.4, 0.02% v/v Tween-80) as background and in insulin solutions (72.5 μM) prepared in the same buffer. As displayed in Figure 2A, a representative CV using the MWCNT film cast from DMF shows an irreversible oxidation peak at +0.759 V vs. Ag/AgCl, 2 M KCl, which is well resolved from the background buffer. The CV using the MWCNT/dihexadecyl phosphate film, solid line in Figure 2B, has an oxidation

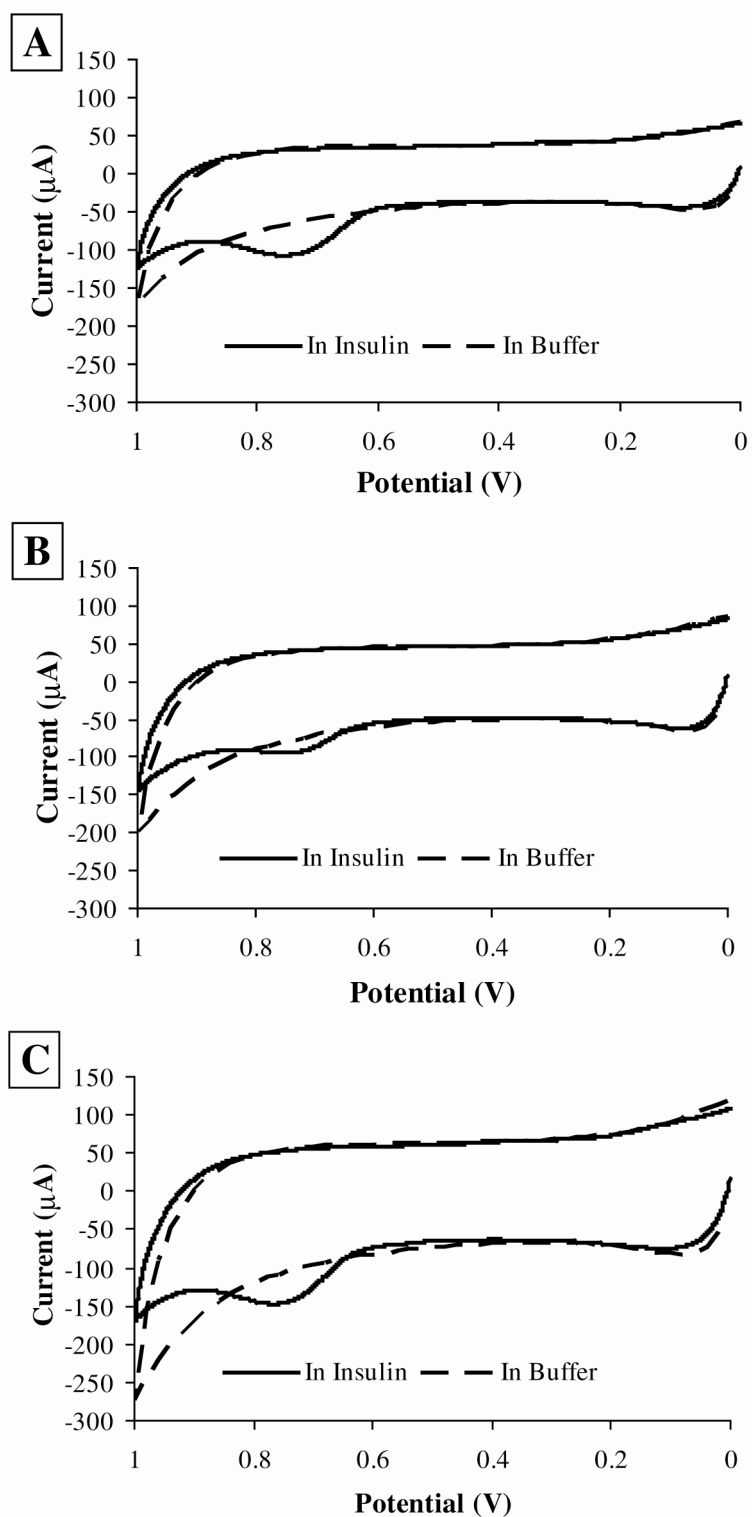


Figure 27. Cyclic voltammograms in 50 mM phosphate buffer (pH 7.4, 0.02% v/v Tween-80) and 72.5 μM insulin solutions in the same buffer at a 3.0 mm GCE coated with each film type vs. Ag/AgCl (2 M KCl). Scan rate: 50 mV/s. (A) MWCNT cast from DMF; (B) MWCNT/dihexadecyl phosphate electrode; (C) MWCNT/DHP electrode.

peak at +0.753 V vs. Ag/AgCl, 2 M KCl, and is not as well defined as the insulin oxidation peak for the MWCNT film cast from DMF or the MWCNT/DHP film. Because of the decreased magnitude of the insulin oxidation peak, the MWCNT/dihexadecyl phosphate film is the least desirable choice for use in insulin detection. The oxidation peak of insulin for the cyclic voltammogram of the MWCNT/DHP composite film, solid line in Figure 2C, has a peak potential of +0.765 V vs. Ag/AgCl, 2 M KCl, and is well defined compared to the background voltammogram in buffer (dotted line). The average peak current as a function of insulin concentration for cyclic voltammograms of each film is given in Table 2.

Table 2. The insulin oxidation peak currents from cyclic voltammograms of 1 mm GCEs modified with MWCNT cast from DMF, MWCNT/dihexadecyl phosphate films, and MWCNT/DHP films and the ratios of the peak current to the insulin concentration^a

Film Type	E_p (V vs. Ag/AgCl)	i_p (μ A)	C (μ M)	i_p/C (μ A/ μ M)
cast from DMF	0.759	59 \pm 5.0	72.5	0.81 \pm 0.07
dihexadecyl phosphate	0.753	35 \pm 3.3	72.5	0.48 \pm 0.05
DHP	0.765	61 \pm 4.9	72.5	0.84 \pm 0.06

^aCVs were run with scan rate of 50 mV/s and a Ag/AgCl (2 M KCl) reference electrode in insulin solutions in 50 mM phosphate buffer (pH 7.4, 0.02% v/v Tween-80). At least three CVs were obtained for each film type.

The electron transfer kinetics, as indicated by the oxidation peak current divided by the insulin concentration, i_p/C , for the MWCNT film cast from DMF and the MWCNT/DHP composite film, were improved compared with the values for the MWCNT/dihexadecyl phosphate film. All three films show oxidation at similar potentials (Table 2), with the sensitivity of the MWCNT/dihexadecyl phosphate film being the lowest. The large

standard deviations in the peak current values in Table 2 result from each film being hand cast. For this reason, each film must be calibrated individually prior to any experiments that involve insulin detection. By comparing the oxidation peak current as a function of concentration, it is clear that the MWCNT/DHP film and the MWCNT film cast from DMF have the best current response and kinetics and thus are the best leads for the detection of insulin from physiological samples; however, further testing is necessary to determine which film was most suitable for the microfluidic environment of the MAMP.

To determine the resistance to shear force of these three film types under the microfluidic flow conditions of the MAMP, sensor head GCEs (Figure 26) were coated and tested under identical conditions. Representative films for each film type are shown in Figures 28A-C before testing and in Figures 28D-F after testing. Prior to testing in the MAMP, all three films appear to have complete surface coverage with some surface roughness seen in the MWCNT/dihexadecyl phosphate and MWCNT/DHP films. After 4.5 hours in the MAMP under stop flow conditions with 180 s cycles with a flow rate of 20 $\mu\text{L}/\text{min}$ for 140 s and a 40 s stop flow period, the thicknesses of the MWCNT film cast from DMF and the MWCNT/dihexadecyl phosphate film, Figure 28D and 28E, are clearly reduced. The adherence and integrity of the films were compared by using the pre- and post-testing images and visually inspecting the optical density of the film remaining as the percentage of its original area. The ratio of the remaining film to the area of original film is defined as the percentage of film loss. The MWCNT film cast from DMF lost 53.6% of its original coverage. The loss of the MWCNT/dihexadecyl phosphate film was more dramatic, with a loss of 90.2% of the original film area. In

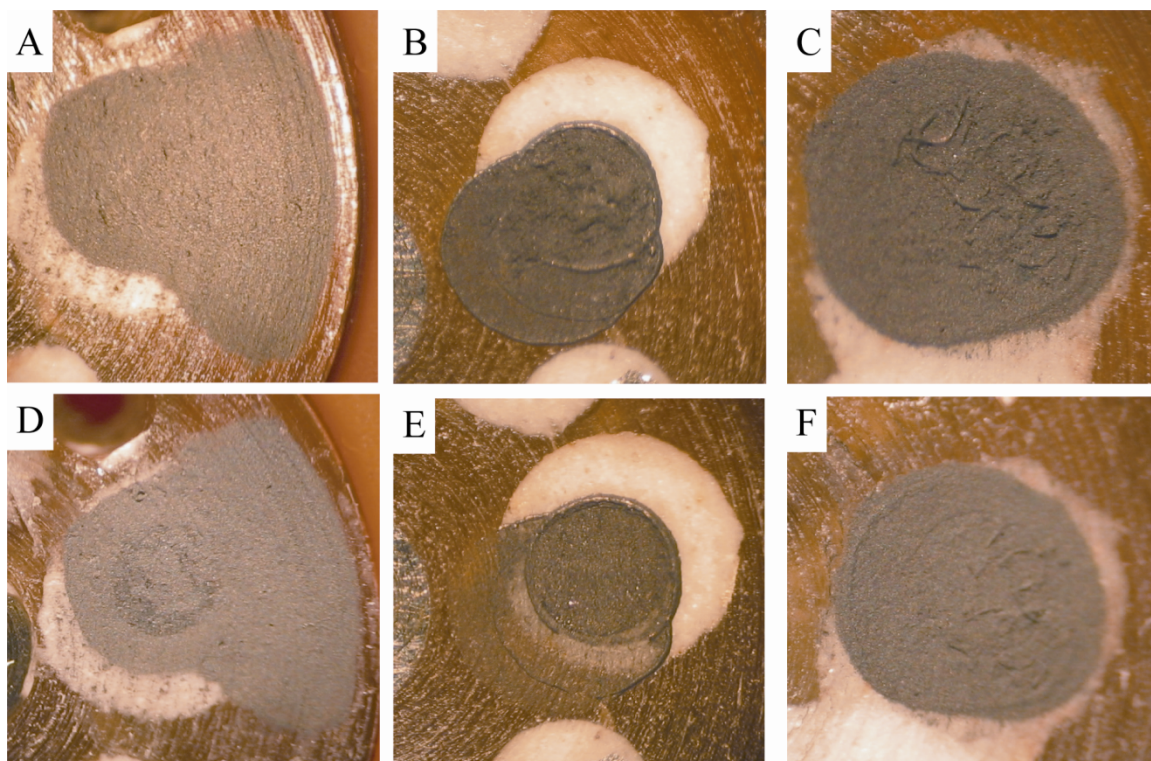


Figure 28. (A-C) Optical microscope images of MWCNT films on modified sensor head (A) Cast from DMF, (B) MWCNT/dihexadecyl phosphate, and (C) MWCNT/DHP (D-F): Same films after 4.5 hours of testing in the MAMP (D) Cast from DMF, (E) MWCNT/dihexadecyl phosphate film, and (F) MWCNT/DHP film.

comparing Figures 28C and 28F, visual inspection showed that none of the MWCNT/DHP film was lost, although some surface changes were observed. The MWCNT/DHP film maintained its integrity and had the best adherence to the electrode surface during the pulsed stop flow conditions in the MAMP out of the three film types tested. The MWCNT film cast from DMF and the MWCNT/dihexadecyl phosphate film are only physisorbed onto the electrode surface, while MWCNT/dihexadecyl phosphate film shows increased homogeneity of the MWCNT film resulting from the addition of a fatty acid to the suspension. In the case of the MWCNT/DHP film, there is physical crosslinking of the nanotubes from the self-polymerization of DHP.¹³⁰ Therefore, although the MWCNT/DHP film and the MWCNT film cast from DMF showed similar

i_p/C values (Table 2), the MWCNT/DHP film is best suited for use in the MAMP as it can better withstand the fluidic shear forces of the instrument, and consequently was used in all future experiments.

LSVs of the MWCNT/DHP composite film were also obtained in the MAMP to verify that the MWCNT/DHP composite film on the 1 mm glassy carbon electrode of the sensor head still has the ability to electrochemically detect insulin in a microfluidic system similar to the preliminary tests of Figure 27. Sample LSVs of the MWCNT/DHP composite film on the glassy carbon electrode of the modified sensor head in buffer and 300 μM insulin are shown in Figure 29. In the presence of insulin, a peak appears around +0.81 V *vs.* Ag/AgCl, 2 M KCl demonstrating the oxidation of insulin at the MWCNT/DHP composite film on the GCE of the modified sensor head in a microfluidic device. This experiment indicates that the MWCNT/DHP film preserves electrochemical activity in the MAMP (Figure 29) similar to that of preliminary experiments (Figure 27).

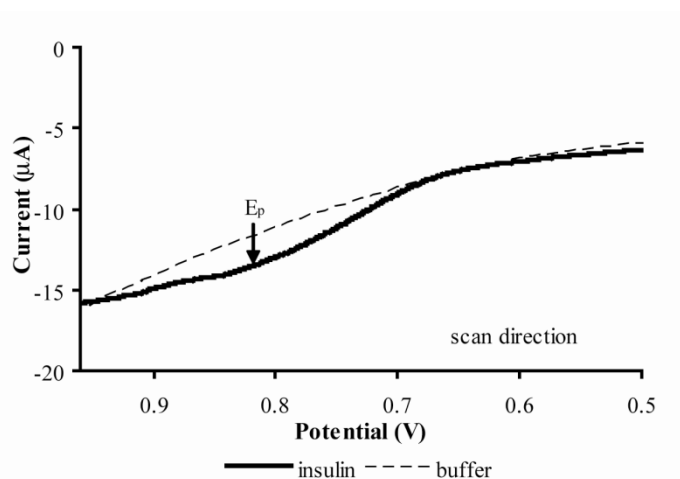


Figure 29. Linear sweep voltammograms of 300 μM insulin in 50 mM phosphate buffer (pH 7.4, 0.02% v/v Tween-80) and of blank buffer at a 1 mm GCE on the modified sensor head coated with MWCNT/DHP composite film *vs.* Ag/AgCl (2 M KCl) in the MAMP. Scan rate: 50 mV/s

Amperometric calibrations were performed on MWCNT/DHP films at +0.88 V vs. Ag/AgCl, 2 M KCl on both 3 mm GCEs in solution under moderate stirring and the 1 mm GCE of the modified sensor head in the MAMP. The blank and insulin solutions were in 50 mM phosphate buffer (pH 7.4, 0.02% v/v Tween-80). The current increase as a function of insulin concentration is given in Figure 30A for three distinct MWCNT/DHP sensor films on a 3 mm GCE, with each point on the graph representing twenty seconds or 200 collected data points. The similarity of the slopes for these three calibrations, given in the equations in Figure 30A, suggests that the sensitivity of the films is comparable, indicating the reproducibility of these films.

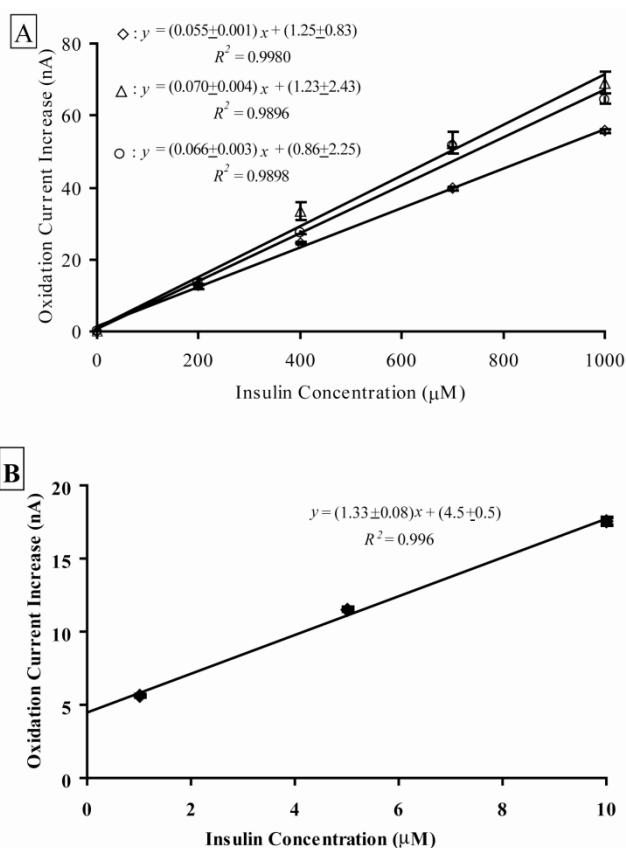


Figure 30. Insulin calibration curves of MWCNT/DHP films at +0.88 V vs. Ag/AgCl (2 M KCl). (A) Calibration curves of three different films on 3 mm GCEs (B) Calibration curve of a single film on a 1 mm GCE of a modified sensor head in the MAMP

An amperometric calibration of the MWCNT/DHP film in the MAMP was performed to ensure that the limit of detection is within the expected physiological concentration range. The current increase during flow as a function of insulin concentration increase is given in Figure 30B. Each calibration point on the graph represents at least five stop flow cycles, comprising 700 collected data points. Each film must be calibrated individually to account for variation in electrode coating due to manual handcasting of the MWCNT/DHP suspension. The current increase for the blank of buffer (0 μM insulin) was not visible above the peristaltic noise of the sensor. The presence of the large y-axis intercept in Figure 30B is due to the same peristaltic pump noise. We were able to detect changes in insulin concentration as low as 1 μM during calibration experiments, which falls within the expected physiological range. As there are no literature values for the secretion of insulin from islets of male FVB mice, for comparison purposes the values determined in Bergsten's study of individual islets isolated from *ob/ob*- mice were used. Insulin was measured using perfusion assay with subsequent quantitation using ELISA, where insulin release of $3 \pm 1 \text{ pmol g}^{-1} \text{ s}^{-1}$ was observed when the glucose concentration was 3 mM with an increase to $99 \pm 10 \text{ pmol g}^{-1} \text{ s}^{-1}$ upon stimulation with 16 mM glucose.¹⁰⁴ By extrapolating this data using the reported islet weight range of 8 – 15 μg and the MAMP volume of 3 μL , approximately 75–125 islets, and stop flow of 40 seconds, a concentration range of 24–75 nM could be expected at the end of the stop flow period for low glucose and a range of 0.8–2.5 μM for high glucose. While this value is for *ob/ob*- mice, it is expected that the value could be larger for the FVB mice used in our studies, as islet function is impaired in *ob/ob*- mice.

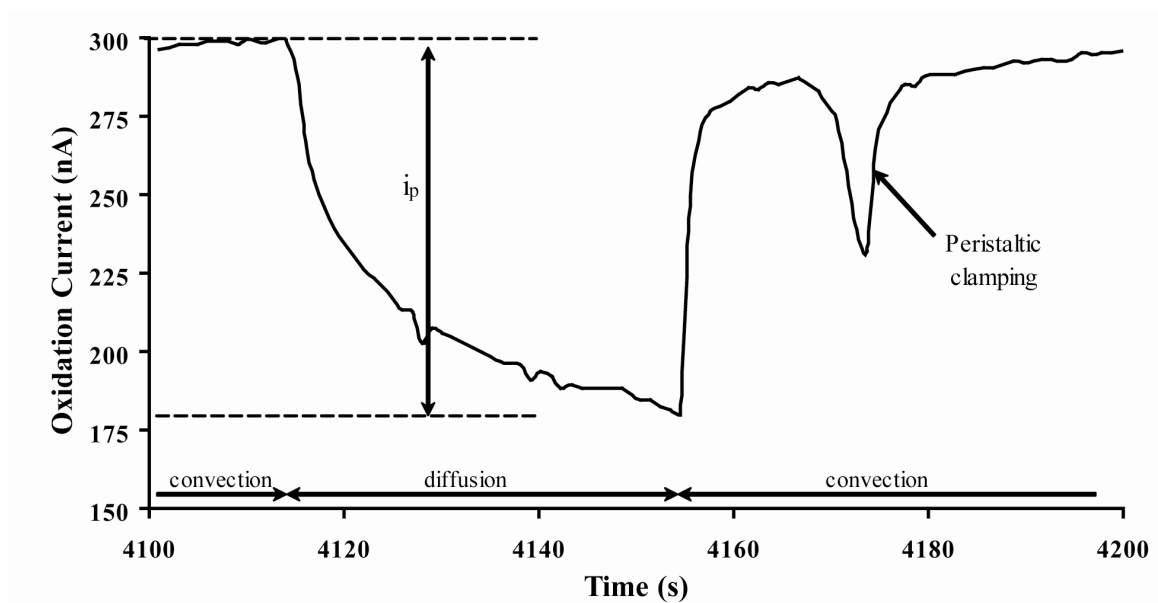


Figure 31. Typical flow – stop flow amperometric current profile of a MWCNT/DHP sensor film in MAMP at + 0.88 V vs. Ag/AgCl (2M KCl) showing the pump on/off periods, peak current (i_p) and peristaltic pump clamping spike.

To demonstrate the suitability of the MWCNT/DHP film in the MAMP for studying insulin with physiological samples, the response of the sensors in the presence of islets was measured. Figure 31 shows the amperometric current/time profile of a MWCNT/DHP composite film electrode during a typical stop-flow period in the presence of insulin secreting islets and the dynamics of the signal upon restart of flow. Also visible in Figure 6 is the spike in current corresponding to the perturbation in microfluidic flow caused by the peristaltic pump clamping. The shape of the current-time profile is the result of convective mass transfer during flow as well as decreased mass transport resulting only from diffusion during stop flow, when the secreted insulin must diffuse to sensors across the 100 μm gap of the microfluidic chamber. The peak height (i_p), which was used in data analysis, is measured from convective flow steady-state current to the minimum of the stop flow diffusional current as shown in Figure 31. One reason for

using i_p in data analysis is that the stop flow data has a higher signal to noise ratio and lower detection limits than the convective flow data even after filtering out the high frequency noise of the peristaltic pump from flow data. The current at the sensor during stop flow is linear when graphed vs. $t^{-1/2}$, indicating that the time dependence profile of the insulin release results from diffusional mass transport from the cells to the sensor. This will be the focus of future studies and could likely be modeled as a two electrode system as analyzed by Bard and Faulkner.³³ Currently, peak height at the end of the stop flow phase is the most accurate way to analyze the insulin sensor data with islets as it represents the maximum physiological activity measured during the stop flow period.

Confirmation of the detection of glucose stimulated insulin secretion from pancreatic islets is demonstrated in Figure 32, which shows the raw amperometric current response of the MWCNT/DHP sensor film in the presence of islets with 2.8 and 16.7 mM glucose. In this experiment, switching the glucose concentration in the HBSS media from low (2.8 mM) to high (16.7 mM) was used to stimulate insulin secretion by the islets.

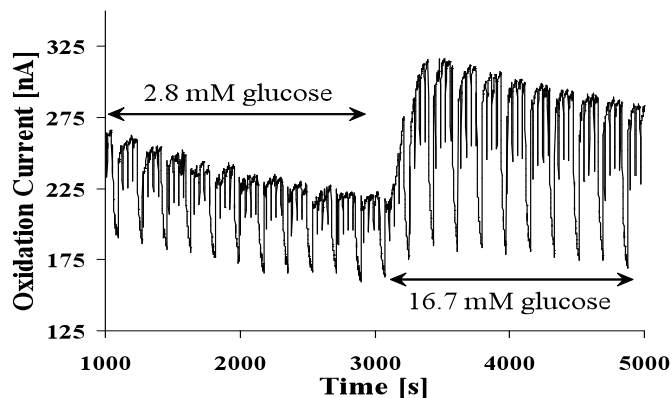


Figure 32. Amperometric current response MWCNT/DHP sensor film in MAMP with 75 islets at + 0.88 V vs. Ag/AgCl (2M KCl) showing increase in peak currents upon stimulation of islets with 16.7 mM glucose.

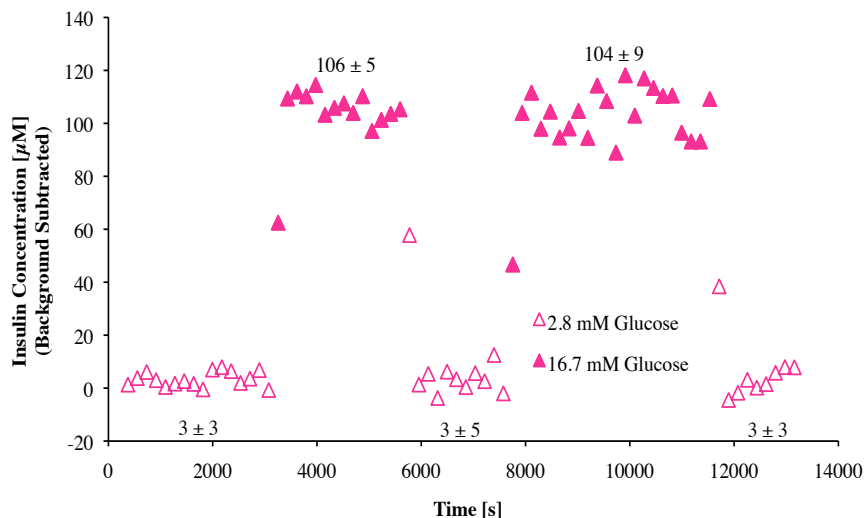


Figure 33. Insulin concentration (background subtracted) as measured with MWCNT/DHP composite film in the MAMP with islets upon stimulation with high glucose

The stop flow peak current in the absence of islets exhibits no significant change ($7.8 \pm 6.3 \%$) when the glucose concentration of the HBSS media is increased from 2.8 mM to 16.7 mM. The background current observed at the MWCNT/DHP composite film electrodes differed, due to variability arising from hand-casting of the films. Due to this variability, and the fact that insulin secretion is extremely low on the micromolar scale during exposure to low glucose,¹⁰⁴ this background current was subtracted. The sensitivity of the MWCNT/DHP film determined in Figure 30 B was used to convert the background subtracted current to concentration.

As shown in Figure 33, when islets are present in the MAMP, the insulin concentration was $3 \pm 3 \mu\text{M}$ during exposure to 2.8 mM glucose. The insulin concentration increases rapidly to $106 \pm 5 \mu\text{M}$ when the glucose concentration is increased to 16.7 mM glucose. When the glucose concentration returns to 2.8 mM, the insulin concentration returns to $3 \pm 5 \mu\text{M}$. A second exposure to 16.7 mM glucose

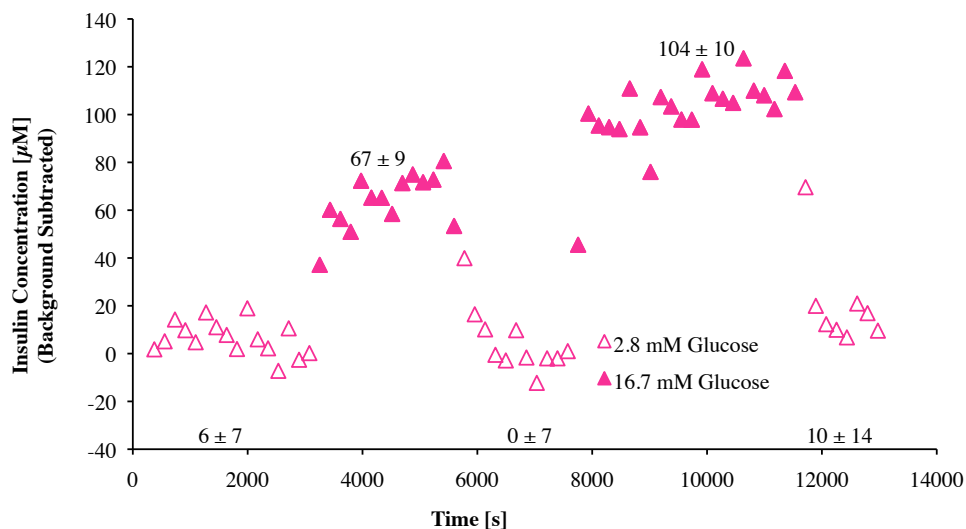


Figure 34. Insulin concentration (background subtracted) as measured with MWCNT/DHP composite film in another chamber of MAMP with islets upon stimulation with high glucose

increases the insulin concentration to $104 \pm 9 \mu\text{M}$, with a decrease to $3 \pm 3 \mu\text{M}$ upon return to 2.8 mM glucose.

The stop flow current response at the MWCNT/DHP sensor for an additional chamber of islets is shown in Figure 34. Again an increase in the insulin concentration is seen upon stimulation with 16.7 mM glucose, from $6 \pm 7 \mu\text{M}$ to $67 \pm 9 \mu\text{M}$. The concentration decreases to $0 \pm 7 \mu\text{M}$ when the glucose concentration is returned to 2.8 mM. A second exposure to 16.7 mM glucose causes the insulin concentration to increase to $104 \pm 10 \mu\text{M}$, with a return to $10 \pm 14 \mu\text{M}$ insulin concentration when the glucose concentration is lowered to 2.8 mM. This larger signal upon a second stimulation with 16.7 mM glucose could be indicative of time dependent potentiation (TDP) that is characteristic of β cells in which the pool of insulin granules available for immediate release is expanded by a prior exposure to glucose.⁸³ For both chambers of FVB murine

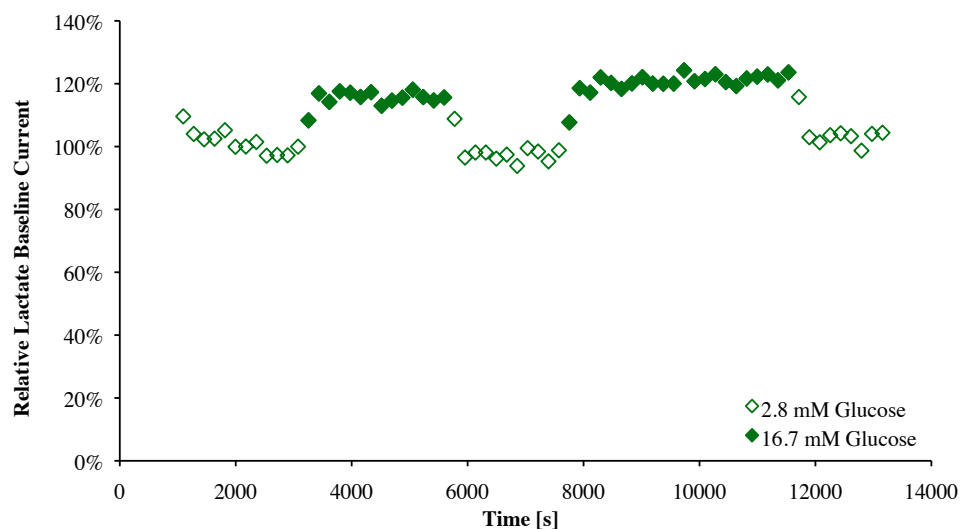


Figure 35. Normalized baseline current response at the lactate oxidase electrode in microfluidic chamber of MAMP upon stimulation of 75 islets with high glucose

islets the increase in the concentration of insulin secreted upon stimulation with glucose is much greater than the concentration increase seen for *ob/ob*- mice in literature, which was measured using perfusion with ELISA quantitation¹⁰⁴ and is greater than the eight-fold increase seen with isolated rat islets.¹³⁹

In the same chamber of islets as Figure 33, increases are seen in the current at the lactate oxidase during flow each time the islets are stimulated with 16.7 mM glucose, as shown in Figure 35. This is significant because it has been shown that up to 90% of the pyruvate produced within β cells is shuttled through the TCA cycle. In the other cell types of the islet (α , δ , and PP cells), only 15% of pyruvate undergoes mitochondrial metabolism. For this reason, the majority of lactate released from the islet is not derived from the β cells but rather from the α , δ , and PP cells.¹⁴⁰ Thus, the increase in current at the lactate electrode during glucose stimulation suggests that we are successfully able to observe the metabolic activity of the entire islet, not just that of β cells.

At +0.88 V vs. Ag/AgCl (2 M KCl), the potential where insulin is detected with the MWCNT/DHP composite film, somatostatin is a possible interferent as it is secreted by the δ -cells of the islet⁹² and has a peak oxidation potential of +0.80 V vs. Ag/AgCl.¹⁴¹ The dramatic increases seen at the MWCNT/DHP composite electrode in Figures 33 and 34 are unlikely to be due to somatostatin as β cells are stimulated to secrete insulin when islets are exposed to high levels of glucose⁸³ and the function of somatostatin is to inhibit β cells.^{142,143}

A major benefit of our MAMP protocol for studying islet metabolism is the confined volume into which insulin is released compared with conventional methods. This setup enhances the detection of insulin and other metabolites as it allows them to accumulate during the stop-flow period. If the MWCNT/DHP composite film insulin sensor was utilized outside of the MAMP stop-flow system, this benefit would be lost and the concentration detected from the same number of islets would be lower. While this concentration is easily measured, if necessary, the stop flow period could be lengthened to allow insulin to accumulate and increase the sensitivity of the technique, enabling the use of a smaller number of islets.

The effect of potassium stimulation on isolated murine islets was also studied using the MWCNT/DHP composite electrode in the MAMP. The background subtracted insulin concentration response of three chambers of islets can be seen in Figure 36A-C. In all three cases, the insulin concentration increases during exposure to 16.7 mM

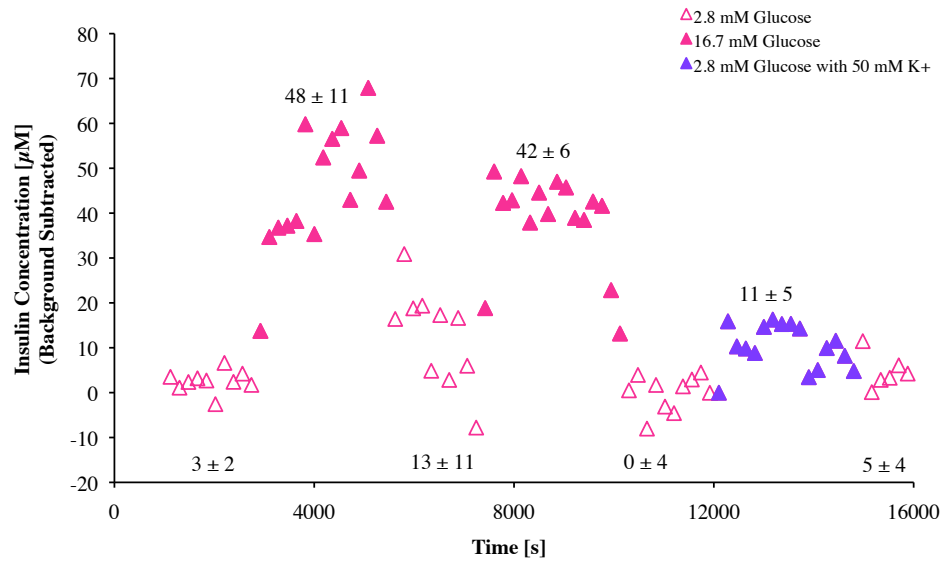


Figure 36A. Insulin concentration (background subtracted) as measured with MWCNT/DHP composite film in the MAMP with 75 islets upon stimulation with high glucose and low glucose with 50 mM potassium

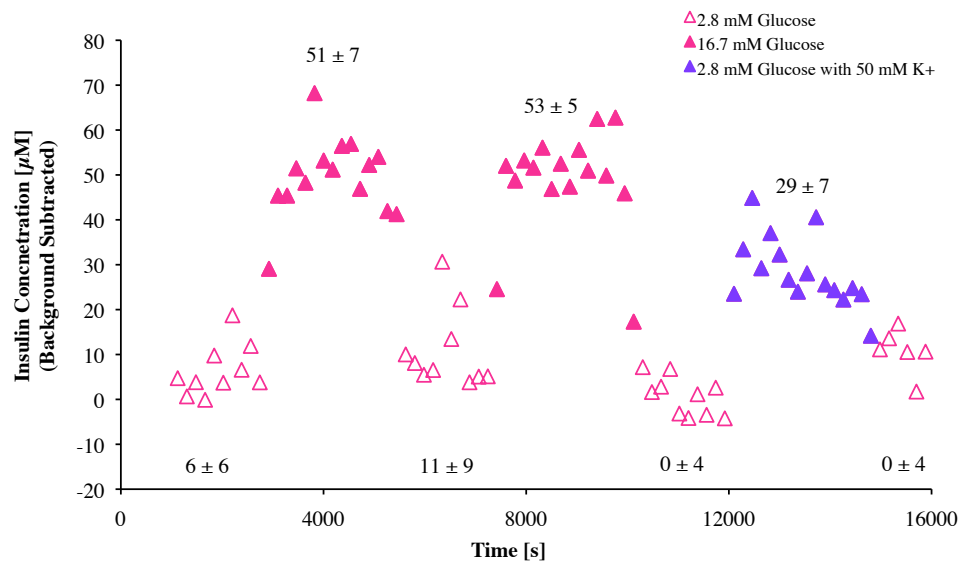


Figure 36B. Insulin concentration (background subtracted) as measured with MWCNT/DHP composite film in the MAMP with 75 islets upon stimulation with high glucose and low glucose with 50 mM potassium

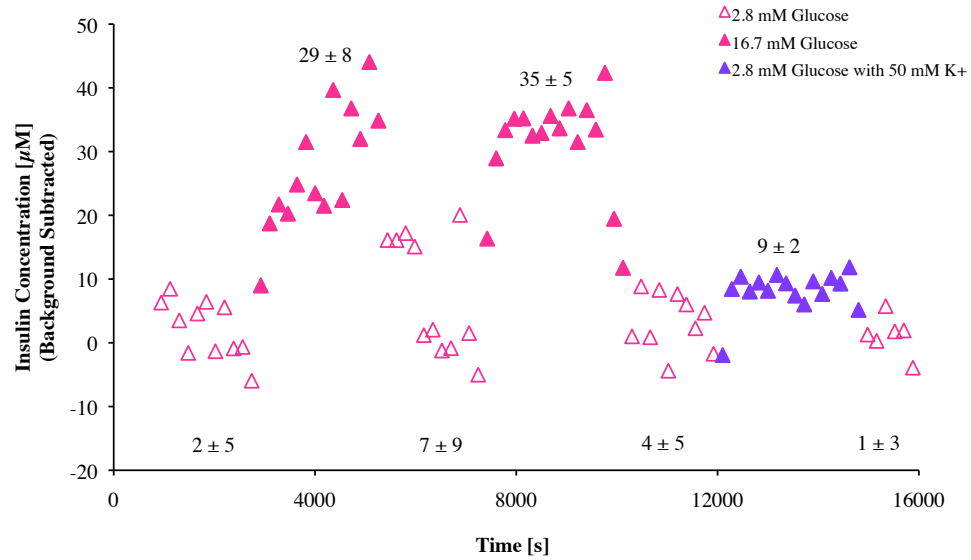


Figure 36C. Insulin concentration (background subtracted) as measured with MWCNT/DHP composite film in the MAMP with 75 islets upon stimulation with high glucose and low glucose with 50 mM potassium

glucose with a smaller, reversible increase seen upon exposure with HBSS containing 2.8 mM glucose and 50 mM K⁺. This smaller, yet significant increase, agrees with insulin secretion results for isolated rat islets measured *via* radioimmunoassay.¹³⁹

These islet studies demonstrate the detection of insulin secreted by islets with our newly developed MWCNT/DHP composite sensor in the MAMP as a real-time method for characterizing islet function and physiology in microfluidic devices. The previous studies of rat islets mentioned for glucose stimulated insulin secretion and potassium stimulated secretion, as well as the study of the role of pyruvate in β cells, was not real-time methods but rather standard static methodology that required subsequent analysis of insulin content by radioimmunoassay.¹³⁹ Bergsten's study of isolated islets from ob/ob-mice was performed using a perfusion method with *ex situ* analysis of insulin *via* ELISA.¹⁰⁴ The addition of insulin sensing capabilities to the MAMP have a clear advantage for studying islet physiology as the metabolic activity of the islet as a whole

can be studied in addition to insulin secretion. The MWCNT/DHP composite sensor has been used in the MAMP for studies of islet physiology under continuous flow to study oscillations in insulin secretions.⁷³ The sensor has also been adapted for use with a carbon fiber ultramicroelectrode to enable measurements of insulin secretion from single islets.¹⁴⁴

Conclusions

Combined with our successful detection of glucose stimulated insulin secretion and the increased islet metabolism that corresponds with that, these results of potassium stimulated insulin secretion show that the addition of the MWCNT/DHP sensor into the MAMP has enabled real-time study of islet metabolism, including insulin secretion and lactate production. We have successfully developed a MWCNT/DHP composite film electrode for the electrochemical detection of insulin secreted by islets in a microfluidic system. This sensor enables direct label-free detection of insulin with improved electrocatalytic kinetics, facile preparation, and resistance to fluidic shear forces as compared to other insulin sensors. We were able to detect insulin concentrations as low as 1 μM in the MAMP during calibration experiments. This sensor was integrated into the multianalyte microphysiometer, and insulin secretion by islets was detected. The increase in concentration of insulin detected for 75 islets is much higher than the limit of detection and as high as 100 μM for the sensor because of the confined volume of the microfluidic chamber and the buildup of insulin molecules during a stop flow period. Additionally, increased insulin secretion in response to potassium stimulation was also observed. The MWCNT/DHP composite sensor will be used in the MAMP to study islet

physiology in a constant flow method to attempt to observe the oscillations in insulin secretion typical of islets. This MWCNT/DHP composite sensor will be also used with a carbon fiber ultramicroelectrode to study insulin secretion from single islets *via* scanning electrochemical microscopy.

Acknowledgements

I would like to thank Amy E. Rue for her assistance in the development of the MWCNT/DHP composite film and testing of the film in the MAMP and Dr. Madalina Ciobanu for her invaluable help in performing the glucose stimulation and potassium stimulation tests of islets in the MAMP. I thank Dr. William Hofmeister, formerly of the Vanderbilt Department of Chemical Engineering and currently at the University of Tennessee Space Institute for the multiwall carbon nanotube samples. I also thank Dr. Alvin Powers and Dr. Zhongyi Chen of the Vanderbilt Diabetes Research and Training Center for their guidance and for their aid in isolating islets.

CHAPTER V

MAMP FOR THE STUDY OF THE METABOLIC EFFECTS OF CHOLERA TOXIN

Introduction

Cholera is a potentially life-threatening infectious secretory diarrhea caused by cholera toxin (CTx) that is secreted by the gram negative bacterium *Vibrio cholera*.^{145,146} The seventh cholera pandemic that still continues today began in the 1960s when the El Tor strain of cholera emerged as the most prevalent form of the disease.¹⁴⁵⁻¹⁴⁷ This strain entered the Western hemisphere in 1991 in Peru and has since caused more than a million cases in Central and South America.¹⁴⁶ The only animal reservoirs of *V. cholerae* are shellfish and plankton, and infection can be caused by drinking contaminated water or food.^{145,146} Those vibrios that survive passage through the stomach can adhere to the mucosal surface of microvilli of the small intestine where they secrete cholera toxin^{145,146} as well as other toxins.¹⁴⁷ The concentration of vibrios on the mucosal surface rapidly increases to 10^7 to 10^8 cells per gram of tissue.

After an incubation period that can vary from 6 hours to five days, the onset of symptoms is abrupt and is characterized by severe diarrhea that can reach a rate of 1 L/hr. This fluid contains large amounts of sodium, chloride, bicarbonate, and potassium, as well as mucus; the loss of these electrolytes cause blood volume depletion, low blood pressure, and shock.^{145,146,148} The fluid loss can be so great that without proper rehydration, death can result within hours of onset.¹⁴⁵

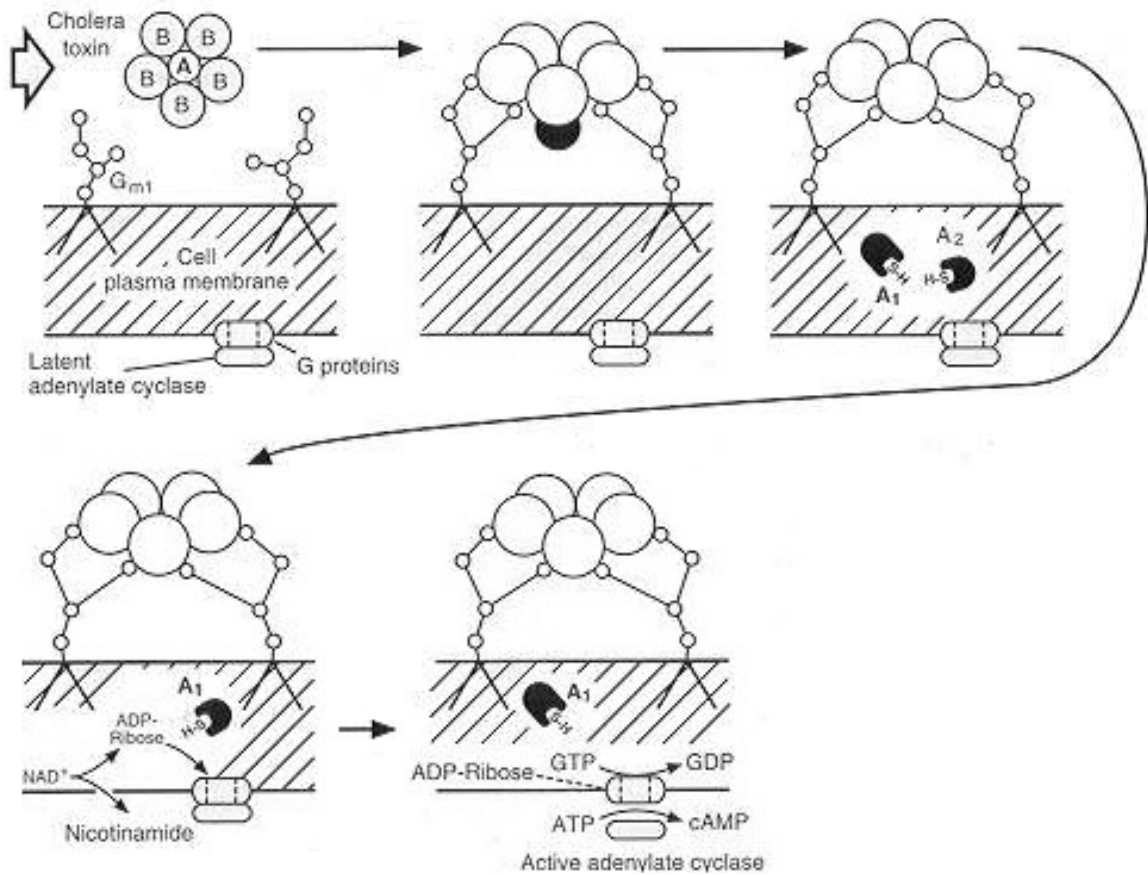


Figure 37. Mechanism of action of cholera toxin. [Adapted from Finkelstein]¹⁴⁶

These clinical effects arise from the action of cholera toxin on both the epithelial and nervous cells of the intestine. The mechanism of action of cholera toxin is illustrated in Figure 37. Cholera toxin, 84 kDa AB₅ hexameric protein, approaches the target cell where B subunits bind to GM1 ganglioside. Upon a conformational change, the A subunit is presented and enters the cell. The disulfide bond of the A unit is cleaved by glutathione, leaving A1 and A2. The A1 unit then catalyzes the formation of ADP-ribose from NAD⁺. ADP-ribosylation of G protein G_sα blocks GTP from inactivating adenylyate cyclase.¹⁴⁶ This causes excessive production of cAMP, which triggers an increase in

chloride secretion by epithelial cells¹⁴⁵ and also triggers changes in secretion by the enteric nerves of the intestine.¹⁴⁸

Cholera toxin is a particularly interesting subject for study in the MAMP, as the clinical effect is well described¹⁴⁵⁻¹⁴⁸ as is the mechanism of adenylate cyclase activation,^{149,150} but there is less information known about the acute and dynamic metabolic effects that occur as a result of exposure to cholera toxin.

As it has been suggested that the diarrheal response to cholera toxin has a significant neurological component (up to 50%),¹⁴⁹ neuronal cells are a logical choice for use in the MAMP. Additionally, PC-12 pheochromacytoma cells (ATCC # CRL-1721) have been shown to be a useful model for studies of neuronal cells¹⁵¹ and to possess GM1 ganglioside receptors capable of binding cholera toxin.¹⁵²

In this chapter, we present the metabolic response of PC-12 cells to cholera toxin. In order to explore which metabolic pathways were affected to cause the response observed, we varied the concentration, duration, and number of exposures of cholera toxin. Additionally, the metabolic response of PC-12 cells to forskolin was measured, as forskolin is known to reversibly activate adenylate cyclase and cause elevated cAMP in PC-12 cells.¹⁵³ The effect of the cAMP-dependent protein kinase inhibitor H-89 on the metabolic response to cholera toxin were also studied, as H-89 has been shown to block the effect of forskolin on PC-12 cells.¹⁵³

Experimental

Chemicals and Instrumentation

All materials were used as obtained unless otherwise noted. Cholera toxin from *Vibrio cholerae*, forskolin from *Coleus forskohlii*, H-89 dihydrochloride hydrate, glucose oxidase (GOx, *Aspergillus niger*), bovine serum albumin (BSA, fraction V, 96%), and glutaraldehyde (glutaric dialdehyde, 25 wt % solution in water) were purchased from Sigma. Stabilized lactate oxidase (LOx) was purchased from Applied Enzyme Technology (Pontypool, UK). Sterile glucose solution and (L)-lactic acid were purchased from Fischer Scientific. Lyophilized alamethicin was obtained from A.G. Scientific, Inc. (San Diego, CA). All MAMP consumables including cell inserts, spacers, and membranes were obtained from Molecular Devices Corp. (Sunnyvale, CA). Modified sensor heads for the MAMP and enzyme films were prepared as described in chapter II. Modified RPMI 1640 buffer for use in MAMP was purchased from Mediatech (Manassas, VA).

MAMP experiments with pheochromacytoma cells

Pheochromacytoma cells ($\sim 5 \times 10^5$ per insert, PC-12, CRL-1721 ATCC) were seeded in Corning Costar[®] Transwell[®] collagen coated cell culture inserts (PTFE, 3 μ m pores) and allowed to grow overnight in F12K media supplemented with 15% donor horse serum and 2.5% fetal bovine serum. All MAMP experiments followed the basic procedure described in chapter II. A four channel microphysiometer and Cytosoft[®] program (Molecular Devices) were used to control pump cycles and temperature. The multipotentiostat described in Chapter III was used to measure the current response. A

120 s stop flow cycle was used with 80 s at a flow rate of 100 μL per minute and a stop period of 40 s. In all experiments modified RPMI 1640 media containing 5 mM glucose was used. Cholera toxin is sold by Sigma Aldrich as a lyophilized powder that is reconstituted as a 23.5 μM solution containing 0.05M Tris buffer salts, pH 7.5, 0.2 M NaCl, 0.003 M NaN_3 , and 0.001 M sodium EDTA. For this reason, all experiments with cholera toxin and controls were run with 5 mM glucose modified RPMI 1640 media supplemented to contain the appropriate concentration of these compounds.

In order to determine the basal metabolic rate of PC-12 cells without toxin, cells were allowed to equilibrate for an hour and thirty minutes before treating with 101 μM alamethicin for forty minutes. In toxin experiments, the cells were again allowed to equilibrate for a period to determine their rate prior to exposure. The cells were treated with toxin for a period of time, and then returned to the running media to allow a period of recovery prior to treatment with alamethicin. In all experiments the sensors were calibrated with modified RMPI media with no glucose and no lactate, with 0.05 mM lactate and 1 mM glucose, with 0.1 mM lactate and 3 mM glucose, with 0.2 mM lactate and 5 mM glucose, and in some cases with 0.3 mM lactate before being returned to the running media. Data was analyzed as described in chapter II.

Results and Discussion

The basal metabolic rates for three chambers of PC-12 pheochromacytoma cells from the same passage and cell seeding are given in Table 3. While there was found to be variability in the basal metabolic rates between passages and seedings, within a given seeding the rates were very similar.

Table 3. Basal metabolic rates of PC-12 cells

Average Metabolic Rates	
Glucose Consumption $\times 10^{-17}$	28.3 ± 2.2
Lactate Production $\times 10^{-17}$	14.4 ± 2.6
Oxygen Consumption $\times 10^{-17}$	2.4 ± 0.7

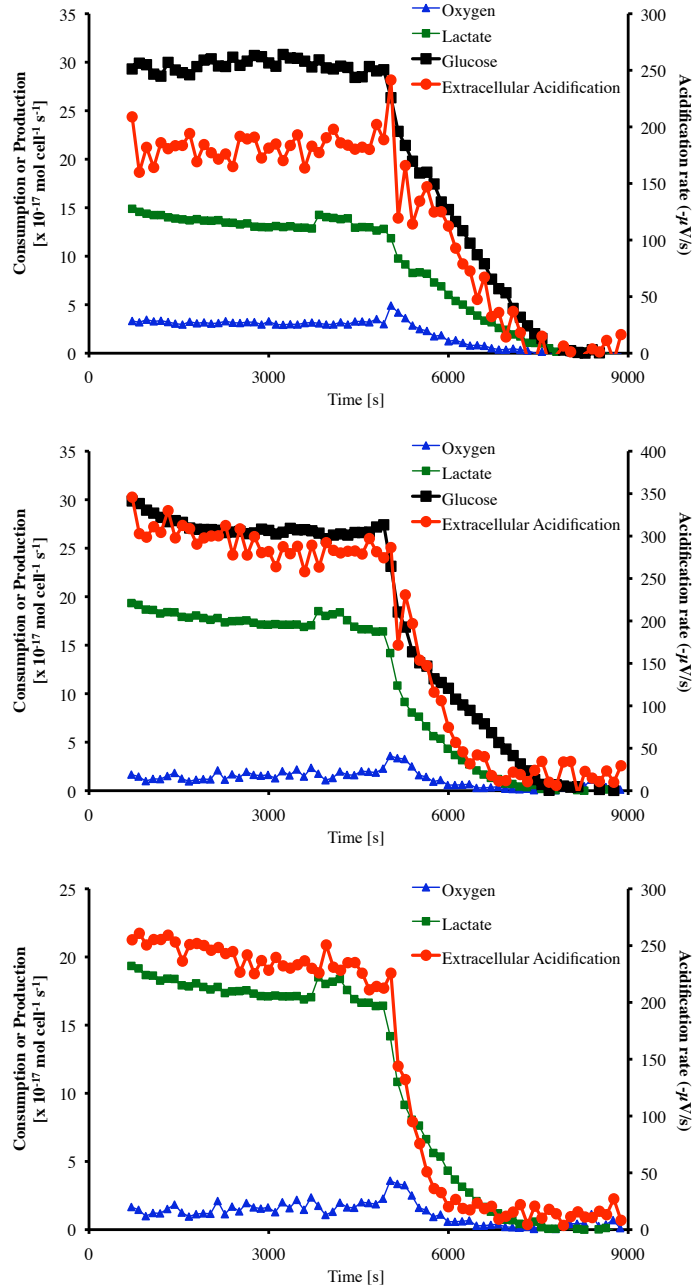


Figure 38. The basal metabolic rates of three chambers of 5×10^5 PC-12 cells as measured in the MAMP. There is no glucose signal in the third graph as that sensor did not calibrate properly.

For this reason in all toxin experiments, one chamber of cells was used to determine the basal metabolism of the cells without exposure to cholera toxin. The basal metabolic rates for three chambers of PC-12 cells are shown within Figure 38. When treatment with 101 μM alamethicin begins at 5040 s, the metabolic rates of all signals rapidly decrease as expected for induced cell necrosis.

The initial experiment performed to determine the metabolic effect of cholera toxin on PC-12 cells involved exposing the cells to 1000 nM cholera toxin for 30 minutes, followed by 90 minutes of recovery before treatment with alamethicin to kill the cells.

When the killed cells were treated 1000 nM cholera toxin, a significant shift was seen in the glucose oxidase electrode signal as shown in Figure 39. The shift in current at the glucose oxidase electrode during flow was quantified as the ratio of the shift to the pre-exposure value. These values for three chambers of cells are given in Table 4; while the magnitude of the shift in the glucose signal was less for dead cells than live cells, the ratio of the shift to the pre-exposure current was the same. Unfortunately, these results indicate that cholera toxin itself is somehow interfering with glucose oxidase. However, even after correcting for this shift, no change was seen in the rate of glucose consumption when cells were treated with cholera toxin, even at the highest concentration and longest exposure time. For this reason, the glucose consumption rate is not shown in the results.

Table 4. Effect of 1000 nM CTx on glucose oxidase sensor in three chambers of cells

A		B		C	
live	pretoxin	live	pretoxin	live	pretoxin
	-63.9		-77.6		-67.3
	shift		shift		shift
	-3.7		-4.7		-3.0
	ratio		ratio		ratio
	0.06		0.06		0.04
dead	pretoxin	dead	pretoxin	dead	pretoxin
	-45.1		-59.5		-49.9
	shift		shift		shift
	-2.9		-3.4		-2.7
	ratio		ratio		ratio
	0.07		0.06		0.05

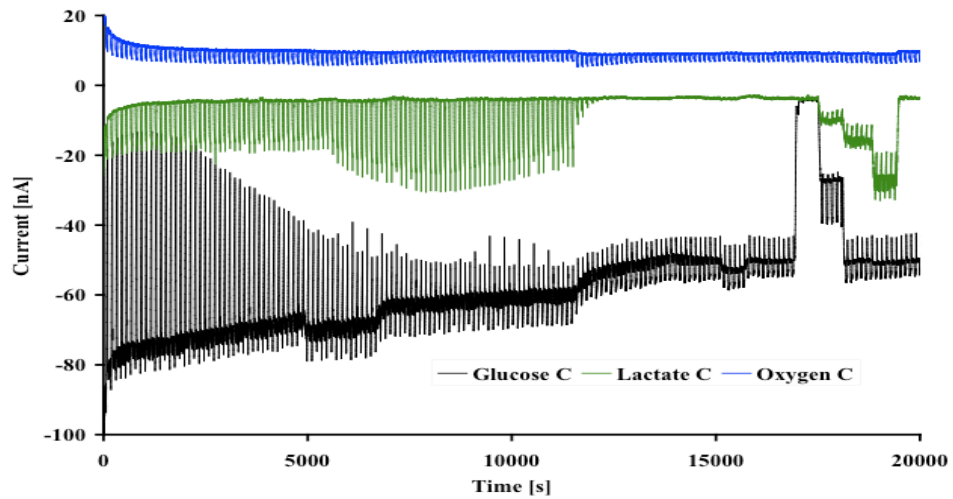
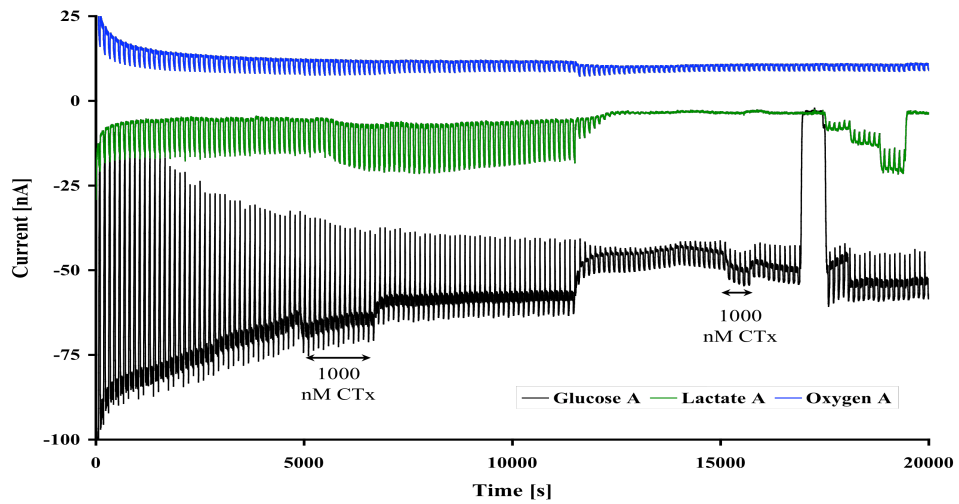


Figure 39. MAMP signals for 5×10^5 PC-12 cells in response to 1000 nM CTx

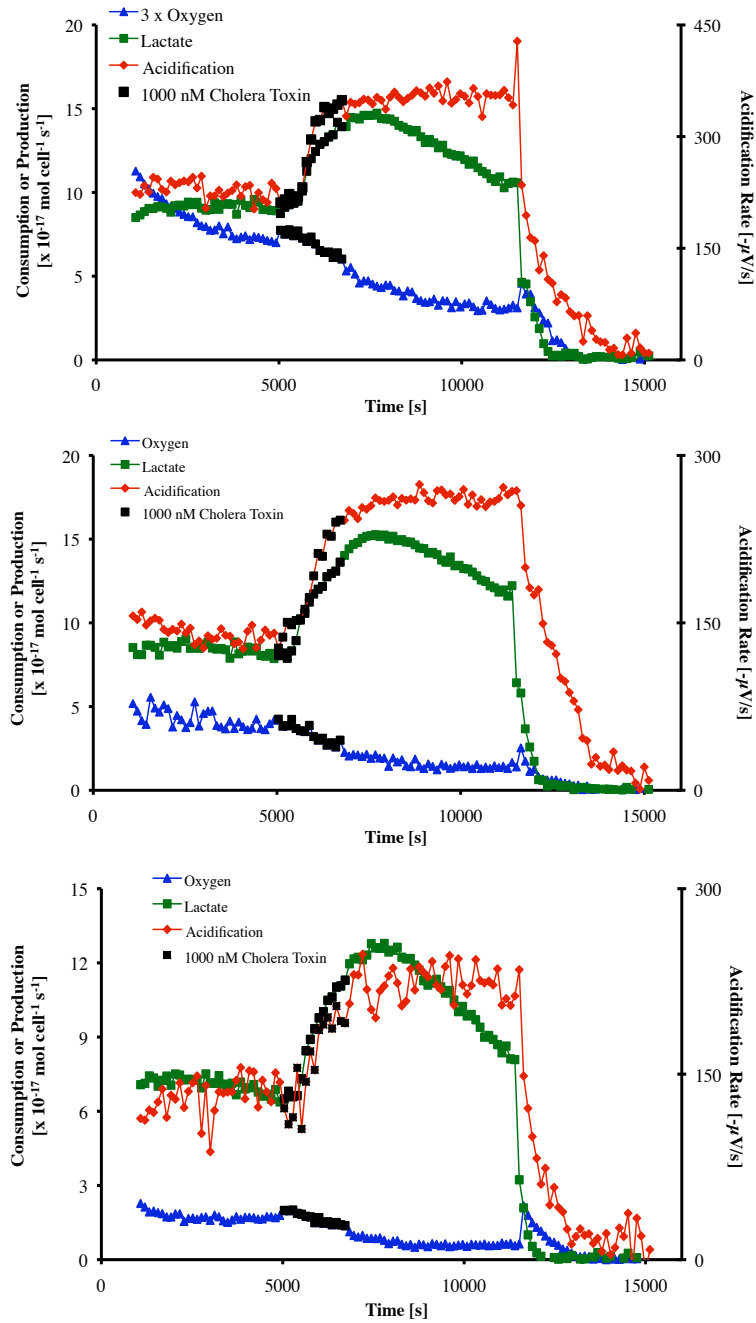


Figure 40. The metabolic rates of three chambers of PC-12 cells exposed to 1000 nM cholera toxin

The metabolic rates of three chambers of 5×10^5 PC-12 cells exposed to 1000 nM cholera toxin are shown in Figure 40. During exposure, the oxygen consumption rate decreases by 40%; when exposed to cholera toxin, the extracellular acidification rate increases rapidly to a plateau of 188% of the pre-exposure rate. After cholera toxin is removed, the extracellular acidification rate remains stable at this value. During exposure after an initial period where the lactate production rate does not change, the lactate production rate increases. This rate continues to increase even after cholera toxin is removed to a peak of 187% of the preexposure rate. After this the lactate production steadily declines, until the cells are killed with alamethicin.

The metabolic rates of two chambers of 5×10^5 PC-12 cells exposed to 500 nM cholera toxin for 30 minutes are given in Figure 41. As in the case of exposure to 1000 nM cholera toxin, the lactate production and extracellular acidification rates increased rapidly, with the extracellular acidification rate plateau at 171% of the preexposure rate and the lactate production rate continuing to increase even after there was no longer cholera toxin present to a peak of 249% of the pre-exposure rate.

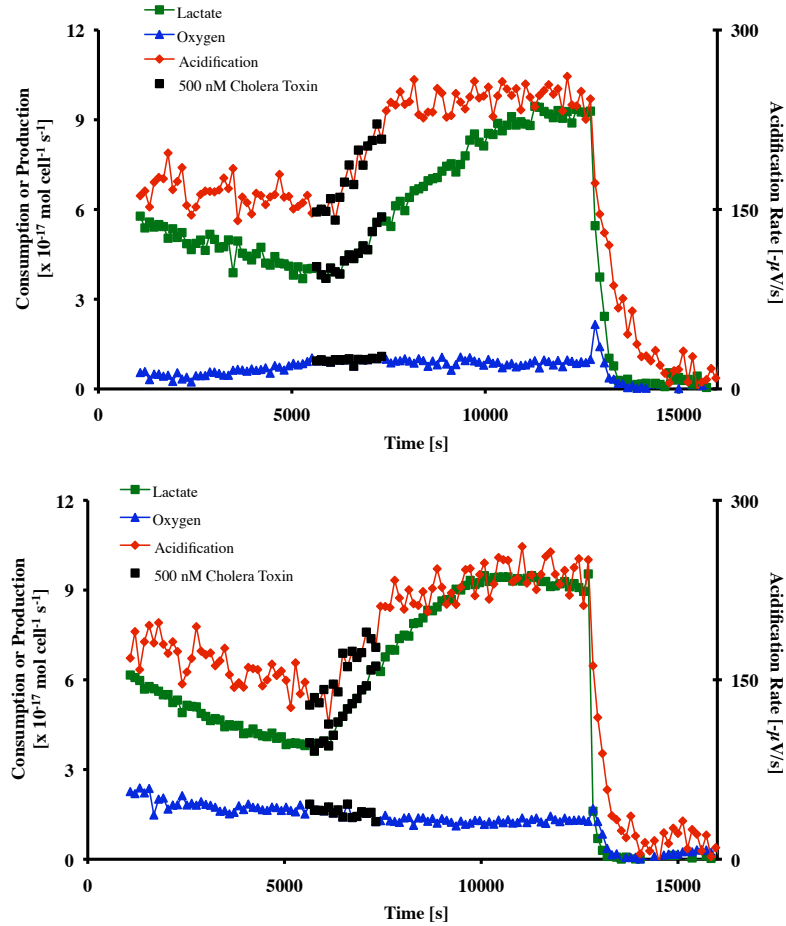


Figure 41. Metabolic response of PC-12 cells to 500 nM CTx

Based on the dramatic metabolic changes seen in PC-12 cell metabolism upon exposure to cholera toxin, the concentration and duration of cholera toxin exposure were studied, as well as the effect of multiple exposures. The metabolic responses of three chambers of PC-12 cells to 3 exposures of 1000 nM cholera toxin, with each exposure being 2 minutes long, *i.e.* a single stop flow period, and followed by a recovery period, is given in Figure 42. The metabolic responses for 3 exposures to 100 nM cholera toxin are given in Figure 43. As in 30 minute exposure, extracellular acidification and lactate

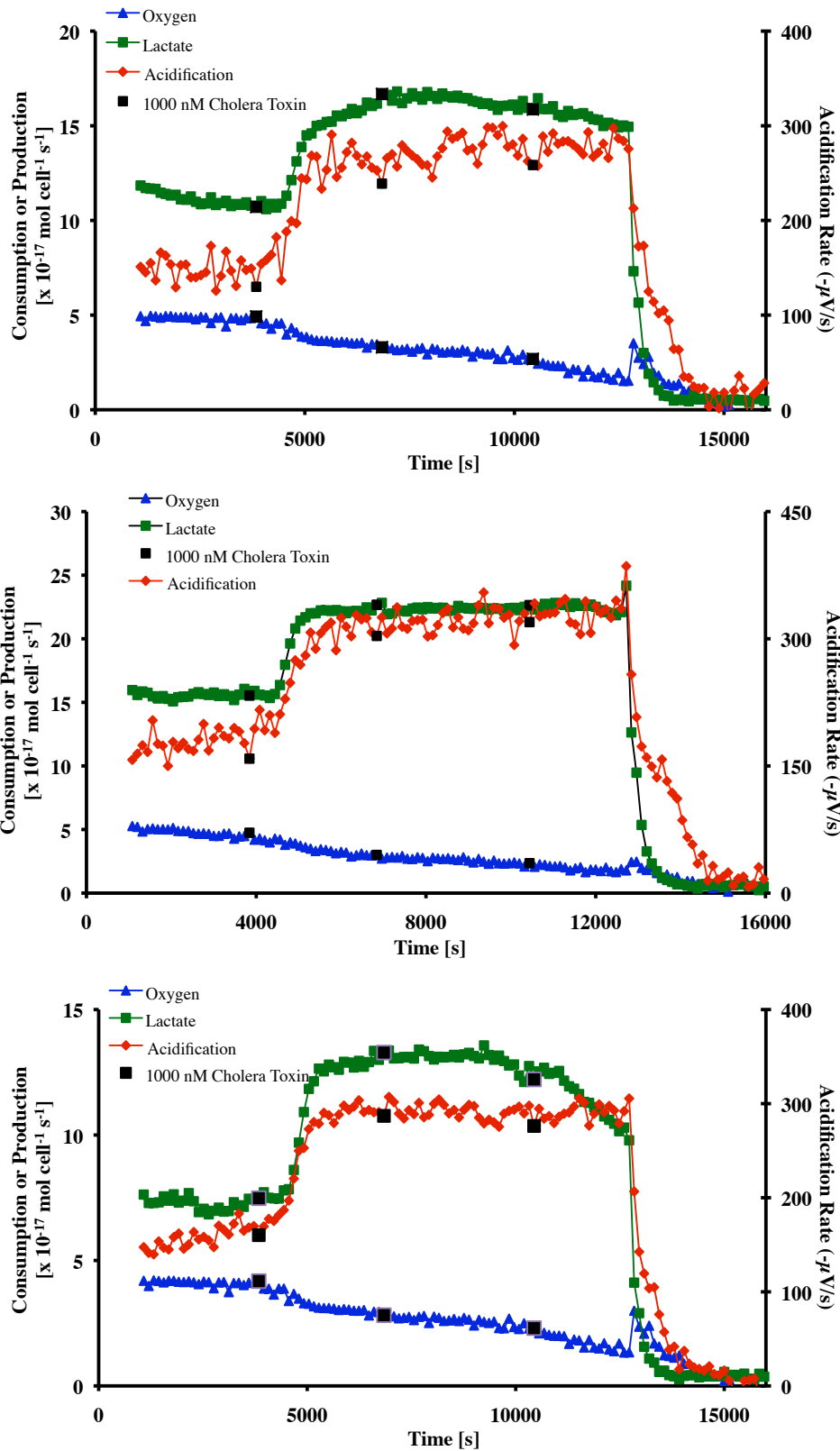


Figure 42. Metabolic responses of three chamber of PC-12 cells to 3 exposures of 1000 nM CTx with each exposure 2 minutes long

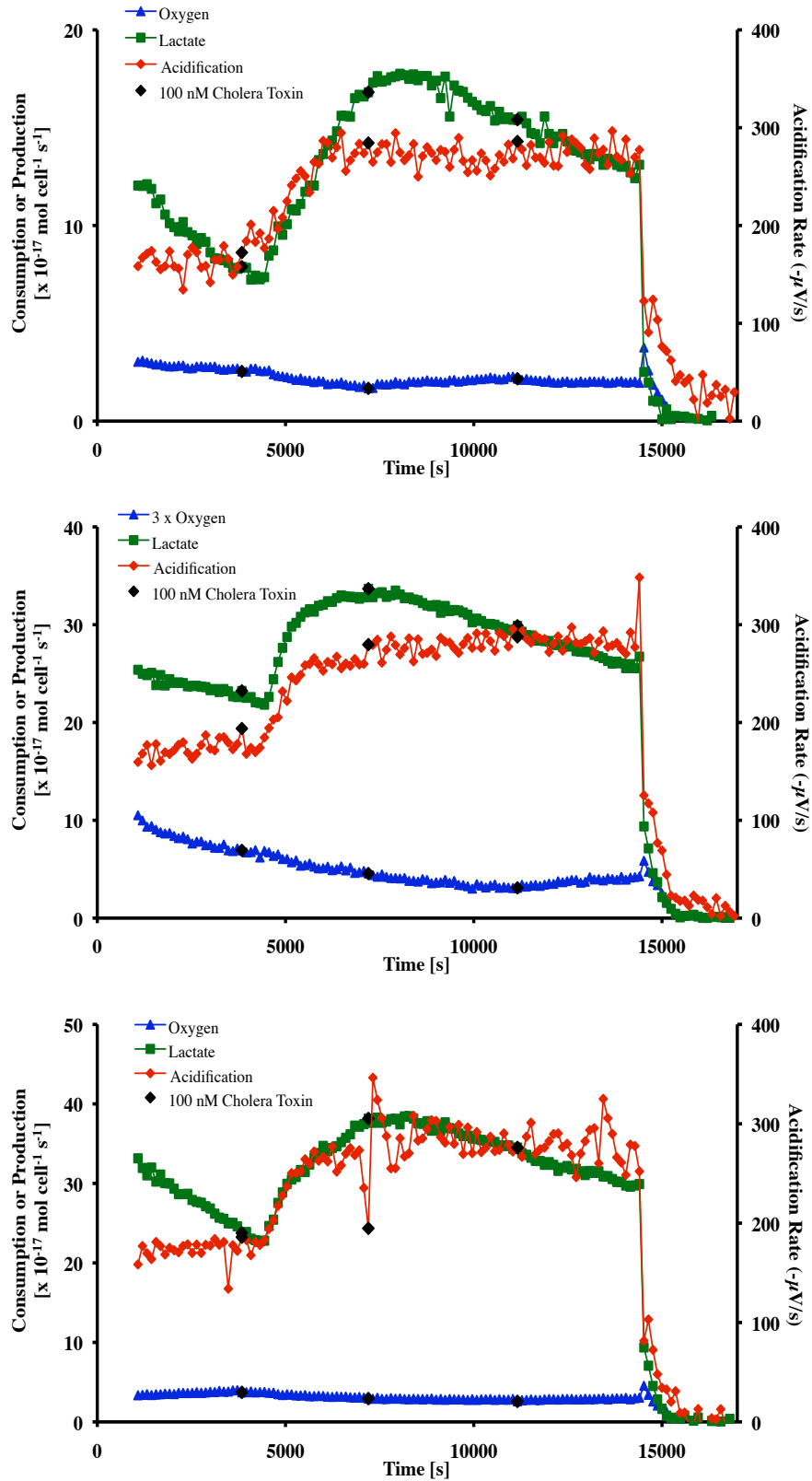


Figure 43. Metabolic responses of three chamber of PC-12 cells to 3 exposures of 100 nM CTx with each exposure 2 minutes long

production rates increase and the oxygen consumption rate decreases. The lactate production rate rises to a plateau in Figure 42 where the cells are exposed to 1000 nM cholera toxin, as was the case for the 30 minute exposure. When cells were exposed to 100 nM cholera toxin for three cycles of 2 minutes each, Figure 43, the lactate production peaks and declines as seen in Figure 41 when the cells were exposed to 500 nM cholera toxin for 30 minutes.

However, the metabolic rates do not respond to the second or third exposure; all of the change appears to come from the first two minutes exposure. In order to verify this, PC-12 cells were exposed to 100 nM CTx for a single cycle followed by an almost four hour recovery period. The metabolic responses are shown in Figure 44. The extracellular acidification rate increases to a plateau and oxygen consumption shows a small decrease. An increase to a peak is seen in lactate production, as was the case when cells were exposed to multiple doses of 100 nM CTx. In this case, however the lactate production rate decreases to below the pre-exposure level for all three chambers of cells tested.

The significance of this experiment was that the same metabolic response was seen whether cells are exposed to a single dose of cholera toxin or multiple doses. Also, there was no response to the second or third dose of cholera toxin in the multiple exposure experiment. This agrees with previous studies that showed that the maximal response in terms of cAMP production could be achieved with doses of 100 nM.¹⁵⁴ For this reason our experiments were performed using 100 nM cholera toxin as we wished to see the maximal metabolic effect using the lowest concentration. Based upon these results and the fact that cholera toxin causes irreversible stimulation of adenylate

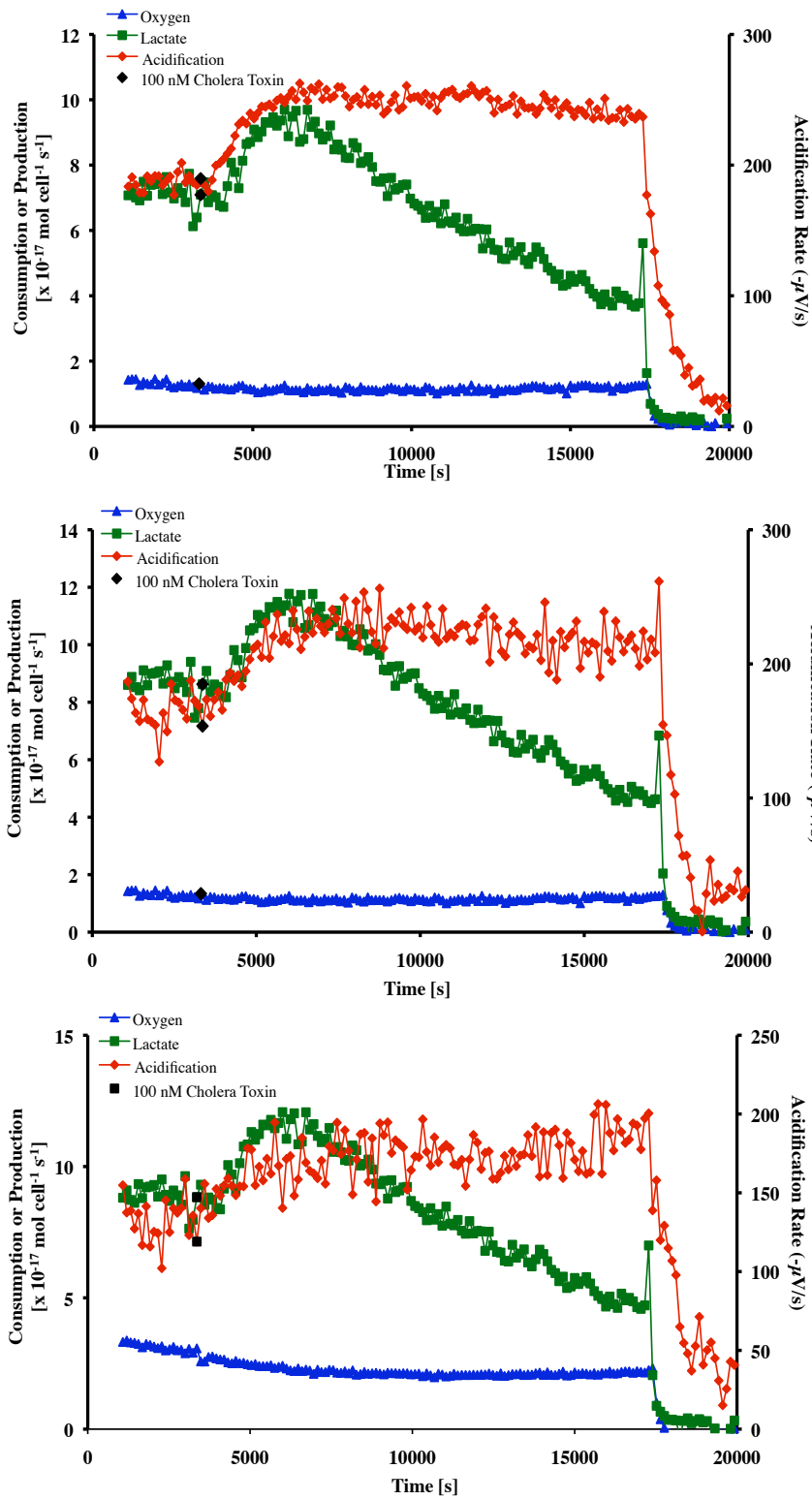


Figure 44. Metabolic responses of three chambers of PC-12 cells exposed to a single 2 minute dose of 100 nM CTx

cyclase,¹⁴⁶ we wanted to explore what cellular pathways are responsible for the increase in extracellular acidification and lactate production and decrease in oxygen consumption. The decrease in oxygen consumption was particularly interesting as a previous study by Keusch on the jejunum isolated from rabbits that had been treated with cholera toxin did not show a statistically significant change in oxygen consumption.¹⁵⁵ Additionally Resnick that the effect of cholera toxin on lactate production varies between multiple cell types, even though the generation of cAMP was similar.¹⁵⁶ In both of these studies, the underlying reasons for these metabolic changes were unclear and were not studied in a real-time manner with simultaneous detection other metabolites. It is also significant to note that in the study by Resnick, the cell lines tested were not related to the intestine or neurons,¹⁵⁶ and the study by Keusch did not attempt to distinguish between the metabolic activity of cholera toxin on the epithelial and neuronal cells of the jejunum.¹⁵⁵

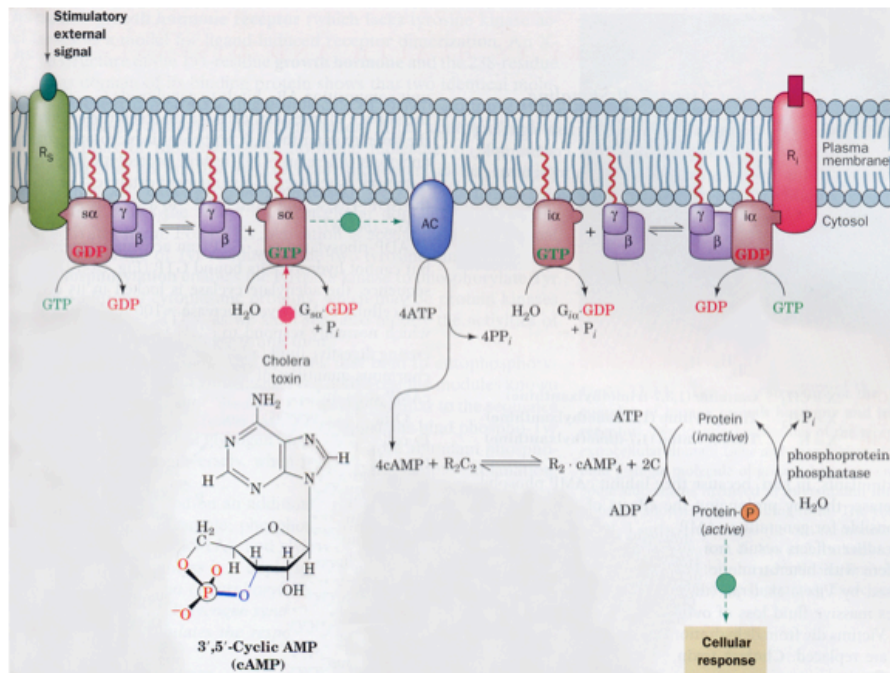


Figure 45. Effect of cholera toxin on adenylate cyclase and effect of cAMP on protein phosphorylation [Adapted from Voet]⁴⁰

Figure 45 illustrates the effect of cholera toxin on adenylate cyclase and the effect of cAMP. cAMP is one of the main secondary messengers in the cell and acts to regulate the phosphorylation of proteins, through the activity of cAMP dependent protein kinase (CAPK), also called protein kinase A (PKA), which is involved in the regulation of glycogen and lipid metabolism.⁴⁰

It is proposed that when PC-12 cells are exposed to cholera toxin, the elevated levels of cAMP cause increased activity of PKA. To investigate this, PC-12 cells were treated with 10 μ M forskolin, which also has been shown to cause elevated cAMP levels in PC-12 cells; the metabolic response to this is shown in Figure 46.

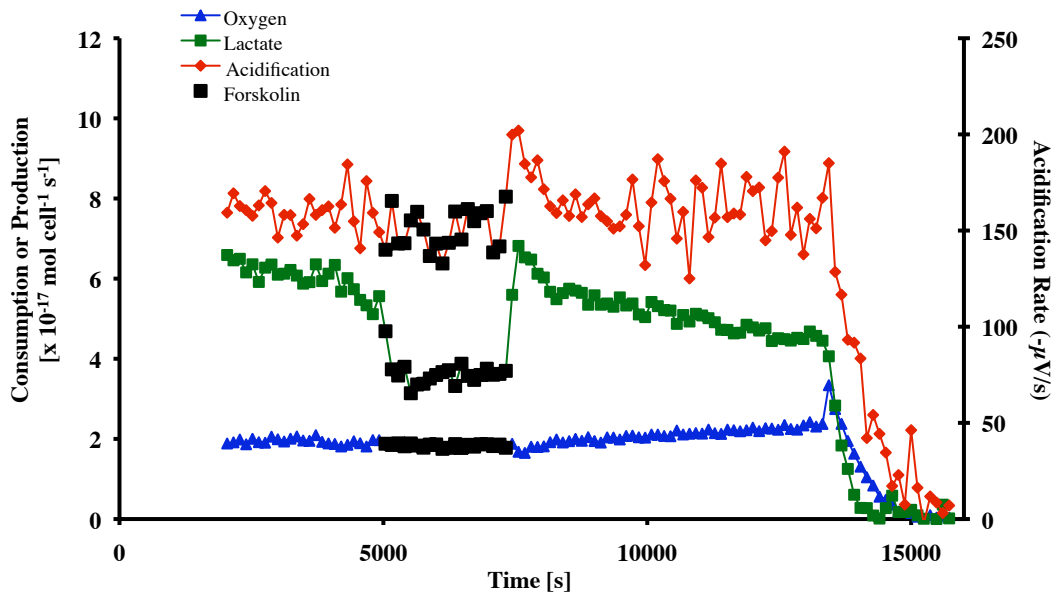


Figure 46A. Metabolic responses of a chambers of PC-12 cells treated with 10 μ M forskolin

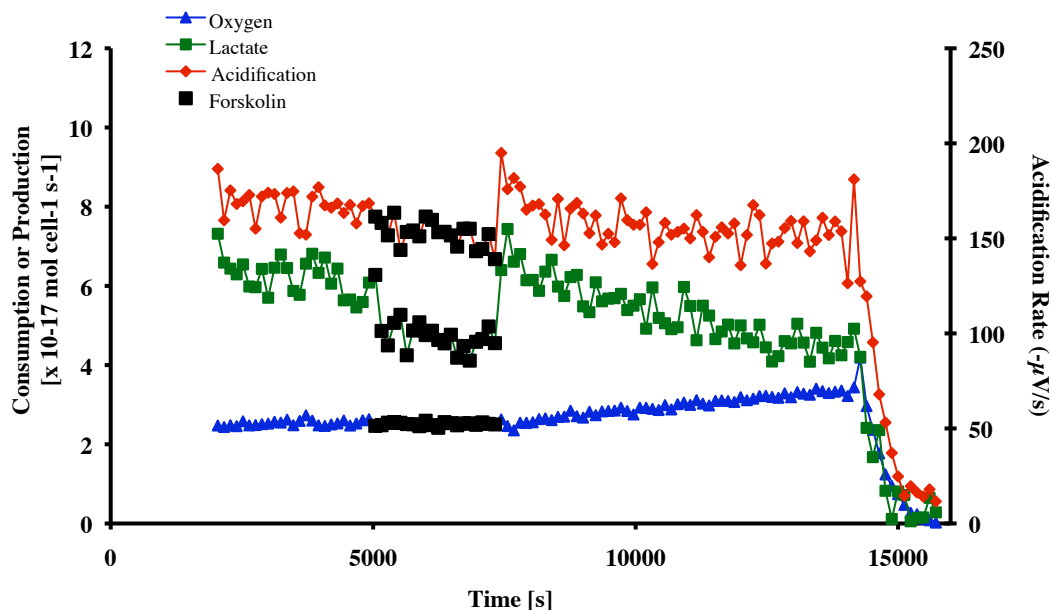


Figure 46B. Metabolic responses of a chambers of PC-12 cells treated with 10 μM forskolin

The response of PC-12 cells to forskolin was quite different than their response to cholera toxin. During exposure to forskolin, there is no change in the extracellular acidification rate of the cells, although when forskolin exposure ends there is a slight increase in acidification that returns to the basal level. Lactate production decreases during exposure to forskolin. After forskolin is removed, the lactate production increases briefly before returning to the basal level. There is no significant change in the consumption of oxygen.

This difference may be explained by the fact that forskolin has secondary activities in addition to its effects on adenylate cyclase. Forskolin has been shown to interact with glucose transporters and ion channels,¹⁵⁷ which would doubtless lead to additional metabolic effects beyond those caused by elevated cAMP.

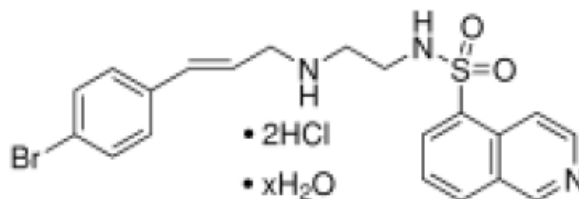


Figure 47. H-89, *N*-[2-(*p*-bromocinnamylamino)ethyl]-5-isioquinolinesulfonamide¹⁵³

The second approach taken to determine whether the activity of PKA was responsible for the metabolic response of PC-12 cells to cholera toxin was to treat cells with a PKA inhibitor. H-89, or *N*-[2-(*p*-bromocinnamylamino)ethyl]-5-isioquinolinesulfonamide shown in Figure 47, was chosen as an inhibitor as it was developed to block effects of forskolin on PC-12 cells by inhibiting the activity of PKA without affecting the intracellular cAMP levels.¹⁵³ H-89 inhibits PKA activity to 2% of the control activity.¹⁵⁸ The metabolic response of PC-12 cells treated with 30 μ M H-89 for 1 hour followed by a single 2 minute exposure to 100 nM cholera toxin is shown in Figure 48. During treatment with H-89, there is a gradual increase in both lactate production and extracellular acidification rates and a dramatic decrease in the oxygen consumption rate. Upon treatment with 100 nM cholera toxin, little effect is seen in the oxygen consumption rate, and the extracellular acidification rate stabilizes. Lactate production shows an increase to a plateau. The time it takes the lactate production rate to increase is lengthened and the magnitude of the increase is less than in cells that are

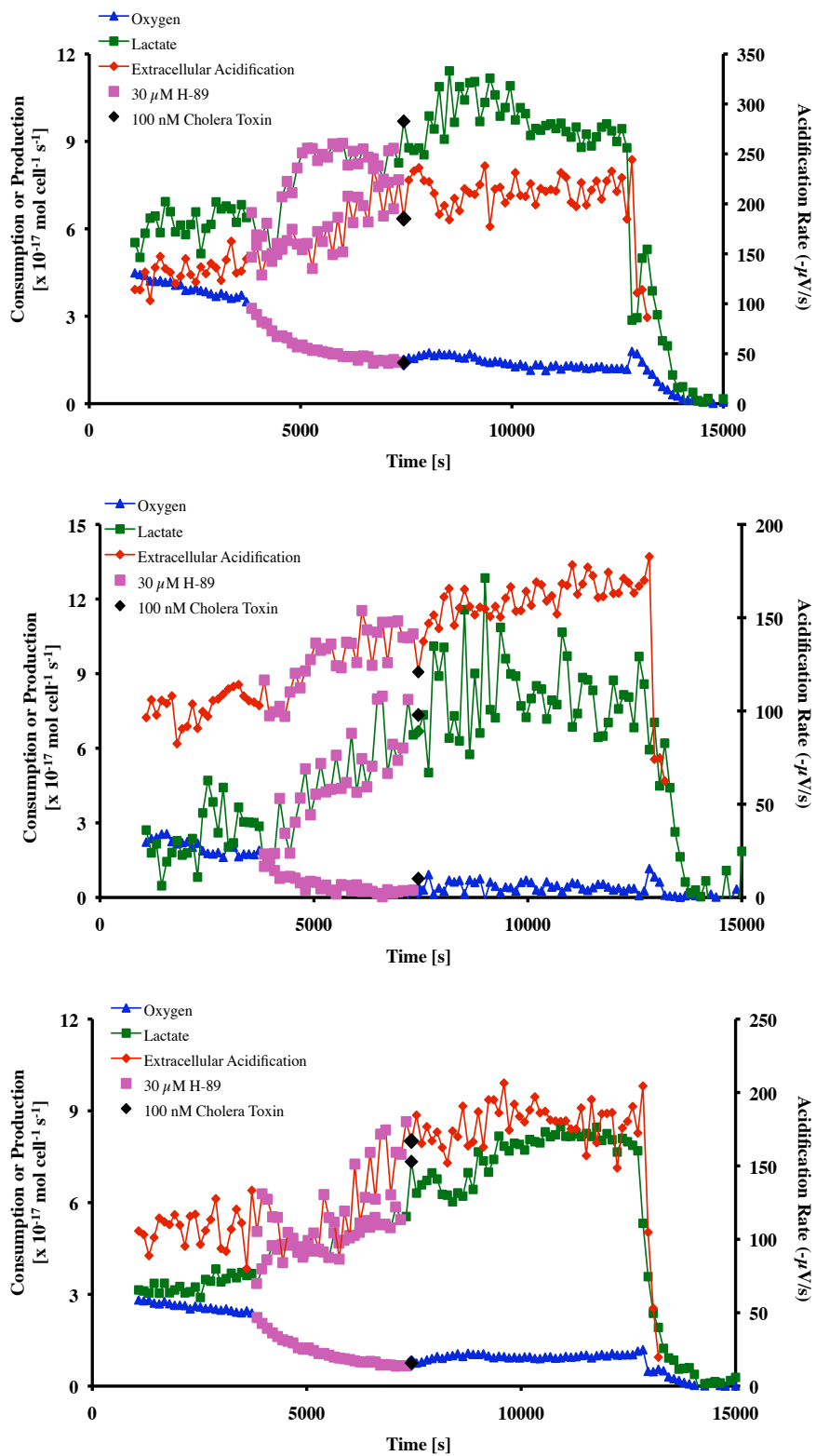


Figure 48. Metabolic responses of three chambers of PC-12 cells treated with 30 μM H-89 and a single two minute dose of 100 nM cholera toxin

not treated with H-89. This result suggests that the increase in lactate production is mediated by PKA. However, H-89 also inhibits a number of additional protein kinases to 25% or less of their normal activity including MAPKAP-K1b, MSK1, PKB α , SGK, S6K1, ROCK-II, AMPK, and CHK1.^{158,159} For this reason, a more specific inhibitor of PKA must be used to prove the link between the metabolic signals seen and increased phosphorylation of glycogen.

Assuming that the glucose consumption rate of the cells remains unchanged, it is our hypothesis that the increased activity of PKA as a result of elevated cAMP levels triggers increased breakdown of intracellular stores of glycogen and increased glucose-6-phosphate (G6P), as shown in Figure 49.⁴⁰ As the G6P level increases, the cell would not need to increase glucose consumption to supply its energy needs. The breakdown of G6P to pyruvate would cause an increase in the ratio of NADH to NAD⁺. NAD⁺ is used in the citric acid cycle and NADH in homolactic fermentation.⁴⁰ The higher concentration

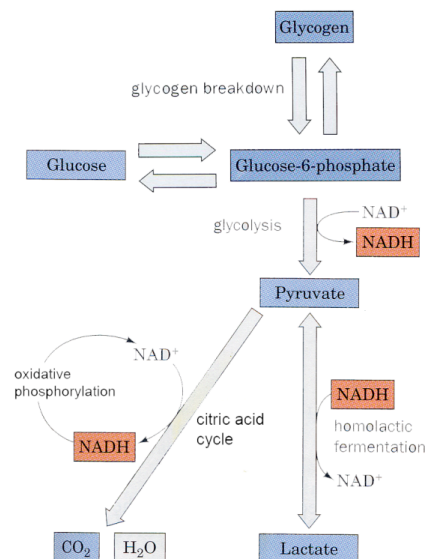


Figure 49. The role of glycogen breakdown in cellular metabolism [Adapted from Voet]⁴⁰

of NADH would result in shunting of more pyruvate into lactic acid production, which would in turn increase the extracellular lactate production and acidification rates. Additional ways to explore this hypothesis are through culturing in isotopically labeled media to label the glycogen stores within the cell or to culture the cells under glucose starvation conditions to decrease the amount of glycogen stored within the cell.

Future work includes the study of lower concentrations of cholera toxin to develop a dose response curve. Other studies in our lab of the effect of lower concentrations of cholera toxin on fibroblasts have show that although the time period until onset varies with concentration the magnitude of the metabolic response was the same.

Conclusions

Multianalyte microphysiometry was successfully used to determine the metabolic response of PC-12 cells to cholera toxin, which elevates cAMP levels. Extracellular acidification and lactate production rates increased, and oxygen consumption rates decreased, when cells were treated with cholera toxin. While forskolin is also known to cause increased cAMP, the metabolic response of PC-12 cells to forskolin did not mirror the response to cholera toxin. When cells were treated with the PKA inhibitor H-89, there was a distinct response of the cells to H-89 itself and the response of PC-12 cells to 100 nM cholera toxin was diminished. These experiments show that the MAMP is a useful tool for determining the acute metabolic effects of biological toxins in real-time and for exploring the signaling pathways triggered by exposure to a toxin or other agent.

Future work in the study of the metabolic effects of cholera toxin using the MAMP will be center on the use of Caco-2 human colon cell line (ATCC # HTB-37) to determine whether there is a differential metabolic response to cholera toxin between the colon cells and the enteric nerve cells that have been implicated in up to 50% of the clinical effects of cholera.¹⁴⁹

Acknowledgments

I would like to thank Dr. Evgeni Kozlov for his guidance in cell culture and Jennifer Merritt for invaluable discussions and support.

APPENDIX A

DESIGN AND ASSEMBLY OF MULTIPOTENTIOSTAT MODULES FOR MULTIANALYTE MICROPHYSIOMETRY

WRITTEN BY EDUARDO LIMA WITH RON REISERER

Due to the large number of quantities to be measured amperometrically in the multianalyte microphysiometer, the design of a custom potentiostat was crucial to keep the costs of our system low. Each chamber of the MAMP has three working electrodes and one counter electrode that need to be controlled by a bi- or multi-potentiostat. Because each MAMP instrument has four chambers, four multipotentiostats are required per MAMP. Since our goal is to run several units in parallel, it becomes clear that the use of commercial potentiostats is not a viable approach. Instead, we opted to build a modular potentiostat in which each module or channel would measure analytes (except pH) in one chamber of the MAMP. Thus, a four-channel potentiostat connects to a single MAMP, whereas an eight-channel potentiostat can measure changes in analyte concentrations on two instruments simultaneously.

Our modular design is quite flexible and allows for easy modifications to expand the current capabilities or for use in other applications. The potentiostat is comprised of a passive backplane, a chassis, a regulated DC power supply, a configuration card, and up to eight bi-potentiostat modules or channels.

The backplane, which is shown in Figure 50, consists of a 6-layer printed circuit board (PCB) board with connectors on both sides. Its main purpose is to provide connections between the modules and the configuration card, as well as to deliver power

to the modules. On the front side, eight Z-pack 2mm HM, type A (AMP 188834-1) male connectors accommodate the mating connector of each of the modules. On the back side, two Z-pack 2mm HM, type B (AMP 100669-1) male connectors accommodate the two mating connectors of the configuration card. The Z-Pack 2mm HM family of connectors, also used in the compact PCI standard, combines high performance, high density and robust mechanical features, as well as allows for shielding. Because of the high pin density, multi-layer boards are required in order to route all of the signals.

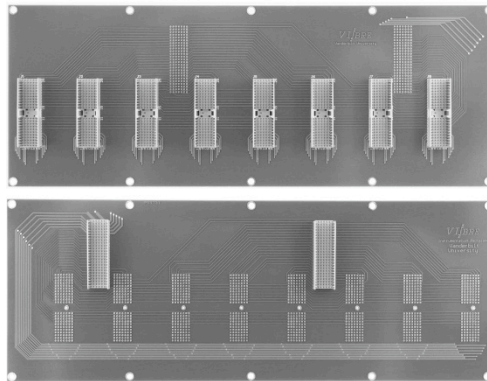


Figure 50. Backplane of multipotentiostat module

The backplane implements 12 parallel power/high-current lines, 12 parallel signal lines and 8 individually addressable lines per slot. The two central layers of the PCB are ground planes intended to be connected to earth ground and power ground (common), whereas the other two inner layers and the two outer layers are dedicated to signal routing. Eight holes in the PCB allow for fixing the backplane to the subrack, as discussed below. One of these holes is coupled to the earth ground plane, and is usually connected to the earth ground pin of the power line EMI filter in the power supply module. The central row of each of the 10 connectors is connected to power ground, providing a low impedance path for return currents.

As for the chassis, the potentiostat is housed in a 3U 19-inch subrack (CMA14-16/90, Vector Electronics & Technology), which accepts ten 1.65"-wide card cages. We used either four or eight of these cages (EFP164A66) to encase the multipotentiostat modules, and a wider (3.05"-wide) card cage (EFP304A66) to encase the power supply. The front plate of the wide cages had to be remade so as to fill the space of two 1.65"-wide card cages. The subrack was then mounted in a 19-inch tabletop rack (RCBS1900513BK1, Hammond Manufacturing).

We used open-frame dual-output regulated linear power supplies (HBB15-1.5-A+, Condor), capable of delivering +12V and -12V at 1.7A. The power supplies were partly disassembled and the aluminum frame was cut prior to mounting to the card cage. The outputs of the power supply and the earth ground are provided to the configuration card by a cable with a 4-pin keyed terminal housing at the end. A combination rocker/thermal circuit breaker switch (1410-F110-P1F1-W14QE3-1A, E-T-A) placed at the front panel of the cage turns on and off the power supply, and thus, the potentiostat.

Figure 51 shows a picture of the configuration card. It is comprised of a 4-layer PCB, in which two Z-pack 2mm HM, type B (AMP 106774-1) female connectors and two Amplimite .050 Series II cap header (AMP 2-174339-5) connectors are mounted on. The latter provide direct connection between the configuration card and the DAQ card *via* one (four-module systems) or two (eight-module systems) standard National Instruments 68-pin shielded cables, avoiding the need for breakout boxes and clumsy cable arrangements. The two inner layers of the PCB consist of ground and power planes, whereas the two outer layers are dedicated to signal routing. The cable from the power supply connects to a right-angle lock header also mounted on the board.

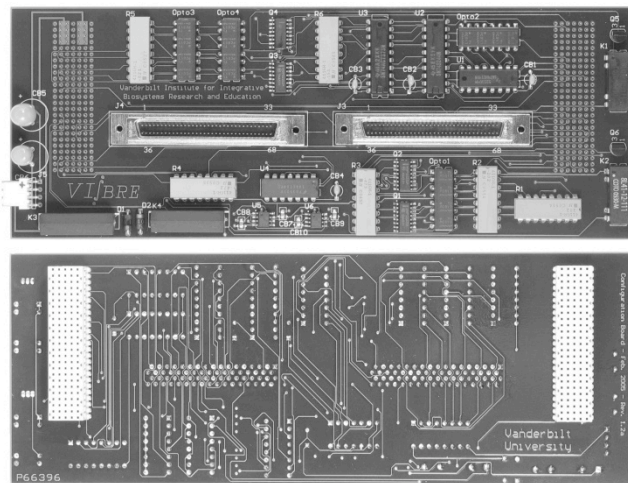


Figure 51. Configuration card

The function of the configuration card is to: (i) distribute power to the backplane; (ii) route backplane signal lines to the DAQ card and pertinent signal lines of the DAQ card to the backplane; (iii) optically isolate digital signals going to and coming from the DAQ card; (iv) decouple the potentiostat analog ground from the DAQ card analog ground; (v) implement a power-on sequencing scheme for the modules; (vi) implement a six-bit data bus with two additional control bits; and (vii) provide control signals to the reed relays that connect/disconnect the electrodes to/from each module. The bus handles the selection of the sensitivity ranges of the potentiostat channels as well as the saturation status and saturation slot number. To keep compatibility with some E-series DAQ cards, we only used 8-bit digital I/O, which lead to the to 6-bit bus concept. The use of a configuration card considerably simplifies adapting or expanding the design to incorporate new features, as it does not require changes in the backplane or —depending on the case— in the module cards. It also allows for different types of modules to be plugged to the backplane and be properly routed to the DAQ card.

Relays K3 and K4 implement the power-on sequencing scheme, in which +12V is available before -12V and 5V, in order to ensure proper operation of CMOS analog switches present in the modules. K4 also disconnects the 5V supply coming from the DAQ board if the dual-output power supply is turned off, thereby completely de-energizing the configuration card.

The tri-state buffer (U2) and the tri-state latch (U3) handle the 6-bit data bus. Because each bit of digital I/O in the DAQ card is individually configurable either as input or output, we assigned bits 6 and 7 as control signals (output always), and bits 0 – 5 as data lines. The direction of the latter is set according to the operation intended to be carried out (read from the bus or write to the bus). Bit 7 determines whether the DAQ card is writing information (low) to the bus or reading data from it (high). It controls the least-significant-bit (LSB) output enable pin of U2 and also the relays K1 and K2, which generate the signals that command the electrode relays in the modules. K1 is normally open, whereas K2 is normally closed, leading to opposite-phase signals. When bit 7 is high, U2 enables its LSB outputs, writing data to the bus, and K1 and K2 are energized, meaning that the electrodes are connected to the multipotentiostat circuits in the modules. These relay control signals are shared by all modules.

By means of individually addressable lines, each module outputs a saturation status signal, which is fed to one of the inputs of the 8-line to 3-line priority encoder (U1). If saturation occurs (*i.e.* if the counter electrode cannot be driven to the voltage required to set the reference electrode at the desired potential and saturates) then U1 outputs —in negative logic notation— the highest number of the saturated modules.

These three lines together with the enable output line, which indicates whether saturation has occurred, are routed to the lower inputs of U2 and are transferred to the data bus whenever the output of the buffer is active. (Note that saturation is different from over ranging, and is independent of the chosen sensitivity ranges.)

When bit 7 is low, U2 is in high-impedance state and there are two possible situations: (i) the bus is idle, or (ii) the DAQ is writing data to the latch U3. For the latter to happen, bit 6, which is only connected to the latch enable pin of U3, must be pulsed high. The data stored in U3 sets the sensitivity ranges in the modules. Although the modules share the same sensitivity settings, each of the three working electrodes has a separate sensitivity control. There are four sensitivity ranges per electrode (1000nA/V, 100nA/V, 10nA/V and 1nA/V), which are selectable *via* a pair of bits, totaling six bits.

Isolation and level translation of digital signals are accomplished by optoisolators and transistors. Signals coming from the 5V-logic DAQ card are converted to 12V CMOS logic by Opto4 and Q3, as well as by Opto3 and Q4. Signals coming from the modules are converted to 5V-logic by Opto1, Q1, Opto2 and Q2.

In order to avoid ground loops in the analog signal path, we used two precision difference amplifiers (U5 and U6). The two inputs of each amplifier are connected to the DAQ board analog ground and to either analog output #0 or analog output #1. The output of the chips is referred to the power supply ground (common), and not to the DAQ card ground. As for the analog inputs, the DAQ card is configured to non-referenced single-ended mode, meaning that the power ground is connected to one of the inputs of an instrumentation amplifier, while the outputs of the potentiostat are connected to the other input through an analog multiplexer, both of them present in the DAQ card. Thus, there is

no direct connection between the power supply ground and the analog ground of the DAQ card.

Each module implements a multipotentiostat with three working electrodes, meaning that two working electrodes have identical potentials referred to the reference electrode. Although our modules were tailored to a specific application, it is straightforward to modify the design so as to implement a tri-potentiostat or another standard configuration, since the core of the circuit is the same. To achieve maximum performance and compactness, almost all components in the modules are surface mount technology.

Figure 52 shows a picture of the module. The op-amp U1 drives the counter electrode, while U2 senses the voltage on the reference electrode, closing the feedback loop. U1 is a high-speed op-amp with the ability to drive capacitive loads (Analog Devices AD817). Because the electrochemical cell is part of U1's feedback loop, oscillations may occur in some experimental setups, despite the op-amp's internal compensation for capacitive loads.

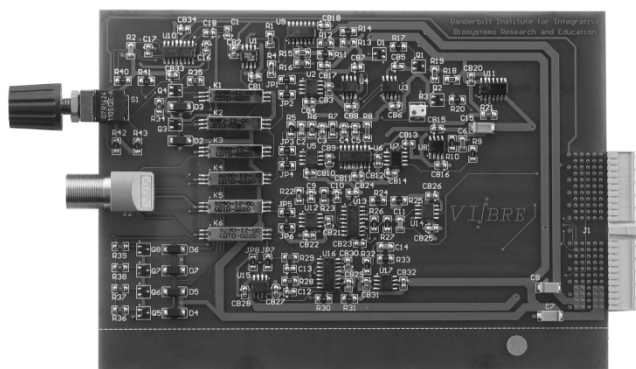


Figure 52. Multipotentiostat module

Therefore, additional external compensation is required to stabilize the potentiostat circuit over a wide range of electrochemical cells.

We used an input-lag compensation scheme (Sergio Franco) with four selectable resistors and a fixed capacitor, which comprises the quad single-pole single-throw CMOS analog switch U10 controlled by a mechanical rotary switch S1, the capacitor C1 and the resistors R2, R44, R45 and R46. The idea is to provide different R-C combinations, which could stabilize various setups. The tradeoff for stabilization is an increase in high-frequency noise, which is filtered out at the current-to-voltage (I-V) converter and at the voltage gain sections. The values for the capacitor and the resistors were obtained empirically, as they were tailored to the modified Cytosensor chambers used in our experiments. Different values may be required to obtain optimal performance for other configurations. The CMOS analog switch ensures signal integrity, which is harder to be obtained by mechanical switches. In this case, a mechanical switch is only used to generate the control signals that select the appropriate compensation pole.

All analog signals pertaining to the electrochemical cell, as well as earth ground, are routed to the 6-pin LEMO connector J2 through single-pole single-throw shielded reed relays K1 - K6, which are controlled by two signals from the configuration card (transistors Q3 - Q8 energize the relays based on these signals). K1 is controlled independently of the other relays, which are all activated by the same control signal. If no measurement is being taken, K1 is energized, while K2 - K6 are open. This physically isolates the electrodes from the circuit, but still closes U1's feedback loop to avoid saturation of the op-amp and eventual damage to electrodes when these are connected to the circuit. When an experiment is in progress, K1 opens and K2-K6 are energized. U5,

U12 and U15 are low-noise precision operational amplifiers that carry out the I-V conversion. Each op-amp has an associated analog switch (U6, U13 and U16, respectively) that selects the gain resistor (*i.e.* the conversion factor) according to the control signals coming from the configuration card. The cutoff frequency of the first-order low-pass filters is set at 7.5 Hz, but can be easily modified by changing the associated capacitors, should larger bandwidths be needed. The output of these op-amps is further amplified and/or filtered by separate gain stages, comprised of U8, U14 and U17. The working electrodes connected to U12 and U15 (glucose and lactate electrodes) are kept at virtual ground, whereas the one connected to U5 (oxygen electrode) is set at $V_{c_2} - V_{c_1}$, where V_{c_1} and V_{c_2} are the input (control) voltages of the potentiostat. The precision difference amplifiers U3 and U4 compute this voltage, which is applied to the positive input of U5. In order to avoid using many large-valued resistors, we opted to utilize a T-network configuration to achieve higher sensitivities. However, because the desired output of U6 is not referenced to ground (U7 yields the corrected output), the T-network can not be used in the I-V converter of the independent working electrode. The inputs of U5, U12 and U15, as well as of U2, are all guarded to minimize signal degradation. Because the current levels involved in the MAMP are quite low, we did not implement an iR compensation scheme.

The voltage at the counter electrode is constantly monitored by a window detector circuit, which is implemented by half the quad comparator U9. Q1 acts as an inverter/level translator, while Q2 controls the charge and discharge of C15, providing a timer mechanism. Should the voltage approach the saturation limits of U1, the output of the window detector switches to low, driving Q2 to cutoff and allowing C15 to charge.

When the voltage across this capacitor reaches the Schmitt trigger U11's low threshold, the output of the latter switches to logic 0 and remains on this state. When U1's output returns to the non-saturation zone, Q2 discharges C15 through R20 and, after a few seconds, the output of U11 goes to logic 1. This signal is monitored by the priority encoder located at the configuration card, which detects a saturation state and identifies in which channel it has occurred. The timer mechanism ensures that the LabVIEW software has enough time to detect the occurrence of saturation in one of the channels.

APPENDIX B

MULTIPLE APPROACHES TO MODELING CURRENT RESPONSES IN THE MAMP TO DERIVE METABOLIC RATES

There are currently three separate efforts underway to develop models to derive metabolic rates from the current responses in the MAMP. The first effort is lead by Narcisse N'Dri, Sebastian Eluvathingal, and Mark Stremmer, formerly of Vanderbilt and now in the Engineering Science and Mechanics department of Virginia Polytechnic Institute and State University. They used their fluid mechanics specialization to develop a 2D axi-symmetric numerical model.¹⁶⁰

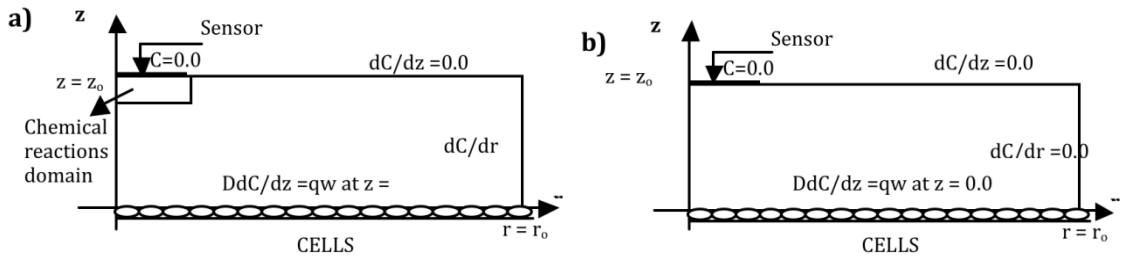


Figure 53. Geometry of the 2D axi-symmetric problem. a) Enzyme sensor and b) Oxygen sensor

Momchil Velkovsky has developed an analytical model for extracting the lactate and glucose fluxes of cells. He has developed formulas for boundary conditions at the surface of the electrodes (Eq. B1) and for the electrode current (Eq. B2) that can be applied to any solution problem containing cell fluxes.¹⁶¹

$$\begin{aligned}
\text{cells: } \partial_n c_S^0|_{\Sigma} &= \frac{R(t)}{D_1}, \quad \partial_n c_H^0|_{\Sigma} = 0, \\
\text{electrode: } \partial_n c_S^0|_{\Sigma} &= \alpha^2 \delta \theta_e c_S^0|_{\Sigma} + (\delta \theta_e + \varepsilon \theta_p) \frac{\partial_t c_S^0|_{\Sigma}}{D_1} \\
c_H^0|_{\Sigma} &= \left(\frac{\delta}{\theta_e} + \frac{\varepsilon}{\theta_p} \right) \partial_n c_S^0|_{\Sigma} + \frac{\alpha^2 \delta^2}{2} c_S^0|_{\Sigma} \\
\text{elsewhere: } \partial_n c_S^0|_{\Sigma} &= 0, \quad \partial_n c_H^0|_{\Sigma} = 0.
\end{aligned} \tag{Eq. B1}$$

$$\frac{I(t)}{nFAD} = \int_{\Sigma} \left(\partial_n c_S^0|_{\Sigma} + \alpha^2 \delta \theta_e c_S^0|_{\Sigma} \right) d^2 \Sigma. \tag{Eq. B2}$$

Jerry Keil has developed a method for derivation of the kinetic rate constants of cellular metabolism by modeling the data as a pseudo Cottrell step. In the MAMP, a linear decrease in the observed current at the lactate oxidase electrode *versus* the inverse square root of time proportional to the bulk concentration of analyte confirms the Cottrell mechanism; *i.e.*

$$i_d = nFAD^{1/2} C^0 / (\pi t)^{1/2} \tag{Eq. B3}$$

Here, n equals the number of equivalents per mole; F , the Faraday constant; A , the working electrode area, in cm^2 ; D , the diffusion coefficient of lactate, in cm^2/s ; C^0 , the bulk concentration, in mol/cm^3 and t , time in seconds. This relationship is modified to reflect the time dependent kinetic factors of consumption or production (Eq. B4-B5).¹⁶²

$$t^{1/2} i_d(t) = (nFAD^{1/2} C^0 / \pi^{1/2}) + (nFAD^{1/2} k_{\text{KIN}} / a \pi^{1/2}) t \tag{Eq. B4}$$

$$t^{1/2} i_d(t) = (nFAD^{1/2} C^0 / \pi^{1/2}) - (nFAD^{1/2} k_{\text{KIN}} / a \pi^{1/2}) t \tag{Eq. B5}$$

This model was found to be most effective in the middle of the stop flow period where the effects of turbulent flow and nutrient depletion are both minimized.

REFERENCES

1. Aggarwal, K.; Lee, K.H. *Brief. Funct. Genomic. Proteomic.* **2003**, *2*, 175-184.
2. Schuster, P. *Montash. Chem.* **2008**, *139*, 427-446.
3. Wikswo, J.P.; Prokop, A.; Baudenbacher, F.; Cliffel, D.; Csukas, B., *et al. IEE Proc.-Nanobiotechnol.* **2006**, *153*, 81-101.
4. Sgroi, D.C.; Teng, S.; Robinson, G.; R, L.; Hudson, J.R., *et al. Cancer Res.* **1999**, *59*, 5656-5661.
5. Golub, T.R.; Slonim, D.K.; Tamayo, P.; Huard, C.; Gaasenbeek, M., *et al. Science* **1999**, *286*, 531-537.
6. Chen, J.J.W.; Peck, K.; Hong, T.-M.; Yang, S.-C.; Sher, Y.-P., *et al. Cancer Res.* **2001**, *61*, 5223-5230.
7. Verpoorte, R.; Choi, Y.H.; Mustafa, N.R.; Kim, H.K. *Phytochem. Rev.* **2008**, *7*, 525-537.
8. Robertson, D.G. *Toxicol. Sci.* **2005**, *85*, 809-822.
9. Clarke, C.J.; Haselden, J.N. *Toxicol. Pathol.* **2008**, *36*, 140-147.
10. Lindon, J.C.; Holmes, E.; Nicholson, J.K. *Anal. Chem.* **2003**, *75*, 384A-391A.
11. Fiehn, O. *Comp. Funct. Genom.* **2001**, *2*, 155-168.
12. Nicholson, J.K.; Lindon, J.C.; Holmes, E. *Xenobiotica* **1999**, *29*, 1181-1189.
13. Lindon, J.C.; Nicholson, J.K. *Trends Anal. Chem.* **2008**, *27*, 194-204.
14. Wittman, C.; Heinzle, E. *Biotechnol. Bioeng.* **1999**, *62*, 739-750.
15. Goudar, C.; Biener, R.; Zhang, C.; Michaels, J.; Piret, J., *et al. Adv. Biochem. Eng. Biotechnol.* **2006**, *101*, 99-118.
16. Eklund, S.E.; Taylor, D.; Kozlov, E.; Prokop, A.; Cliffel, D.E. *Anal. Chem.* **2004**, *76*, 519-527.
17. Eklund, S.E.; Snider, R.M.; Wikswo, J.P.; Baudenbacher, F.; Prokop, A., *et al. J. Electroanal. Chem.* **2006**, *587*, 333-339.
18. Eklund, S.E.; Cliffel, D.E.; Kozlov, E.; Prokop, A.; Wikswo, J.P., *et al. Anal. Chim. Acta* **2003**, *296*, 93-101.

19. Eklund, S.E.; Kozlov, E.; Taylor, D.E.; Baudenbacher, F.; Cliffler, D.E. In *Methods in Molecular Biology*; Rosenthal, S. J., Wright, D. W., Eds.; Humana Press Inc: Totowa, NJ, 2005; Vol. 303, pp 209.
20. Skoog, D.A.; Holler, F.J.; Crouch, S.R. *Principles of Instrumental Analysis*; 6th ed.; Thomson Brooks/Cole: Belmont, CA, 2006.
21. Hafner, F. *Biosens. Bioelectron.* **2000**, *15*, 149-158.
22. Smart, D.; Coppel, A.; Rossant, C.; Hall, M.; McKnight, A.T. *Eur. J. Pharmacol.* **1999**, *379*, 229-235.
23. Coldwell, M.C.; Boyfield, I.; Brown, A.M.; Stemp, G.; Middlemiss, D.N. *Br. J. Pharmacol.* **1999**, *127*, 1135-1144.
24. Landwojtowicz, E.; Nervi, P.; Seelig, A. *Biochemistry* **2002**, *41*, 8050-8057.
25. Cao, C.J.; Mioduszewski, R.J.; Menking, D.E.; Valdes, J.J.; Cortes, V.I., *et al.* *Toxicol. in Vitro* **1997**, *11*, 285-293.
26. Khare, S.; Gokulan, K.; Linthicum, D.S. *J. Neurosci. Res.* **2001**, *63*, 64-71.
27. Parak, W.J.; Dannohl, S.; George, M.; Schuler, M.K.; Schaumburger, J., *et al.* *J. Rheumatol.* **2000**, *27*, 2312-2322.
28. May, L.T.; Lin, Y.; Sexton, P.M.; Christopoulos, A. *J. Pharmacol. Exp. Ther.* **2005**, *312*, 382-390.
29. Parce, J.W.; Owicki, J.C.; Kersco, K.M.; Sigal, G.B.; Wada, H.G., *et al.* *Science* **1989**, *246*, 243-247.
30. Owicki, J.C.; Bousse, L.J.; Hafeman, D.G.; Kirk, G.L.; Olson, J.D., *et al.* *Annu. Rev. Biophys. Biomol. Struct.* **1994**, *23*, 87-113.
31. *Cytosensor Microphysiometer System: User's Manual*; Molecular Devices Corporation: Sunnyvale, CA, 1995.
32. McConnell, H.M.; Owicki, J.C.; Parce, J.W.; Miller, D.L.; Baxter, G.T., *et al.* *Science* **1992**, *257*, 1906-1912.
33. Bard, A.J.; Faulkner, L.R. *Electrochemical Methods: Fundamentals and Applications*; 2nd ed.; John Wiley and Sons, Inc: New York, 2001.
34. Hafeman, D.G.; Parce, J.W.; McConnell, H.M. *Science* **1988**, *240*, 1182-1185.
35. Parce, J.W.; Owicki, J.C.; Wada, H.G.; Kersco, K.M. *Altern. Meth. Toxicol.* **1991**, *8*, 97-106.

36. Ritov, V.B.; Murzakhmetova, M.K.; Tverdislova, I.L.; Menshikova, E.V.; Butylin, A.A., *et al. Biochim. Biophys. Acta* **1993**, *1148*, 257-262.
37. Lord, J.M.; Merrett, M.J. *New Phytol.* **1973**, *72*, 249-252.
38. Bueding, E.; Goldfarb, W. *J. Biol. Chem.* **1941**, *141*, 539-544.
39. Onstad, J.; Hancock, D.; Wolf, P.L. *Clin. Chem.* **1975**, *21*, 895.
40. Voet, D.; Voet, J.G.; Pratt, C.W. *Fundamentals of Biochemistry*; John Wiley & Sons: New York, 2002.
41. Clark, L.C.; Wolf, R.; Granger, D.; Taylor, Z. *J. Appl. Physiol.* **1953**, *6*, 189-193.
42. Harvey, D. *Modern Analytical Chemistry*; McGraw-Hill: Boston, 2000.
43. Heller, A.; Feldman, B. *Chem. Rev.* **2008**, *108*, 2482-2505.
44. Wang, J. *Chem. Rev.* **2008**, *108*, 814-825.
45. Clark, L.C.; Lyons, C. *Ann. N.Y. Acad. Sci.* **1962**, *102*, 29-45.
46. Guilbault, G.G.; Lubrano, G.J. *Anal. Chim. Acta* **1973**, *64*, 439-455.
47. Michael, A.C.; Borland, L.M. *Electrochemical Methods for Neuroscience*; CRC Press: Boca Raton, 2007.
48. Wilson, G.S.; Gifford, R. *Biosens. Bioelectron.* **2005**, *20*, 2388-2403.
49. Robinson, D.L.; Hermans, A.; Seipel, A.T.; Wightman, R.M. *Chem. Rev.* **2005**, *10*, 2554-2584.
50. Bange, A.; Halsall, H.B.; Heineman, W.R. *Biosens. Bioelectron.* **2005**, *20*, 2488-2503.
51. Chang, S.-C.; Pereira-Rodrigues, N.; Henderson, J.R.; Cole, A.; Bedioui, F., *et al. Biosens. Bioelectron.* **2005**, *21*, 917-922.
52. Guglielmo-Vireta, V.; Thullie, P. *J. Immunol. Meth.* **2007**, *328*, 70-78.
53. Zhao, Q.; Gan, Z.; Zhauang, Q. *Electroanalysis* **2002**, *14*, 1609-1613.
54. Delahay, P. *New Instrumental Methods in Electrochemistry*; Interscience Publishers: New York, 1954.
55. Hickling, A. *Trans. Faraday Soc.* **1942**, *38*, 27-33.
56. Lingane, J.J. *Electroanalytical Chemistry*; Interscience Publishers: New York, 1953.

57. Amatore, C.; Maisonhaute, E.; Simonneau, G. *J. Electroanal. Chem* **2000**, *486*, 141-155.
58. Steinberg, M.D.; Lowe, C.R. *Sens. Actuators, B* **2004**, *B97*, 284-289.
59. Gopinath, A.V.; Russell, D. *Chem. Educ.* **2006**, *11*, 23-28.
60. Hildebrandt, A.; Ribas, J.; Bragos, R.; Marty, J.-L.; Tresanchez, M., *et al. Talanta* **2008**, *75*, 1208-1213.
61. Huang, C.-Y.; Syu, M.-J.; Chang, Y.-S.; Chang, C.-H.; Chou, T.-C., *et al. Biosens. Bioelectron.* **2007**, *22*, 1694-1699.
62. Kwakye, S.; Baeumner, A. *Sens. Actuators, B* **2007**, *B123*, 336-343.
63. Pittet, P.; Lu, G.-N.; Galvan, J.-M.; Ferrigno, R.; Blum, L.J., *et al. IEEE Sens. J.* **2008**, *8*, 565-571.
64. Rocchitta, G.; Migheli, R.; Dedola, S.; Calia, G.; Desole, M.S., *et al. Sens. Actuators, B* **2007**, *B126*, 700-709.
65. Martin, R.S.; Ratzlaff, K.L.; Huynh, B.H.; Lunte, S.M. *Anal. Chem.* **2002**, *74*, 1136-1143.
66. Cardoso, J.L.; de Menezes, L.E.; de Emeri, J.L.; Fontes, M.B.A.; Gongora-Rubio, M.R. **2008**, *36*, 623-635.
67. Popovtzer, R.; Neufeld, T.; Ron, E.Z.; Rishpon, J.; Shacham-Diamand, Y. *Sens. Actuators, B* **2006**, *B119*, 664-672.
68. Cumyn, V.K.; Fleischauer, M.D.; Hatchard, T.D.; Dahn, J.R. *Electrochem. Solid State Lett.* **2003**, *6*, E15-E18.
69. Fang, T.; McGrath, M.; Diamond, D.; Smyth, M.R. *Anal. Chim. Acta* **1995**, *305*, 347-58.
70. Ciobanu, M.; Cliffel, D.E. *Abstracts of Papers, 234th ACS National Meeting, Boston, MA, United States, August 19-23, 2007* **2007**, AEI-002.
71. Hinow, P.; Gerlee, P.; McCawley, L.J.; Quaranta, V.; Ciobanu, M., *et al. arXiv.org, e-Print Arch., Quant. Biol.* **2008**, 1-25, arXiv:0810.1024v1 [q-bio TO].
72. Snider, R.M.; Ciobanu, M.; Rue, A.E.; Cliffel, D.E. *Anal Chim Acta* **2008**, *609*, 44-52.
73. Ciobanu, M.; Snider, R.M.; Rue, A.E.; Chen, Z.; Powers, A.C., *et al. Analytical Chemistry manuscript in preparation.*

74. Yicong, W.; Ping, W.; Xuesong, Y.; Qingtao, Z.; Rong, L., *et al. Biosens. Bioelectron.* **2001**, *16*, 277-86.
75. Shapiro, A.M.J.; Nanji, S.A.; Lakey, J.R.T. *Immunol. Rev.* **2003**, *196*, 219-236.
76. *National Diabetes Fact Sheet: United States, 2003*, U.S. Department of Health and Human Services, Centers for Disease Control and Prevention, 2004.
77. Montague, W. *Diabetes and the Endocrine Pancreas: A Biochemical Approach*; Oxford University Press: New York, 1983.
78. Taylor-Fishwick, D.A.; Pittenger, G.L.; Vinik, A.I. *Drug Dev. Res.* **2008**, *69*, 165-176.
79. Bonner-Weir, S. In *The Exocrine Pancreas*; Samols, E., Ed.; Raven Press: New York, 1991, pp 15-27.
80. Rocheleau, J.V.; Walker, G.M.; Head, W.S.; McGuinness, O.P.; Piston, D.W. *Proc. Natl. Acad. Sci. U.S.A.* **2004**, *101*, 12899-12903.
81. Brissova, M.; Fowler, M.J.; Nicholson, W.; Chu, A.; Hirshberg, B., *et al. J. Histochem. Cytochem.* **2005**, *53*, 1087-1097.
82. Pfeifer, M.A.; Broadstone, V.L. In *The Endocrine Pancreas*; Samols, E., Ed.; Raven Press: New York, 1991, pp 175-189.
83. Straub, S.G.; Sharp, G.W.G. *Diabetes Metab. Res. Rev.* **2002**, *18*, 451-453.
84. Wu, L.; Nicholson, W.; Knobel, S.M.; Steffner, R.J.; May, J.M., *et al. J. Biol. Chem.* **2004**, *279*, 12126-12134.
85. Schmid, G.M.; Meda, P.; Caille, D.; Wargent, E.; O'Dowd, J., *et al. J. Biol. Chem.* **2007**, *282*, 12717-12724.
86. Hiatt, N.; Davidson, M.B.; Chapman, L.W.; Sheinkopf, J.A. *Diabetes* **1978**, *27*, 550-3.
87. Gomez, M.; Curry, D.L. *Endocrinology* **1973**, *92*, 1126-1134.
88. Sanger, F. *Science* **1959**, *129*, 1340-1344.
89. Permutt, M.A. In *The Islets of Langerhans: Biochemistry, Physiology, and Pathology*; Cooperstein, S. J., Watkins, D., Eds.; Academic Press: New York, 1981, pp 75-95.
90. de Groot, M.; Schuurs, T.A.; van Schilfgaarde, R. *J. Surg. Res.* **2004**, *121*, 141-150.
91. Leitao, C.B.; Cure, P.; Tharavanij, T.; Baidal, D.A.; Alejandro, R. *Curr. Diab. Rep.* **2008**, *8*, 324-31.

92. Robertson, R.P. *N. Engl. J. Med.* **2004**, *350*, 694-705.
93. Shapiro, A.M.J.; Lakey, J.R.T.; Ryan, E.A.; Korbitt, G.S.; Toth, E., *et al.* *N. Engl. J. Med.* **2000**, *343*, 230-238.
94. Ryan, E.A.; Paty, B.W.; Senior, P.A.; Bigam, D.; Alfadhli, E., *et al.* *Diabetes* **2005**, *54*, 2060-2069.
95. Hunkeler, D.; Rehor, A.; Ceausoglu, I.; Schuldt, U.; Canaple, L., *et al.* *Ann. N.Y. Acad. Sci.* **2001**, *944*, 456-471.
96. Shirouzu, Y.; Gu, Y.; Koga, M.; Sakurai, T.; Qi, M., *et al.* *J. Surg. Res.* **2006**, *133*, 167-175.
97. Bussiere, C.T.; Lakey, J.R.T.; Shapiro, A.M.J.; Korbitt, G.S. *Diabetologia* **2006**, *49*, 2341-2349.
98. Poirier, H.; Rouault, C.; Clement, L.; Niot, I.; Monnot, M.-C., *et al.* *Diabetologia* **2005**, *48*, 1059-1065.
99. Persaud, S.J.; Muller, D.; Belin, V.D.; Kitsou-Mylona, I.; Asare-Anane, H., *et al.* *Diabetes* **2007**, *56*, 197-203.
100. Cooksey, R.C.; Pusuluri, S.; Hazel, M.; McClain, D.A. *Am. J. Physiol. Endocrinol. Metab.* **2006**, *290*, E334-E340.
101. Sweet, I.R.; Cook, D.L.; DeJulio, E.; Wallen, A.R.; Khalil, G., *et al.* *Diabetes* **2004**, *53*.
102. Sugden, M.C.; Greenwood, G.K.; Smith, N.D.; Holness, M.J. *Endocrinology* **2003**, *144*, 146-153.
103. Holness, M.J.; Greenwood, G.K.; Smith, N.D.; Sugden, M.C. *Diabetes* **2006**, *55*, 3501-3508.
104. Bergsten, P. *Am. J. Physiol. Endocrinol. Metab.* **1998**, *37*, E796-E800.
105. Cunha, D.A.; Carneiro, E.M.; Alves, M.d.C.; Jorge, A.G.; Morais de Sousa, S., *et al.* *Am. J. Physiol.* **2005**, *289*, E768-E775.
106. Porksen, N.; Nyholm, B.; Veldhuis, J.D.; Butler, P.C.; Schmitz, O. *Am. J. Physiol. Endocrinol. Metab.* **1997**, *273*, E908-E914.
107. Yang, C.; Huang, H.; Zhang, H.; Liu, M. *Anal. Lett.* **2006**, *39*, 2463-2473.
108. Maghasi, A.T.; Halsall, H.B.; Heineman, W.R.; Rodriguez-Rilob, H.L. *Anal. Biochem.* **2004**, *326*, 183-189.

109. Barbosa, R.M.; Silva, A.M.; Tome, A.R.; Stamford, J.A.; Santos, R.M., *et al.* *Biochem. Biophys. Res. Commun.* **1996**, *228*, 100-104.
110. Qian, W.-J.; Peters, J.L.; Dahlgren, G.M.; Gee, K.R.; Kennedy, R.T. *Biotechniques* **2004**, *37*, 922-933.
111. Roper, M.G.; Shackman, J.G.; Dahlgren, G.M.; Kennedy, R.T. *Anal. Chem.* **2003**, *75*, 4711-4717.
112. Shackman, J.G.; Dahlgren, G.M.; Peters, J.L.; Kennedy, R.T. *Lab Chip* **2005**, *5*, 56-63.
113. Cox, J.A.; Gray, T. *Anal. Chem.* **1989**, *61*, 2462-2464.
114. Huang, L.; Shen, H.; Atkinson, M.A.; Kennedy, R.T. *Proc. Natl. Acad. Sci. U.S.A.* **1995**, *92*, 9608-12.
115. Gorski, W.; Aspinwall, C.A.; Lakey, J.R.T.; Kennedy, R.T. *J. Electroanal. Chem* **1997**, *425*, 191-199.
116. Cheng, L.; Pacey, G.E.; Cox, J.A. *Anal. Chem.* **2001**, *73*, 5607-5610.
117. Pikulski, M.; Gorski, W. *Anal. Chem.* **2000**, *72*, 2696-2702.
118. Elsen, H.A.; Slowinska, K.; Hull, E.; Majda, M. *Anal. Chem.* **2006**, *78*, 6356-6363.
119. Nagy, Z.; You, H. *Electrochim. Acta* **2002**, *47*, 3037-3055.
120. Baughman, R.H.; Zakhidov, A.A.; de Heer, W.A. *Science* **2002**, *297*, 787-792.
121. Musameh, M.; Wang, J.; Merkoci, A.; Lin, Y. *Electrochem. Comm.* **2002**, *4*, 743-746.
122. Gooding, J.J.; Wibowo, R.; Liu, J.Q.; Yang, W.; Losic, D., *et al.* *J. Am. Chem. Soc.* **2003**, *125*, 9006-9007.
123. Yu, X.; Chattopadhyay, D.; Galeska, I.; Papadimitrakopoulos, F.; Rusling, J.F. *Electrochem. Comm.* **2003**, *5*, 408-411.
124. Wang, J. *Electroanalysis* **2005**, *17*, 7-14.
125. Wang, J.; Agnes, L.; Martinez, T. *Bioelectrochem. Bioenerg.* **1992**, *29*, 215-221.
126. Wang, J.; Musameh, M. *Anal. Chim. Acta* **2004**, *511*, 33-36.
127. Wang, J.; Tangkuaram, T.; Loyprasert, S.; Vazquez-Alvarez, T.; Veerasai, W., *et al.* *Anal. Chim. Acta* **2007**, *581*, 1-6.
128. Wu, K.; Ji, X.; Fei, J.; Hu, S. *Nanotechnology* **2004**, *15*, 287-291.

129. Zhang, M.; Mullens, C.; Gorski, W. *Anal. Chem.* **2005**, *77*, 6396-6401.
130. Naumov, S.; Janovsky, I.; Knolle, W.; Mehnert, R. *Macromol. Chem. Phys.* **2004**, *205*, 1530-1535.
131. Chen, N.; Liu, L.; Zhang, Y.; Ginsberg, H.N.; Yu, Y.-H. *Diabetes* **2005**, *54*, 3379.
132. Dong, F.; Fang, C.X.; Yang, X.; Zhang, F.L.; Lopez, J.R. *Diabetologia* **2006**, *49*, 1421.
133. Fang, C.X.; Dong, F.; Ren, B.H.; Epstein, P.N.; Ren, J. *Diabetologia* **2005**, *48*, 2412-2421.
134. Brissova, M.; Fowler, M.; Wiebe, P.; Shostak, A.; Shiota, M., *et al.* *Diabetes* **2004**, *53*, 1318-1325.
135. Dujardin, E.; Ebbesen, T.W.; Krishnan, A.; Tracy, M.M.J. *Adv. Mater.* **1998**, *10*, 611.
136. Bironaite, D.; Gera, L.; Stewart, J.M. *Chem. Biol. Interact.* **2004**, *150*, 283-93.
137. Ikeda, K.; Kobayashi, S.; Suzuki, M.; Miyata, K.; Yamada, T., *et al.* *Life Sci.* **1999**, *65*, 1569-1577.
138. Ferguson, J.; Allsop, R.H.; Taylor, R.M.R.; Johnston, I.D.A. *Diabetologia* **1976**, *12*, 115-121.
139. Ronnebaum, S.M.; Ilkayeva, O.; Burgess, S.C.; Joseph, J.W.; Lu, D., *et al.* *J. Biol. Chem.* **2006**, *281*, 30593-602.
140. Ishihara, H.; Wollheim, C.B. *IUBMB Life* **2000**, *49*, 391-395.
141. Bennett, G.W.; Brazell, M.P.; Marsden, C.A. *Life Sci.* **1981**, *29*, 1001.
142. Sharp, G.W. *Am. J. Physiol. Cell* **1996**, *271*, C1781-99.
143. Srivastava, S.; Goren, H.J. *Diabetes* **2003**, *52*, 2049-56.
144. Wilburn, J.P.; Ciobanu, M.; Cliffel, D.E. *Abstracts of Papers, 234th ACS National Meeting, Boston, MA, United States, August 19-23, 2007* **2007**, AEI-010.
145. Sack, D.A.; Sack, R.B.; Nair, G.B.; Siddique, A.K. *Lancet* **2004**, *363*, 223-233.
146. Finkelstein, R.A. In *Medical Microbiology*; 4th ed.; Baron, S., Ed.; University of Texas Medical Branch: Galveston, Texas, 1996, pp.
147. Olivier, V.; Salzman, N.H.; Fullner Satchell, K.J. *Infect. Immun.* **2007**, *75*, 5043-5051.

148. Lundgren, O. *Pharmacol. Toxicol.* **2002**, *90*, 109-120.
149. Sanchez, J.; Holmgren, J. *Cell. Mol. Life Sci.* **2008**, *65*, 1347-1360.
150. Selinger, Z. *Annu. Rev. Biochem.* **2008**, *77*, 1-13.
151. Martin, T.F.J.; Grishanin, R.N. *Meth. Cell Biol.* **2003**, *71*, 267-286.
152. Majoul, I.; Schmidt, T.; Pomasanova, M.; Boutkevich, E.; Kozlov, Y., *et al.* *J. Cell Sci.* **2002**, *115*, 817-826.
153. Chijiwa, T.; Mishima, A.; Hagiwara, M.; Sano, M.; Inoue, T., *et al.* *J. Biol. Chem.* **1990**, *265*, 5267-5272.
154. Cassel, D.; Selinger, Z. *Proc. Natl. Acad. Sci. U.S.A* **1977**, *74*, 3307-3311.
155. Keusch, G.T.; Rahal, J.J.; Weinstein, L.; Grady, G.F. *Am. J. Physiol.* **1970**, *218*, 703-707.
156. Resnick, R.J.; Kole, H.K.; Racker, E. *Arch. Biochem. Biophys.* **1991**, *286*, 579-585.
157. Insel, P.A.; Ostrom, R.S. *Cell Molec. Neurobiol.* **2003**, *23*, 305-314.
158. Cohen, P. *Cell Transm.* **2003**, *19*, 11-14.
159. Davies, S.P.; Reddy, H.; Caivano, M.; Cohen, P. *Biochem. J.* **2000**, *351*, 95-105.
160. N'Dri, N.A.; Stremmler, M.; Eluvathingal, S.; Cliffel, D.E.; Snider, R.M., *et al.* *Biophys. J.* **manuscript in preparation**.
161. Velkovsky, M.; Cliffel, D.E.; Snider, R.M.; N'Dri, N.A.; Stremmler, M., *et al.* **manuscript in preparation**.
162. Keil, R.G.; Ciobanu, M.; Snider, R.M.; Armstrong, T.; Cliffel, D.E. **manuscript in preparation**.

Rachel M. Snider

Department of Chemistry, Vanderbilt University
VU Station B #351822
7330 Stevenson Center
Nashville, Tennessee 37235-1822
Tel. (615) 322-5013; E-mail. r.snider@vanderbilt.edu

Education

2003-2008 Ph.D. in Analytical Chemistry, Vanderbilt University, Nashville, TN
1999-2003 B. S. Chemistry *cum laude*, Sweet Briar College, Sweet Briar, VA

Research Experience

- 2003-2008 **Graduate Research Fellow with Prof. David E. Cliffel**
- Developed new sensor for electrochemical detection of insulin
 - Developed methodology for evaluating islet physiology in multianalyte microphysiometer
 - Wrote program using LabVIEW to control multi-channel bipotentiostat and collect data
 - Applied multianalyte microphysiometry to the effect of cholera toxin on PC-12 metabolism
 - Experienced with BSL 2 work with cholera toxin and cell culture
- 2002-2003 **Undergraduate Research Assistant with Prof. Susan Piepho**
- Developed LabVIEW virtual instrument to investigate luminescence decay
 - Studied the effect of sample media on luminescence quenching
- 2002 **Undergraduate Research Assistant, Vanderbilt Summer Research**
Advisor: David Wright
- Synthesized and purified synthetic hemozoin, purified porphyrin analog
 - Gained experience with synthetic methods and liquid chromatography
- 2001 **Research Assistant, Sweet Briar Honors' Summer Research Program**
Advisor: John Beck
- Performed natural products research on herbs from the US Virgin Islands
 - Developed a bioassay method and extraction protocols

Publications

“A Multiwalled Carbon Nanotube/Dihydropyran Composite Film Electrode for Insulin Detection in a Microphysiometer Chamber.” Snider, R.M.; Ciobanu, M.; Rue, A.E.; Cliffel, D.E. *Analytica Chimica Acta* **2008**, *609*, 44-52

“Multianalyte Microphysiometry as a Tool in Metabolomics and Systems Biology”, Eklund, S.E.; Snider, R.M.; Wikswo, J.; Baudenbacher, F.; Prokop, A.; Cliffel, D.E. *Electroanalytical Chemistry* **2006**, *587*, 333-339

“Bioremediation of Soil Contaminated with Hexachlorobenzene”, DeSantis, J.; Snider, R.; Granger, R.M. *Journal of Undergraduate Chemistry Research* **2002**, *1*, 83-87

Manuscripts in Preparation and Likely Journals

“Design and Construction of a Multiple Chamber Multipotentiostat for Multianalyte Microphysiometry”, Lima, E.A.; **Snider, R.M.**; Reiserer, R.S.; Wikswow, J.P.; Cliffel, D.E. (to be submitted to *Sensors and Actuators B*)

“Metabolic Profiling of Islets Using Multianalyte Microphysiometry”, Ciobanu, M.; **Snider, R.M.**; Rue, A.E.; Chen, Z.; Powers, A.C.; Cliffel, D.E. (to be submitted to *Analytical Chemistry*)

“MAMP Determination of the Apparent Kinetic Rate Constants for Mammalian Cellular Metabolite-Solution Transport Using Thin Enzyme Electrodes: Lactate, Glucose and Oxygen.” Keil, R. G.; Ciobanu, M.; **Snider, R. M.**; Armstrong, T.; Cliffel, D. E.

“Computation of Cell Metabolic Rates in the Multianalyte Microphysiometer.” N'Dri, N. A.; Stremmer, M.; Eluvathingal, S.; Cliffel, D. E.; **Snider, R.M.**; Velkovsky, M.; Wikswow, J. P. (to be submitted to *Biophys. Journal*)

“Modeling the Measurements of Cellular Fluxes in Microbioreactor Devices Using Thin Enzyme Electrodes.” Velkovsky, M.; Cliffel, D. E.; **Snider, R. M.**; N'Dri, N. A.; Stremmer, M.; Wikswow, J. P.

Presentations

Snider, R.M.; Cliffel, D.E.; Wikswow, J.P. “Electrochemical Studies of the Effect of Cholera and Botulinum Toxins on Cellular Metabolism.” *Abstracts of Papers*, Pittsburg Conference, New Orleans, LA, 2008; Assessing Cytotoxicity and Cellular Morphology. 2910-3.

Snider, R.M.; Lima, E.; Reiserer, R.; Green, C.; Wikswow, J.; Cliffel, D.E. “A Multichannel Bipotentiostat for Electrochemical measurements in the Multianalyte Microphysiometers.” *Abstracts of Papers*, Lab Automation 2007, Palm Springs, California, 2007. (poster presentation)

Snider, R.M.; Eklund, S.E.; Wikswow, J.; Cliffel, D.E. “The Effect of *Botulinum* Neurotoxin A on Cellular Metabolism as Measured Using Multianalyte Microphysiometry.” *Abstracts of Papers*, Joint International Meeting Electrochemical Society, Cancun, Mexico, 2006.

Snider, R.M.; Ciobanu, M.; Rue, A.E.; Chen, Z.; Powers, A.C.; Cliffel, D.E. “An Electrochemical Insulin Sensor for the Metabolic Profiling of Islets.” *Abstracts of Papers*, Pittsburg Conference, Orlando, FL, 2006; Bio- and Nanoelectrochemistry 430-5. (poster presentation)

Snider, R.M.; Rue, A.E.; Ciobanu, M.; Chen, Z.; Powers, A.C.; Cliffel, D.E. “Multianalyte Microphysiometry for the Metabolic Profiling of Islets.” *Abstracts of Papers*, 57th Southeast Regional Meeting of the American Chemical Society, Memphis, TN, 2005; *Analytical Chemistry* 149.

Honors and Awards

- Society of Electroanalytical Chemists Travel Award, Pittcon 2008
- Student Travel Award, Lab Automation 2007
- Recipient of NIH-sponsored Chemistry-Biology Interface Training Grant, 2004-present
- Vanderbilt University Graduate Fellowship, 2003-present
- Government Assistantship in Areas of National Need Fellowship, 2003-2004

Affiliations

- Founding Member of the Student Committee of the Association for Laboratory Automation
- Electrochemical Society
- American Chemical Society

References

1. David E. Cliffel, Vanderbilt University, Department of Chemistry; (615)343-3937; d.cliffel@vanderbilt.edu
2. John Wikswo, Vanderbilt University, Department of Biomedical Engineering; (615)343-4124; john.wikswo@vanderbilt.edu
3. David Wright; Vanderbilt University, Department of Chemistry; (615)322-2636; david.wright@vanderbilt.edu